

NANOFLUIDIC CHANNELS FOR BIOLOGICAL SEPARATIONS

A Dissertation

Presented to the Faculty of the Graduate School

Of Cornell University

In Partial Fulfillment of the Requirements for the Degree of

Doctor of Philosophy

by

Joshua David Cross

January 2007

© 2007 Joshua David Cross

NANOFLUIDIC CHANNELS FOR BIOLOGICAL SEPARATIONS

Joshua David Cross, Ph.D.

Cornell University 2007

Nanofluidic channels are used to separate DNA molecules by length and applications of the channels to other biomolecules are discussed. The problem of separating DNA and biomolecules by length, charge, or other physical characteristics has consumed a tremendous amount of time and resources over the latter half of the twentieth century and the beginning of the twenty-first century. Micro- and nanofluidic structures afford the opportunity to increase separation effectiveness while decreasing the cost of analysis. Additionally, owing to their simplicity, micro- and nanofluidic devices offer the possibility of modeling molecular motion through confining environments from fundamental physical principles.

Three nanofluidic devices for separating biomolecules by length are discussed herein. A description of their physical operation is given, and results indicating their effectiveness are presented. Important concepts in molecular biology, polymer physics, and electrophoresis are presented, as well as a review of the trend toward miniaturization of traditional separation techniques. The physical effects manifest in the nanofluidic devices described herein are most easily leveraged in the microchip format, so the details of the fabrication processes used to manufacture these devices are also presented.

BIOGRAPHICAL SKETCH

Joshua David Cross was born in Portland, OR, on 2 May 1979. He grew up across the Columbia River in Vancouver, WA. He was fortunate enough to have an excess of great teachers who always provided him with interesting things to think about and taught him that there are right answers. After graduating from Hudson's Bay High School, he migrated eastward to Appleton, WI, where he attended Lawrence University. Under the driving (percussion) instruction of Dane Richeson, he learned that all the world is a stage and that to be players one must be good. Perhaps the most proximal voice of reason that he had to this point in his education was that of Thomas Ryckman in the Philosophy department. Ultimately, Joshua would take six semesters of classes from Professor Ryckman and has the scar of a minor in Philosophy to prove it. Yet, while he spent many hours in the Conservatory of Music and in Main Hall (the Philosophy Department home), he ultimately spent more time in Science Hall and graduated with a Bachelor of Arts degree in Physics. Upon graduation, he again migrated eastward, ending up in Ithaca, NY. Ithaca has proved a good teacher as well, being utterly unique in so many ways and constantly challenging him to dig deeper to try to understand the world around him.

ACKNOWLEDGEMENTS

I am a wholehearted supporter of the notion that we do not accomplish much without the help of others. If you read through this and feel as if you should have been included but were not, please see me after class and I will make it up to you.

My parents and sister have supported me throughout my educational career and for that I am truly grateful. My wife as well deserves great thanks, for keeping my spirits up, encouraging me to eat lots of carrots, and generally showing me how to be a better person. Additionally, my in-laws have my deepest appreciation for their continual support and encouragement.

I would like to thank Kevan Samiee for being the smartest and most rational person I have ever met. Samuel Stavis, John Mannion, Elizabeth Strychalski, Leon Bellan, Paul Zhu, Jose Moran-Mirabal, Mario Cabodi, Stephane Corgie, and Mathieu Foquet have helped and encouraged me in a myriad of ways over the years. Professors Ted Cox and Robert Austin of Princeton have offered guidance both directly and indirectly and they deserve more than just the slight tip of the hat that I hereby offer. Much of my research involved time in the CNF, and I hope the staff accepts my thanks for their help and patience over the years. I would like to thank Professors Franck, Walker, and BenDaniel for guiding me through the graduate school process and for teaching me things I otherwise would not have learned. Finally, my sincerest thanks go out to Professor Harold Craighead. Thank you for giving me the opportunity to work with you.

TABLE OF CONTENTS

Chapter 1: Overview	1
Chapter 2: Introduction to Micro- and Nanofluidics for Biological Separations	3
Chapter 3: DNA as a Polymer	59
Chapter 4: Theory of Electrophoresis	69
Chapter 5: Microchannel Fabrication and Experimental Setup	77
Chapter 6: Nanopillar Devices	87
Chapter 7: Nanoslit Devices	119
Chapter 8: Entropic Traps	136
Chapter 9: Concluding Remarks	161
References	163

LIST OF FIGURES

2.1	Simple fabrication process	6
2.2	Sacrificial layer fabrication process	7
2.3	High aspect ratio nanopillars	9
2.4	Microfluidic schematic collage	18
2.5	Separation experiment schematic collage	19
2.6	Experimental setup	20
2.7	Serpentine microfluidic device	30
2.8	Results of amino acid separation	31
2.9	Results of microchip sequencing	37
2.10	Sacrificial layer sieving matrix	41
2.11	Example of entropic recoil experiment	45
2.12	Examples of DNA in nanochannels	46
2.13	Entropic trap schematic and energy diagram	51
2.14	Asymmetric diffusion array schematic collage	54
3.1	Chemical structure of DNA	61
3.2	DNA base pairing	62
5.1	Two-layer device fabrication schematic	80
5.2	Experimental setup	86
6.1	Gold island fabrication schematic	88
6.2	SEM of 5nm gold film on silicon	89
6.3	Two SEMs of melted gold on silicon	90
6.4	SEM of melted and etched gold on silicon	91
6.5	Cross-sectional SEMs of nanopillars in silicon	92
6.6	Cross-sectional SEMs of nanopillars in silicon	93
6.7	SEM collage of nanopillar structures in fused silica	94

6.8	SEM collage of destroyed gold island etch mask	95
6.9	SEM of gold evaporated onto photoresist	96
6.10	Effects of heating and etching on gold island size and polydispersity	97
6.11	Polydispersity of gold islands on fused silica	98
6.12	Experimental setup and device schematic	99
6.13	DNA gathering at an interface	104
6.14	Results of DNA electrophoresis in nanopillars	105
6.15	Results of DNA electrophoresis in control channels	106
6.16	Two DNA molecules tracked in nanopillar device	109
6.17	Results of nanopillar electrophoresis with long DNA	111
6.18	Comparison of nanopillar results for DNA ladder experiment	116
7.1	Device schematic and nanoslit illustration	121
7.2	Results of DNA electrophoresis in nanoslits	123
7.3	Results of nanoslit electrophoresis control experiments	124
7.4	Nanoslit electrophoresis results and theoretical fit	127
7.5	Mobility of long DNA in a nanoslit	131
7.6	Elution time of long DNA in a nanoslit	132
7.7	<i>S. pombe</i> separation in a nanoslit	134
8.1	Two schematics of entropic barriers	138
8.2	Schematic of surface area difference for big and small molecules	141
8.3	Collage of optical, SEM, and AFM images of entropic traps	147
8.4	Short double-stranded DNA at an entropic trap	149
8.5	Results of entropic trapping with theoretical fit	150

8.6	Theoretical plot of the number of DNA at a trap versus time for various incident “fluxes”	151
8.7	Theoretical plot of the number of DNA at a trap versus time for various probing frequencies	151
8.8	Comparison of single-stranded and double-stranded DNA gathering at an entropic trap with fits	153
8.9	Comparison of probing frequencies	154
8.10	Data showing the warm up period of the 512B camera	158
8.11	Data illustrating “normalizing” intensity data	159

LIST OF TABLES

6.1	Resolution of DNA separations in nanopillar channel	107
-----	---	-----

List of Symbols

R, R_g, R_{3D} – radius of gyration (nm; chapter 7)

N – total number of base pairs

P, b – persistence length (nm; b in chapter 7)

v – velocity (m/s, cm/s, or $\mu\text{m/s}$)

μ – mobility (cm^2/Vs)

E – electric field (V/cm)

μ_{EOF} – electroosmotic mobility (cm^2/Vs)

μ_{EP} – electrophoretic mobility (cm^2/Vs)

F – free energy (J; chapter 2)

x – reaction coordinate or distance (m, cm, or μm)

T – temperature (K)

P – probability of escape (from an entropic trap; chapter 2)

k – Boltzmann constant (J/K)

t – time (s)

τ – trapping time (s)

μ_0 – free solution mobility (cm^2/Vs)

L – DNA length (nm or μm ; chapter 3)

a – DNA monomer length (nm; chapter 3)

n – number of joints (chapter 3)

l – length of a joint (nm; chapter 3)

R_0 – random flight radius of gyration (nm or μm ; chapter 3)

v_c – excluded volume parameter (μm^3 ; chapter 3)

ψ – electrostatic potential (V or J/C, chapter 3)

r – radial dimension (chapter 3)

ρ – charge distribution (C/m³; chapter 3)
 ε – relative permittivity (chapter 3)
 ε_0 – permittivity of free space (C²/Nm²; chapter 3)
 e – fundamental unit of charge (C)
 F – Faraday constant (C/mole; chapter 3)
 z – valence (chapter 3)
 c – concentration (moles/m³; chapter 3)
 g_h – number of monomers in a sub-blob (chapter 3)
 h, d – nanoslit height (chapter 3; chapter 7)
 F_E – total electric force (N)
 Q – total electric charge (C)
 F_d – total drag force (N)
 D – drag coefficient (kg/s)
 m – mass (kg)
 η – fluid viscosity (kg/m/s)
 δ – drag per basepair (kg/s/bp)
 α – added drag (kg/s; chapter 3)
 β – added charge (C)
 c – gel concentration (usually measured as kg/kg; chapter 4)
 K – retardation coefficient
 f – fractional free volume of a gel
 s – surface area per unit volume of an obstacle (1/m; chapter 4)
 L – long dimension of DNA molecule (m; chapter 4)
 h – length per unit volume of gel fiber (m⁻²; chapter 4)
 A – surface area of DNA molecule (m²; chapter 4)
 N – number density of obstacles (m⁻³; chapter 4)

V – volume of a molecule (m^3 ; chapter 4)
 Δt – time between adjacent peaks (s)
 w_1, w_2 – width of peaks (s)
 Θ – number of contacts per surface area (m^2)
 R_{2D} – two-dimensional radius of gyration (m^2)
 C – total number of DNA-surface contacts (chapter 7)
 α – fraction of DNA molecule interacting with surface (chapter 7)
 f_b – buffer friction per basepair coefficient (kg/s/bp; chapter 7)
 f_s – surface friction per basepair coefficient (kg/s/bp; chapter 7)
 S – total entropy of molecule (J/K; chapter 8)
 $U_{Electric}$ – Electric field energy (J; chapter 8)
 q – polymer charge (C; chapter 8)
 p – passage probability of single escape attempt (chapter 8)
 P – passage probability per second (s^{-1} ; chapter 8)
 w – escape attempt frequency (s^{-1} ; chapter 8)
 d_s – depth of shallow trap region (nm; chapter 8)
 t_{period} – travel time across one period of entropic trap array (s)
 I – fluorescence intensity (camera pixel value)
 N_t – number of molecules probing a trap
 N_i – number of molecules arriving at trap
 N_o – number of molecules leaving a trap
 Φ – rate of incoming molecules ($\#/s$; chapter 8)
 λ – linear density of molecules ($\#/m$; chapter 8)

CHAPTER 1

OVERVIEW

This dissertation describes nano-scale systems evaluated for separating DNA molecules by length. One such system is a nanoscale, artificial gel-like construction made within a fluidic channel (chapter 6). Another system is a thin slit, tens of nanometers in height (chapter 7). And the last system described herein is an entropic barrier, tens of nanometers in thickness (chapter 8). These devices all have the virtue of being easy to fabricate and that fabrication processes used to manufacture these devices are compatible with most other fabrication processes used to make lab-on-a-chip devices. Thus, any of the systems described could easily be incorporated into a lab-on-a-chip device to perform biomolecule separation, purification, or concentration.

I recently co-authored a book chapter with Harold Craighead to be published early in 2007 entitled, "Micro- and Nanofluidics for Biological Separations", to appear in a book entitled *BioCMOS Technologies* and edited by a team from Harvard University (note that the book title is probably subject to change). This book chapter summarizes many introductory concepts from the motivations for doing micro- and nanofabrication for biological applications, to some of the newest techniques and applications of these technologies. Brief discussions of biology, fabrication, and electrophoresis theory are found in the chapter. I have decided to include that chapter, largely unaltered, as the second chapter of this dissertation. The reader already familiar with nanofabrication, biological applications of nanotechnology, and the recent applications of nanofabricated devices is encouraged to skip chapter 2 of this dissertation. Many of the concepts only touched upon in chapter 2 appear in

detail chapters 3, 4, and 5 of this dissertation, so the reader can bypass chapter 2 without loss of introduction.

This dissertation contains a broad overview of biology (chapter 3) relevant for the applications discussed in the experimental chapters 6-8, an overview of electrophoresis theory (chapter 4), and an overview of fabrication techniques (chapter 5). Broad conclusions are drawn at the end of each experimental chapter, but the most encompassing conclusions to the work of this dissertation can be found throughout and at the end of chapter 2; so the reader is encouraged to return to that chapter after having read the remainder of this dissertation and perhaps after having already skipped the chapter.

As a scientist and technologist, I have enjoyed working on nanofluidic systems for DNA applications. The problems yet to be solved include ones that are very scientific in nature (such as how do molecules move through and interact with confining geometries) and ones very applicable to new technologies (such as how to make the best confining geometry with which to separate molecules by length or sequence). I hope that those reading this dissertation come to appreciate that while bio-nanotechnology has solved many scientific and technological problems, there are many more that it can address and that need to be addressed.

CHAPTER 2

INTRODUCTION TO MICRO- AND NANOFUIDICS FOR BIOLOGICAL SEPARATIONS

2.1 Introduction

This chapter is substantially identical to a chapter that I co-authored with Harold Craighead for submission to an edited book reviewing biological applications of CMOS technologies. Slight modifications have been made to facilitate its inclusion in this dissertation. While somewhat long, it serves as a complete introduction to the work presented in chapters 6-8. Substantially more detailed chapters on DNA, polymers, electrophoresis, and specific fabrication techniques that I used follow this chapter. The reader is encouraged to skim this chapter for an overview of the dissertation, and perhaps return to this chapter to obtain an overview of the motivation for doing biological separations in micro- and nanofluidic devices.

Current research on analytical techniques for biological applications is being conducted using micro- and nanofluidic devices fabricated with CMOS processes. Materials such as silicon, silicon nitride, and silicon dioxide are used as device substrates because they are compatible with the lithographic and etching processes required to manufacture nanometer-scale structures. Micro- and nanoscale structures have been fabricated in order to probe and confine molecules on length scales that are comparable to the size of the molecules [1]. At these size scales, advanced separation techniques are possible as are single molecule studies. Micro- and nanofluidic devices have enabled new methods of DNA separation, such as the rapid separation of genomic length DNA. The ability to manipulate, elongate, and detect individual

molecules has opened the door for single molecule restriction mapping, directly observing protein binding, and perhaps even single molecule sequencing [2]. Labs-on-chips, of which microfluidics is the key enabling component, hold the promise of facilitating faster bioanalytical techniques using less reagents with more sensitivity and less variability [3].

This chapter summarizes one subsection of what has become a large field of multidisciplinary research known as microfluidics. Because this chapter was originally written for a book entitled *BioCMOS Technologies*, and because one of the author's expertise is in biological separations in glass- and silicon-based micro- and nanofluidic devices, what follows will be oriented in this direction. Common fabrication techniques, likely familiar to the CMOS engineering community, will be discussed. DNA and proteins will be briefly discussed as these biological molecules are the primary analytes of most of the microfluidic devices discussed. A brief history of the move from "conventional" microfluidics to chip-based microfluidics will be presented. After the fabrication, the biology, and the history, the remainder of the chapter will describe new micro- and nanoscale systems that have been developed to interrogate and analyze biological samples.

2.2 FABRICATION

As CMOS fabrication techniques, academic cleanrooms, and advanced lithographic tools have become more available, engineers have increasingly used these techniques for applications other than the manufacture of "classical" CMOS devices. Using CMOS fabrication techniques to manufacture devices for biological applications is now common in the research community. Conventional techniques for separating and purifying biological molecules

almost always involve capillary electrophoresis, which is electrically driving molecules through fused silica capillaries [4-6]. Using CMOS fabrication techniques, these capillaries can now be etched directly into silicon or glass wafers.

With creative geometries, wafers can hold hundreds of capillaries, each meters in length. In addition to the miniaturization of existing technologies, CMOS fabrication methods allow features to be made with dimensions of comparable size as biomolecules. Currently, the demands of making features on the order of nanometers or tens of nanometers requires “hard” substrates familiar to the world of integrated circuits such as silicon and silicon dioxide. The lithographic methods and the pattern transfer processes (as described below) will no doubt seem familiar to the general CMOS community. The ability to make channels and structures on the scale of biomolecules has enabled entirely new biological applications as well as elucidated many biological and physical phenomena.

Using standard CMOS fabrication technologies, many types of microfluidic devices can be made (see Figures 2.1-3). As previously mentioned, capillaries can be easily placed on chips. Channel widths of tens of microns are defined using standard photolithographic techniques. A resist is spun onto a silicon or glass wafer. The resist is patterned with photolithography or electron beam lithography and developed. Once developed, reactive ion etching or chemical etching can be used to transfer the lithographic pattern into the substrate. The walls and floor of the chip-based microfluidic capillary are thereby defined. The ceiling of the channel is established when a cover wafer is bonded to the etched wafer. For the

simplest implementation of capillaries-on-a-chip, this is all the fabrication required.

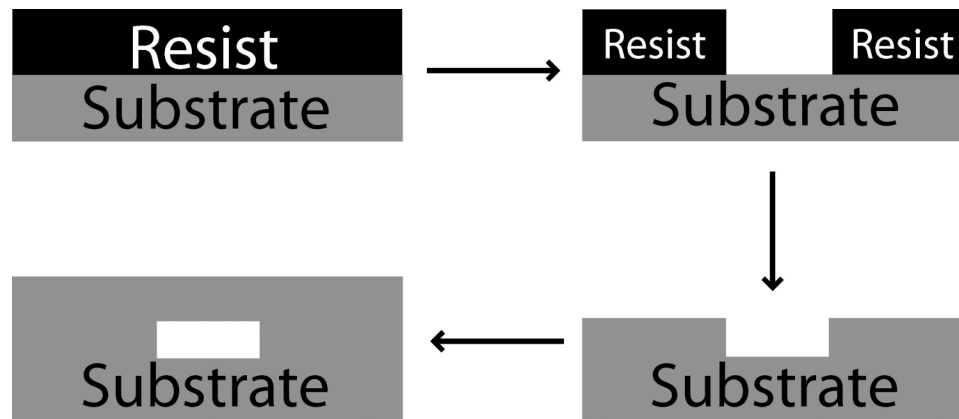


Figure 2.1: Schematic diagrams showing the fabrication process for a simple microfluidic channel. Resist is spin-coated on a SiO_2 substrate. The resist is then patterned with photolithography or electron beam lithography. Wet or reactive ion etching is used to transfer the pattern into the SiO_2 and the resist is removed. Finally, a SiO_2 cover is bonded to the SiO_2 substrate to encapsulate the channels.

Sacrificial layer techniques are sometimes employed to produce very thin channels or when a thin capping layer is required (to reduce background fluorescence, for instance; see Figure 2.2). A sacrificial film is deposited, spun, or grown on the surface of the substrate (examples of sacrificial layers include chrome, photoresist, or polysilicon). Lithography is used to pattern the sacrificial film. A capping layer is grown on the sacrificial film, which then has access holes patterned into it. Once the access holes are opened by wet or dry etching, the sacrificial layer is removed with an appropriate chemical etchant. Another film is then deposited to close the access holes and the microfluidic channels are complete. Capping layers of tens to hundreds of nanometers are possible. The microfluidic channels are defined by the sacrificial layer and can be as shallow as nanometers (see Figure 2.10, for example).

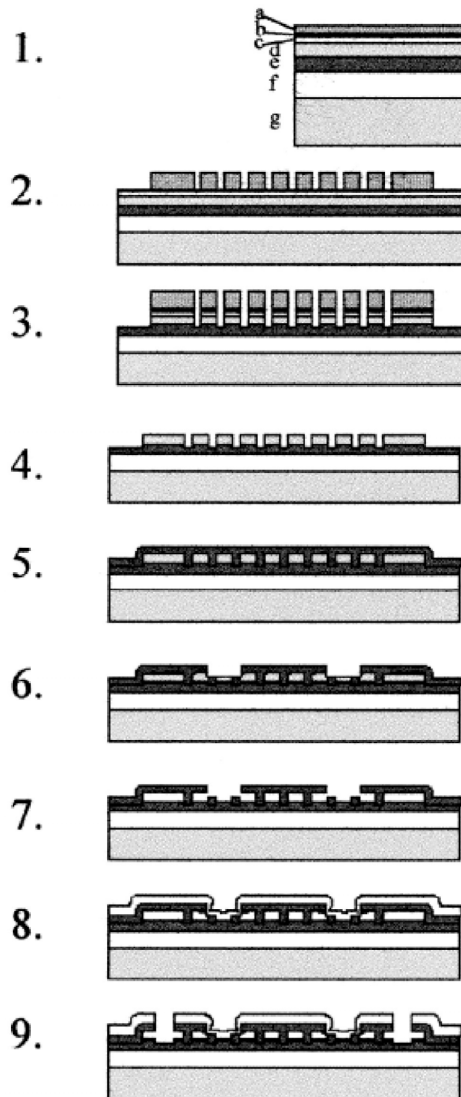


Figure 2.2: An overview of a sacrificial layer fabrication process (reprinted with permission from [7], Copyright 2000 Wiley-VCH Verlag GmbH & Co KG). For an example of a device made using this technique, see Figure 2.10. 1) The film stack is composed of: a-PMMA resist, b-aluminum conducting layer, c-silicon dioxide hard mask, d-polysilicon sacrificial layer, e-silicon nitride floor layer, f-silicon dioxide insulating layer, and g-silicon substrate. 2) Pattern the resist. 3) Etch pattern into sacrificial layer. 4) Remove resist and pattern transfer layers. 5) Apply ceiling silicon nitride layer. 6) Add access holes to facilitate sacrificial layer removal. 7) Remove sacrificial layer. 8) Seal access holes with silicon dioxide. 9) Add reservoirs via new access holes.

More sophisticated fabrication techniques can be used to manufacture progressively more exotic microfluidic devices. An example of high-aspect ratio nano-pillars used to fractionate long DNA molecules is shown in Figure 2.3 (from [8]). Multi-layer lithography, with aligned features, allows one to manufacture microfluidic channels that include holes, grooves in the channel floor, thin slits through otherwise micron deep channels, and similarly shaped gaps or restrictions. As many of these features can be made with sizes comparable to the size of things like DNA and proteins, many biophysical applications are possible in devices with these somewhat sophisticated geometries.

As will be discussed below, the ability to manufacture microfluidic channels with features of comparable size as biomolecules permits new research on fundamental biophysical phenomena and applications. Using confining microfluidic geometries and single molecule imaging techniques, individual molecule properties such as conformation, length, affinity for substrates, and susceptibility to localized chemical treatments can be studied more directly and with better resolution than previously possible. Artificial gel-like structures can be created to separate biomolecules by length, diffusion constant, affinity for patternable substrates, or other physical properties. Additionally, due to the high surface-to-volume ratio achievable in microfluidic channels, miniaturized capillary systems are able to perform better than their macroscopic versions as higher electric fields can be used to drive molecules because heat dissipation is greatly improved.

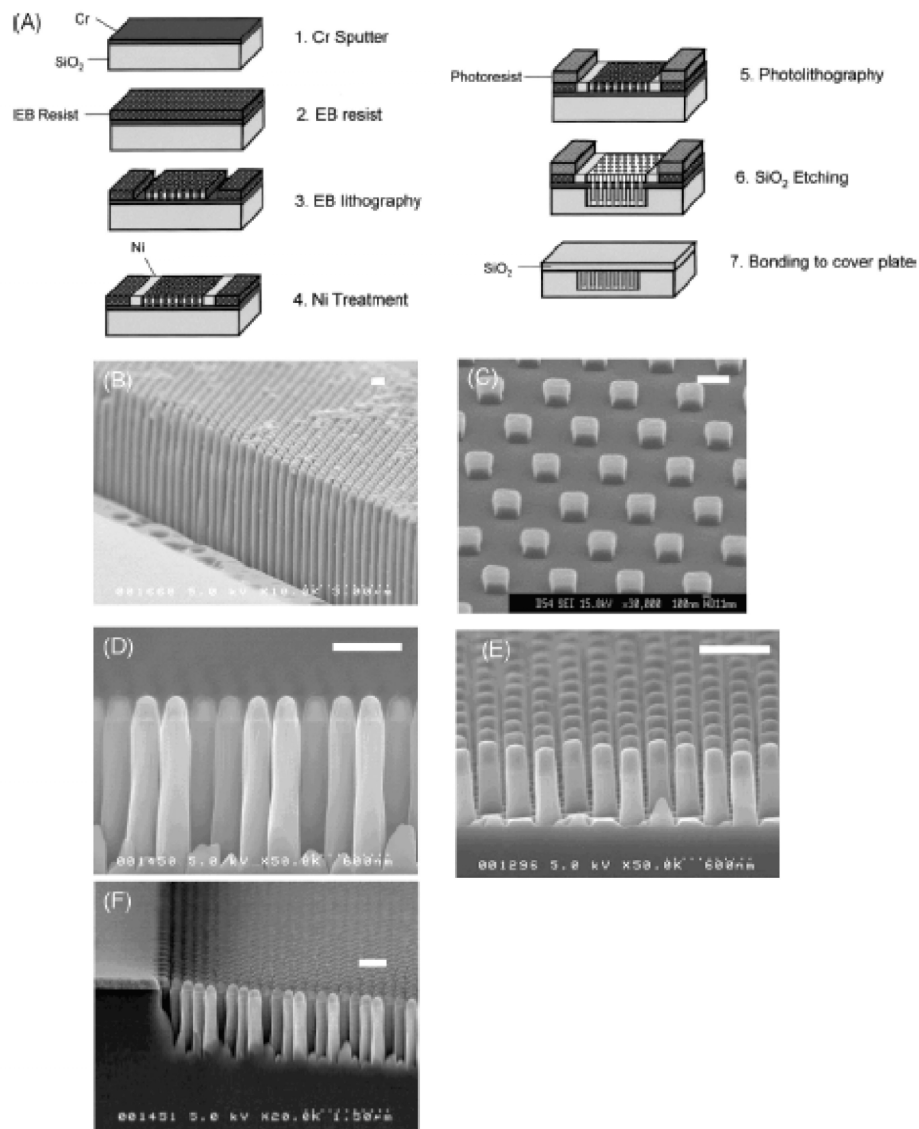


Figure 2.3: A schematic diagram of the fabrication process used to produce the high aspect ratio nanopillars shown in the lower scanning electron micrographs (reprinted with permission from [8], Copyright 2004 American Chemical Society). The devices are fabricated on a glass substrate. Chrome is used as a conducting layer under the electron beam resist. Nickel is electroplated to act as a mask for the silicon dioxide dry etch. The nanopillars are dry etched using a neutral planar discharge technique. The channels are sealed with a quartz cover plate. The micrographs show different aspect ratios of pillars (height to width, scale bar in each is 500nm): b-20, c-1, d-6, e-3. The last micrograph (F), shows defects in the nanopillars.

2.3 BIOLOGICAL APPLICATIONS

As the majority of the microfluidic systems described in this chapter are used to separate mixtures of biological molecules, we present a brief discussion of the importance of these molecules. Proteins, RNA, DNA, and cells are the key biological molecules at work in all living organisms [9]. Proteins are responsible for gene expression and regulation, for shuttling other molecules throughout cells, and for catalyzing biochemical reactions within cells (just to name a few key roles they play) [6, 10]. Analytical techniques used to separate proteins are useful for diagnosing diseases or for investigating when certain genes are turned on or off throughout the cell cycle [6, 11]. Similarly, techniques for separating mixtures of DNA molecules are useful for studying genetic variation, which is important for determining how individual genes function, elucidating the foundations of genetic diseases, or anticipating reactions to medicines [5]. Separating DNA by size is also useful for characterizing DNA libraries and is necessary to sequence DNA molecules or do forensic DNA fingerprinting [5, 12]. While we do not mean to ignore RNA and cells, most of the techniques described below focus on DNA and protein samples, so only these molecules will be described in any detail here.

DNA forms the genetic code of all living things [5]. Variations in DNA length or sequence (described below) are important indications of genetic differences or mutations, are indications of gene function (as observed via “knock out” experiments), and can be used in DNA fingerprinting applications [12]. Chemically, DNA is a polymer that is made up of four monomer constituents that can be arranged in any order along the entire length of the chain. The monomers are typically referred to as bases and are called individually: A (adenine), C (cytosine), G (guanine), and T (thymine). The

bases are of comparable molecular weight, and each is attached to the next by an identical piece of backbone. Therefore, the polymer mass is essentially proportional to the number of bases. The particular series of bases that form a DNA polymer is referred to as a sequence. DNA sequencing refers to the process of taking segments of DNA with unknown base composition and learning what that composition is [4, 5]. Sequencing DNA is useful for applications ranging from detecting genetic diseases to tracing evolutionary pathways.

DNA is found in both single- and double-stranded configurations. The single-strand is a single polymer chain, whereas the double-stranded version is composed of two single-strands wrapped about each other in a stable, helical configuration [13]. DNA only forms stable double-stranded configurations when each strand is the complement of the other. Complimentary base pairings are: A with T and G with C. In bioanalytical applications, both single- and double-stranded DNA molecules are of interest, and DNA polymer lengths commonly used in experiments range from tens of bases to millions of base pairs.

DNA is a charged polymer. Over most of the pH range, the backbone of a DNA polymer carries one free negative charge per base. Because both the charge and mass of the DNA polymer scale linearly with the number of bases, DNA molecules have a constant charge-to-mass ratio. This constant charge-to-mass ratio is important because it makes separating DNA molecules by length challenging.

As a polymer, DNA is well-described using the terminology of polymer physics. When in an electrolyte solution of sufficient strength, a DNA molecule's backbone charge is sufficiently screened by counterions in the

solution so that the molecule can relax into a blob configuration. A polymer blob is often described by a radius of gyration, R_g , which can be calculated from Flory's theory that takes into account the excluded volume of the polymer [14]

$$R \propto N^{3/5}, \quad (2.1)$$

where N is the total number of monomers. Another useful means of describing a polymer is by its persistence length, P . The persistence length of a polymer gives an indication of the stiffness of polymer (a large P means a stiffer polymer). A typical double stranded DNA molecule has a width of 2nm and the monomer length is 0.34nm [5, 15]. Single-stranded DNA has a persistence length of ~ 3 nm, whereas double-stranded DNA has a persistence length of ~ 50 nm. The persistence length is dependent upon the salt concentration [16].

As an electronegative molecule, DNA in solution can be moved with electric fields. This technique is called electrophoresis. When an electric field is established in a fluid containing DNA molecules, the molecules move toward the positive electrode. To account for variability in the electrophoretic velocity caused by variations in environmental parameters such as salt type and salt concentration in the buffer, molecular mobility is typically cited in lieu of molecular velocity. The mobility is related to the velocity by

$$v = \mu E, \quad (2.2)$$

where v is the velocity of the molecules (cm/s), E is the applied electric field (typically measured in V/s) and μ is the mobility ($\text{cm}^2/\text{V/s}$).

Unfortunately, in a solution free of obstructions, DNA molecules of different lengths almost always move with the same velocity [17-19]. This is unfortunate because if they had an inherent size-dependent velocity, then separating DNA molecules by length would be much easier than it is. Most

DNA molecules migrate with the same velocity because both the charge and the mass of the molecules scale directly with the length of molecules. Thus, while the electromotive element (the charge) increases as the molecules get longer, so too does the drag (which directly related to the mass). This phenomenon, referred to as the free-draining property of DNA, is the primary reason why so much effort has been put into developing sieving matrices like slab gels or microfluidic obstacle courses [18-20]. These restrictive physical environments impart DNA molecules with size-dependent velocities generally through friction, but not always, as will be highlighted later.

Proteins are also polymers, but are made of combinations of 20 different monomers known as amino acids [6]. The amino acids are also not all negatively charged. Each amino acid of the protein polymer can have one or multiple ionizable hydrogen atoms. Therefore, across a range of pH values, proteins can have dramatically different electrical properties. Additionally, amino acids are much more disparate in size than are the four DNA bases. Thus, proteins do not have a constant charge-to-mass ratio. Some analytical techniques take advantage of the variability of proteins' charge-to-mass ratio to directly separate proteins by free solution electrophoresis [6]. Another analytical technique that can be used to separate proteins is isoelectric focusing [6]. With this technique, a pH gradient is established in a column through which proteins are electrically driven. Ionization occurs at various points along the pH gradient for different proteins, and at particular pH each protein becomes electrically neutral and stops moving. Direct electrophoresis of proteins and isoelectric focusing are useful, but are not always helpful for samples of interest and are not always capable of adequately resolving mixed samples. In these cases, proteins can be immersed in a buffer containing a

constant charge-to-mass ratio molecule that uniformly binds along the protein polymer chain (such as sodium dodecylsulfate or urea). These so-called denaturants impart all proteins with essentially the same charge-to-mass ratio. Then, sieving matrices similar to those used to separate DNA molecules by size can be used to separate the protein mixture by size.

Proteins and DNA are ubiquitous as specimens for biological assays because they are at the heart of many biological processes and diseases. DNA sequences encode genes that are turned into proteins, so mutations in DNA can cause more-, less-, or non-functional proteins to be created [9, 10]. Any of these deviations from normalcy has the potential to cause drastic, observable biological consequences (such as disease) [11]. Thus, analytical techniques such as separating DNA molecules by size are used to detect disease-causing mutations. Proteins are truly pervasive in biological processes. Proteins are the worker-molecules that perform diverse biological tasks such as packing and unpacking DNA from its storage place in cell nuclei, transcribing DNA into RNA which then gets translated into new proteins, transporting molecules across cell membranes, and participating in metabolic processes that convert stored fuel into usable energy [6, 9]. Protein separations are used to detect the presence of proteins at various points in the cell cycle or to detect mutated forms of proteins. Protein assays are critical for understanding what exactly proteins do and what happens to biological systems when proteins do not do what they are supposed to do. For these reasons – and many more which were omitted for brevity – there is tremendous interest in developing tools for separating proteins and DNA.

The ability to use CMOS fabrication techniques to manufacture microfluidic channels in silicon and glass chips has enabled miniaturized and

improved versions of well-established biological and chemical techniques. Additionally, these microfluidic chips afford new analytical techniques. Separations of biomolecules by a range of physical properties are possible. Microfluidic filtration systems can be used to remove unwanted constituents of a complex mixture as well as concentrate and localize critical constituents that are often present at only a fraction of the concentration required for quantitation. Most or all of the research effort in microfluidics is in some way directed at achieving a so-called micro-total-analytical-system (μ TAS) or lab-on-a-chip.

The allure of a μ TAS is that there are potentially significant advantages over traditional systems. Very low sample volumes can be used, thus reducing the amount of reagents needed to perform experiments. Additionally, single molecule fluorescence imaging techniques permit extremely low concentrations of analytes to be detected in microfluidic channels. As microfluidic cell handling techniques improve and on-chip PCR and filtration are better refined, we will see more and improved experiments in which an individual cell is loaded into a chip reservoir and its DNA or proteins sorted and quantified. A μ TAS has the potential to be massively parallel, dramatically improving analysis throughput. Improved heat dissipation, leading to better resolution, is another μ TAS advantage. And, increasingly, key analytical components such as optics and detectors are being fabricated in such a way as to be packaged directly with the microfluidic channels. All of these advantages are driving the effort to develop μ TAS technology that is widely deployed in the medical and research communities.

2.4 MICROFLUIDIC EXPERIMENTS

Chip-based microfluidic devices have emerged over the last decade as viable – and perhaps superior – platforms for separating biological molecules. Microfluidics, as exemplified by the promise of μ TAS technology, have the potential to perform “classic” biological separations using fewer reagents, in less time, and with better resolution than current methods can deliver. A diagram of a typical microfluidic channel is shown in Figure 2.4. Figure 2.4A shows a top-down view of a standard, crossed-channel design used for separating biomolecules based upon size, charge, or affinity to a material in the separation channel. Analytes would typically be loaded into reservoir 1 and driven towards reservoir 2, filling the intersection (Figure 2.5). Well-defined plugs of the sample are injected into the separation channel, which is the channel extending from the intersection to reservoir 4, by switching the direction of the flow to point from reservoir 3 to reservoir 4. In almost all circumstances, reservoirs 1 and 2 must be “back-biased” to prevent leakage of sample from these side-channels into the separation channel.

A generic schematic of a laboratory-based experimental setup is shown in Figure 2.6. The chip containing the microfluidic channels is placed upon a microscope (typically an inverted microscope to allow for facile introduction of wires and tubing to the reservoirs on the chip). The microscope is equipped with a broad-spectrum light source such as a mercury arc lamp for fluorescence illumination. Lasers can also be used to illuminate fluorescently labeled biomolecules. Biomolecules can readily be labeled with fluorophores that have well-defined excitation and emission wavelengths. Bandpass or longpass filters are used to select wavelengths of light near where fluorophores are excited and emit fluorescent light. A CCD or photomultiplier is

generally used to collect the photons emitted from the fluorescent molecules. The detector is positioned at some point along the separation channel and measures intensity or absorbance of the analytes as they are illuminated by the light source. Bio-separations are typically quantified with intensity versus time data from which other important values such as analyte mobility or abundance are calculated.

A schematic side-view of a reservoir and the access hole into the microfluidic channel is shown in Figure 2.3B. Though pressure-driven flow is sometimes used in microfluidic experiments, electric fields are typically used to move either the liquid (electroosmotic or electrokinetic flow) or the analytes in the channel (electrophoretic flow). Electrodes from a power supply are placed in the reservoirs to establish an electric field in the microfluidic channels (sometimes these electrodes are integrated onto the chip through the fabrication process as in [21]).

A cross-section of a microfluidic channel, as seen looking along the direction of the channel, is shown schematically in Figure 2.4C. The channel width, w , is typically defined and set lithographically, so it has dimensions between tens of nanometers (electron beam or electrospinning techniques) and tens of microns (photolithography). The channel height, h , is usually established through etching or a sacrificial layer process. Micron-scale depths are typically obtained with chemical etches such as hydrofluoric acid for glass substrates. Chemical etches are usually isotropic, so channels have rounded bottoms and sidewalls. If reactive ion etching is used to etch the channels, then a square channel bottom is achieved, and the height is usually a couple of microns down to tens of nanometers.

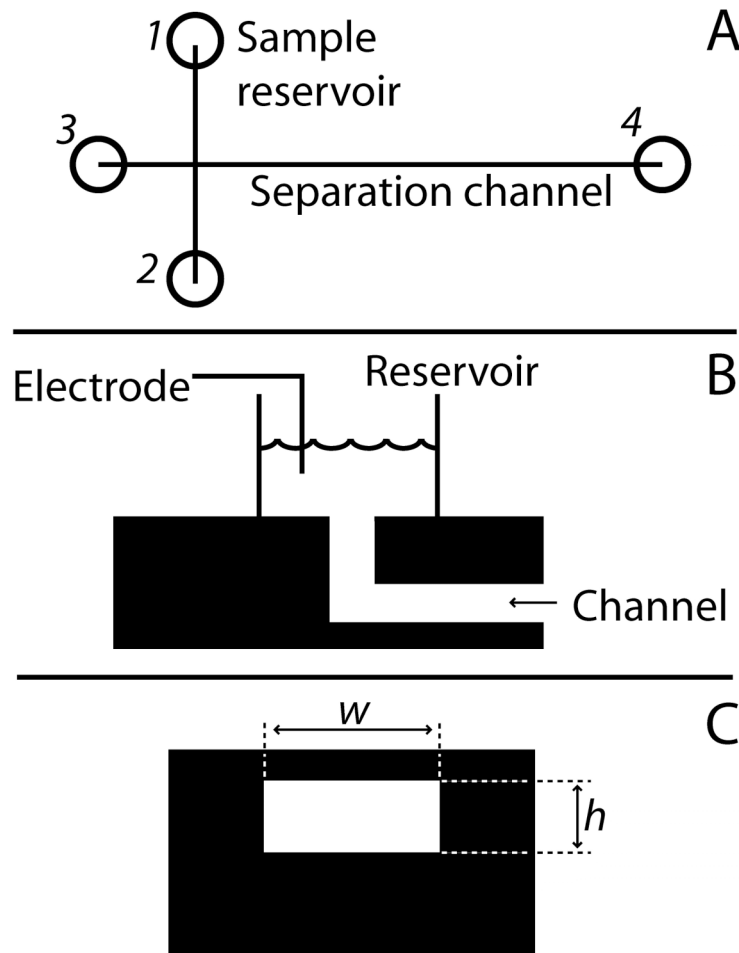


Figure 2.4: A) A schematic representation of a typical microfluidic device. One such device would constitute a microchip and tens to hundreds could populate a four or six inch wafer if carefully designed. Biological samples are loaded into one of the reservoirs (reservoir 1 in the figure). The channel from reservoir 1 to reservoir 2 is the “loading” channel. The channel from reservoir 3 to 4 is the “separation” channel. Pressure- or electrokinetic-driven flow is used to move biological analytes through the channels. B) A side-view of the interface between the macro- and micro-world. The reservoir is often a pipette tip glued to the chip. The access hole is a hole etched or drilled through the substrate in which the channels were fabricated. C) A typical square cross-section microchannel (that would result from reactive ion etching). The width, w , is defined lithographically and is limited only by lithographic resolution. The channel height, h , is established through the etching process. This height is limited by practical etch limitations, and is sometimes also limited by the method used to bond a cover to encapsulate the channels.

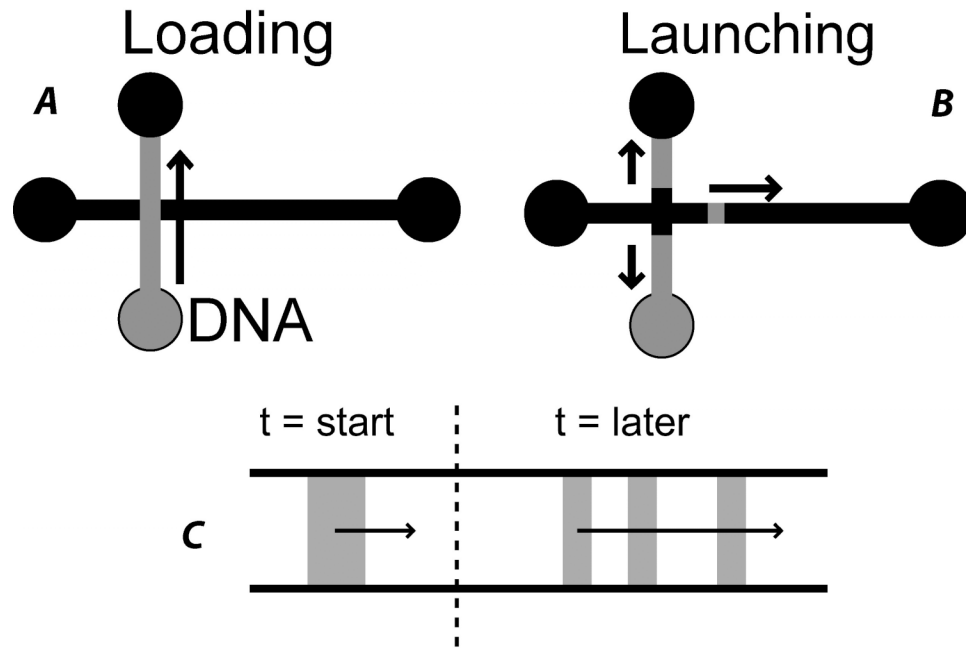


Figure 2.5: Schematics showing a typical microfluidic device and a DNA separation experiment. A) DNA is driven electrophoretically from one reservoir to another in the loading phase. B) The electric field is switched to direct a plug of DNA in the intersection to move down along the separation channel. In DNA separation experiments, the separation channel is typically filled with a sieving matrix. DNA near the intersection but not launched in the plug is typically forced to move away from the intersection with an electric field. This is done to prevent sample leakage into the separation channel. C) An example of the desired effect when a plug of molecules ($t = \text{start}$) is launched into a separation channel and separates into individual constituents ($t = \text{later}$).

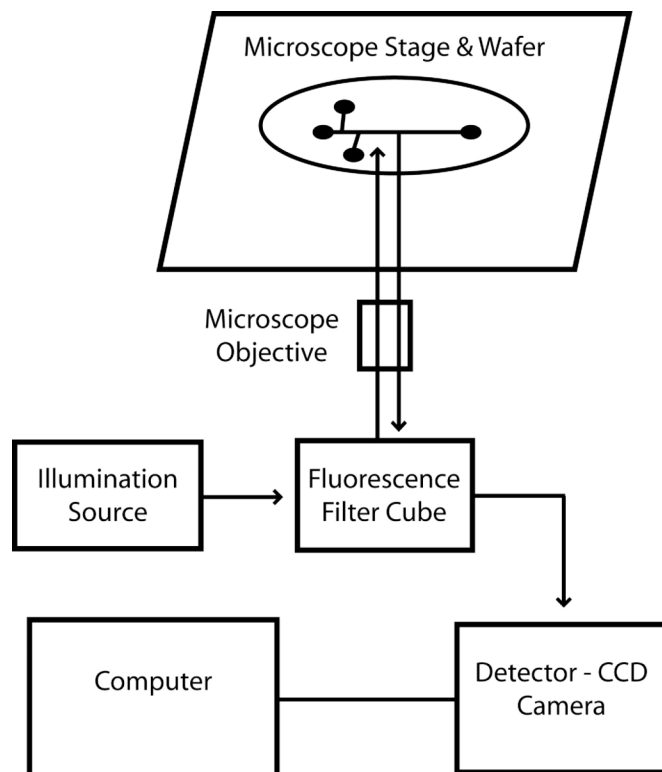


Figure 2.6: A schematic of a typical microfluidic experimental setup. A microchip or full wafer containing microfluidic devices is mounted on a microscope stage. A broad-spectrum light source or laser is typically used to illuminate fluorescently labeled molecules in the microfluidic channels. A photodetector such as a CCD camera or photomultiplier tube is used to quantify the emitted intensity from the interrogated molecules.

The last step in most microfluidic fabrication processes is the bonding of a cover wafer to the processed wafer containing the channels (this is typically not necessary in sacrificial layer processes). Once the channels are sealed, they must be filled, and this is not always a trivial process (though a new, super-critical wetting technique was just reported [22] that is capable of filling even otherwise difficult to fill channels). When all of the channel dimensions are at least $1\ \mu\text{m}$, the filling process is usually straightforward. Whatever buffer is to be used for experiments can be directly introduced into the channels. The channels will fill by capillary force with few air bubbles. Once the channels are filled, any trapped air bubbles dissolve over time or can

be driven out with electroosmotic flow (described later). Channels with a dimension that is less than $1\mu\text{m}$ are more difficult to fill. Significant numbers of air bubbles form, especially in long channels or near intersections and corners. Additionally, even relatively large channels that have features such as pits, grooves, lateral pockets, or slits can be expected to require at least some massaging to remove trapped air bubbles. Low surface tension solvents, such as ethanol, can be used to help mitigate the formation of air bubbles in microfluidic channels.

Once a continuous fluid path is established between two reservoirs, an electric field can be used to help drive fluid through the channel. This can be done even in the presence of large bubbles and is often necessary to dissolve or drive out bubbles. Though capillary force is a convenient means of filling microfluidic channels, pressure can also be used to hasten the process. Sometimes pressure is necessary due to complicated channel geometries or because air bubbles are difficult to eliminate passively. Both positive and negative pressure can be used if appropriate reservoirs are securely fixed to the microfluidic channel access holes.

The interface between the macro-world and the micro-world is important, especially when thinking about a μTAS . In the research environment, microfluidic channels are most frequently made in chips or wafers with at least a 1cm^2 footprint. The only access point between the big world and the small world is through the reservoir. Reservoirs are typically made from cut pipette tips glued around an access hole in the wafer. Reservoirs made to withstand high pressures and made with standard thread gauges for pressure-compatible fittings can also be purchased from commercial vendors. In commercial applications, reservoirs are sometimes

nothing more than the access hole itself. Mechanized sample loading and electrode placement enables a direct connection to the microscale.

Furthermore, pressurized or sealed sample environments in commercial microfluidic devices prevent annoying effects such as evaporation, so significantly smaller volumes of liquid are needed.

Biological samples always require particular liquid environments in order to assume physically relevant forms. Proteins, for example, adopt complex structures that are meaningful and must be preserved for some types of experiments or eliminated for others. Buffer pH and buffer additives (such as sodium dodecylsulfate) can be used to control the structural properties of biomolecules. Of course, pH and additives often impact the electrical properties of the buffer, which subsequently affect the electrical properties of the microchannel surfaces, which finally affect the electrokinetics of the flow in the channels. For example, high ionic strength salt in a buffer significantly reduces the surface potential in glass microchannels causing decreased electroosmotic flow (bulk flow of liquid from the positive electrode to the negative electrode) [23-25].

There are primarily two types of flow used in microchannel experiments: pressure-driven flow and electrokinetic flow [26]. Each has associated advantages and disadvantages. The technique employed is often dictated by experimental conditions such as the buffer necessary for the biomolecules.

Pressure-driven flow can be used in almost all cases. Reservoirs must be securely affixed to the wafer in order to provide leak-proof sealing. Pressure-driven flow moves the bulk fluid through the channel carrying analytes along with it. Pressure-driven flow is relatively simple in that everything in the microchannel moves in the same direction. That is, positively

and negatively charged analytes move with the bulk fluid. This is a straightforward means of driving both fluid and analytes through microchannels.

One of the biggest drawbacks of using pressure to drive flow is that the liquid velocity profile is parabolic. This arises from the no-slip boundary conditions on the liquid at the channel walls [26]. The parabolic velocity profile automatically disperses analyte plugs across the channel width. Thus, experiments that rely upon discrete plugs of analytes being separated with high resolution do not lend themselves to pressure-driven flow. Corners, side channels, and obstacles are also problematic for pressure-driven flow setups. Flow instabilities can arise in channels that are not straight. These can lead to vortices, stagnation regions, and generally unstable flow. Pressure drops in the fluidic system must be well understood, because it is possible that the flow rates required for an experiment are not achievable with a given pressure setup (it might not be possible to achieve high enough pressures in the microfluidic channels for instance). Additionally, because many traditional biological experiments depend upon the electrical force to move charged molecules in response to an applied electric field, pressure-driven flow does not lend itself to performing certain “classical” biological experiments.

Electrokinetic flow involves moving the analytes, the bulk fluid, or both, by applying an electric field through the buffer. Electroosmosis is the term used to describe bulk fluid flow in a channel [27]. This phenomenon occurs when there is a surface charge on channel walls. SiO_2 channel walls, for instance, have a negative surface charge over most of the pH range. The surface charge leads to a wall potential (the so-called zeta potential) that decays into the channel where counterions in the buffer solution effectively

neutralize it. Near the walls, however, the surface potential is significant and draws counterions to it. These counterions are not tightly bound to the surface, however, and when an electric field is applied in the channel, they move towards the positive electrode. These counterions drag fluid along with them and the net effect is that the entire buffer solution moves toward the positive electrode. Unlike the pressure-driven velocity profile, however, the electroosmotic velocity profile is nearly uniform over most of the channel (assuming channels are more than about $1\mu\text{m}$ in their smallest dimension [23]). Thus, electroosmosis is quite effective at moving samples (via bulk fluid transport) with minimal dispersion.

Just as the counterions in the solution move towards the positive electrode, charged analytes also move. Negatively charged analytes move with the fluid toward the positive electrode, while positively charged analytes move against the fluid toward the negative electrode. Neutral molecules simply have the velocity of the bulk fluid. If the electroosmotic flow is strong enough, then all molecules will migrate in the same direction. The phenomenon of charged molecules moving in an electric field is called electrophoresis. The total mobility of electrokinetically driven molecules is

$$\mu_{total} = \mu_{EOF} + \mu_{EP}, \quad (2.3)$$

where μ_{EOF} is the electroosmotic (bulk) velocity, and μ_{EP} is the electrophoretic velocity.

Electroosmotic flow can be reduced or eliminated by minimizing the wall potential. Minimizing the wall potential can be accomplished with high concentrations of salt [25] or with surface coatings [8]. If electroosmotic flow can be minimized or eliminated, then purely electrophoresis is observed. There are some advantages to eliminating electroosmotic flow. If negatively

charged analytes are used, eliminating electroosmotic flow speeds up the overall analysis time (because the electroosmotic flow slows down the analytes). Electroosmotic flow is also somewhat unstable, especially in devices that have one dimension less than $1\ \mu\text{m}$ or in devices that have many intersections, corners, or otherwise complicated geometries. Because there is bulk fluid flow, there is the potential for stagnation points or vortices in the flow. These fluid effects are decoupled from electrophoresis, so it is possible to create very interesting (but usually not useful) analyte flow patterns when instabilities arise. Stagnation points and vortices are avoided when electrophoresis is used because the fluid does not move and charged molecules follow electrical field lines through the microchannels. These electrical field lines typically fill microchannels quite well [28].

In summary, the simplest microfluidic devices involve etching trenches in substrates such as glass or silicon. The fluidic channel is completed by sealing the etched substrate with a cover. The chip or wafer containing the microfluidic channel is mounted on a microscope with an illumination source and a detector. Biological samples are introduced to the microfluidic device via reservoirs that provide a gateway between the micro- and macro- worlds. Pressure or electrokinetic drive is used to move fluids and analytes through the channels where they separated. Analysis is accomplished by observing and quantifying what occurs within the channels or by removing processed samples from another reservoir and performing an off-chip analysis. These steps comprise the essential features of microfluidic experiments and are almost all necessary in any experiment.

2.5 MICROCHANNEL CAPILLARY ELECTROPHORESIS

In this section we describe initial efforts to miniaturize conventional capillary electrophoresis experiments. Microfluidic devices were fabricated that replicated the essential qualities of capillary systems. These early microfluidic chips incorporated electrokinetic sample handling protocols to facilitate easy sample manipulation within the microfluidic environment. Additional improvements over conventional capillary systems were realized through decreased detection limits and decreased analysis time.

One of the first steps towards miniaturizing conventional biological assays and developing a μ TAS was the work of Harrison *et al.* [29]. Over a decade ago, these researchers micromachined a glass substrate with 30 μ m wide channels for use in separating two charged, fluorescent molecules. The experiment was essentially the microfluidic analog of capillary electrophoresis. Their results indicated that glass substrates and microfabrication techniques could effectively be used to miniaturize capillary electrophoresis equipment. Furthermore, their results showed that microfluidics offered excellent fluid and sample handling characteristics. Rather than using pressure in conjunction with separate sample vials, they were able to introduce samples from on-chip reservoirs with electroosmotic pumping. Electrokinetic sample handling is significantly simpler than pressure-based methods and is very compatible with microfluidic systems.

They report their separation efficiency in terms of the theoretical number of plates (a common chromatographic measure of separation efficiency), and obtain a maximum number of theoretical plates for calcein of 35,000. This is comparable to conventional capillary electrophoresis methods. Finally, they estimate that their microfluidic separation system performs nearly

ideally in the sense that the only measurable dispersion is due to the finite size of the detector and the size of the injected sample plug. Joule heating and analyte-wall interactions play no role in band broadening.

Another effort to miniaturize conventional capillary electrophoresis experiments was conducted by [30]. One of their first reports describes a 2.5cm² glass chip upon which a serpentine channel was etched. This unique geometry enables much longer microfluidic channels to be made on a much smaller footprint. In addition to using a new geometry to minimize the overall chip-area, the group describes techniques for minimizing band dispersion caused by inefficient injection methods. In order to minimize the width of the injected analyte plug, it is necessary to apply appropriate voltages to all reservoirs, not just the sample loading and sample loading waste reservoirs. The separation reservoirs must be biased with voltage (as opposed to floated relative to ground) to prevent leakage during the loading phase. The group showed that these serpentine devices could be used to separate two fluorescent dyes as depicted in Figure 2.7.

Shortly after their work in 1992, Harrison *et al.* reported results showing the separation of six amino acids (the monomer units of proteins) in similar microfluidic channels [31]. Results of the amino acid separation experiment are shown in Fig1.8. The reported separation efficiency was 40,000 to 75,000 theoretical plates, as compared to 400,000 theoretical plates reported in conventional capillary electrophoresis experiments [32]. While the microfluidic system's separation efficiency is an order of magnitude lower than the capillary system, the microfluidic-based experiment takes about 15 seconds while the conventional experiment takes about 15 minutes.

In 1995, Jacobsen *et al.* used fused quartz microchips to electrophoretically separate metal ions bound to 8-hydroxyquinoline-5-sulfonic acid [33]. The researchers used zinc, cadmium, and aluminum, all of which possessed a net negative charge in solution. Because the negative charge on the metals would cause the metal electrophoretic mobility to be in the opposite direction as the bulk fluid electroosmotic mobility, the researchers coated the channels with linear acrylamide. This coating, which is applied by flowing acrylamide through the channels and covalently linking it to the negatively charged fused quartz surface prior to electrophoresis experiments, has the effect of suppressing the zeta potential which in turn essentially eliminates electroosmotic flow of the bulk fluid. When only negatively charged analytes are used in electrophoresis experiments, it is generally recommended to eliminate the bulk electroosmotic flow to increase analyte mobility and decrease analysis time. The researchers were able to separate the three metal complexes in about 15s. Owing to the very low background fluorescence of the fused quartz microchip, quantities of metals as low as 46, 57, and 30ppb for Zn, Cd, and Al respectively. Similar experiments done with conventional capillary electrophoresis systems result in detection limits from 46 to 613ppb in times of at least two or three minutes [34].

These initial microchip-based capillary electrophoresis experiments all involved separations of molecules with different charge-to-mass ratios (or quantification of charged molecules in the case of [33]). No sieving matrix was present in the microchannels. When electrophoresis is performed in capillaries or channels with no matrix, the process is typically referred to as free solution electrophoresis. When the charge-to-mass ratio of molecules is different, then free solution electrophoresis is capable of separating the molecules given

enough resolution or channel length. For proteins in their native conformation (or amino acids) or for biomolecules that can be selectively bound to “carrier” molecules of different charge-to-mass ratios, free solution electrophoresis is typically sufficient for separation. For DNA or denatured proteins (which have a constant weight and charge molecule bound along the entirety of the polymer), free solution electrophoresis is not capable of effecting length-based separation. A sieving matrix must be introduced to break the so-called charge-to-mass symmetry. Slab gels of agarose or polyacrylamide are typically used to separate DNA and denatured proteins. Agarose, polyacrylamide, and similar substances can be introduced into microfluidic channels creating microfluidic analogues of gel electrophoresis techniques. These gel-filled channels are discussed in the next section.

2.6 FILLED MICROFLUIDIC CHANNELS

With the initial success in miniaturizing capillaries to the microchip format, researchers moved to improve the performance of microchip devices. For capillary electrophoresis or microchannel-based electrophoresis experiments improved performance generally means increased sample resolution. As capillaries had been filled with sieving matrices to improve their resolving power, so too were microfluidic channels filled with sieving matrices. Just as filling capillaries with viscous polymer solutions is difficult, so too is filling microfluidic channels. A number of techniques for filling channels have been developed and here we will describe the basic methods as well as some of the successes of filled microfluidic channels in rapidly separating biomolecules.

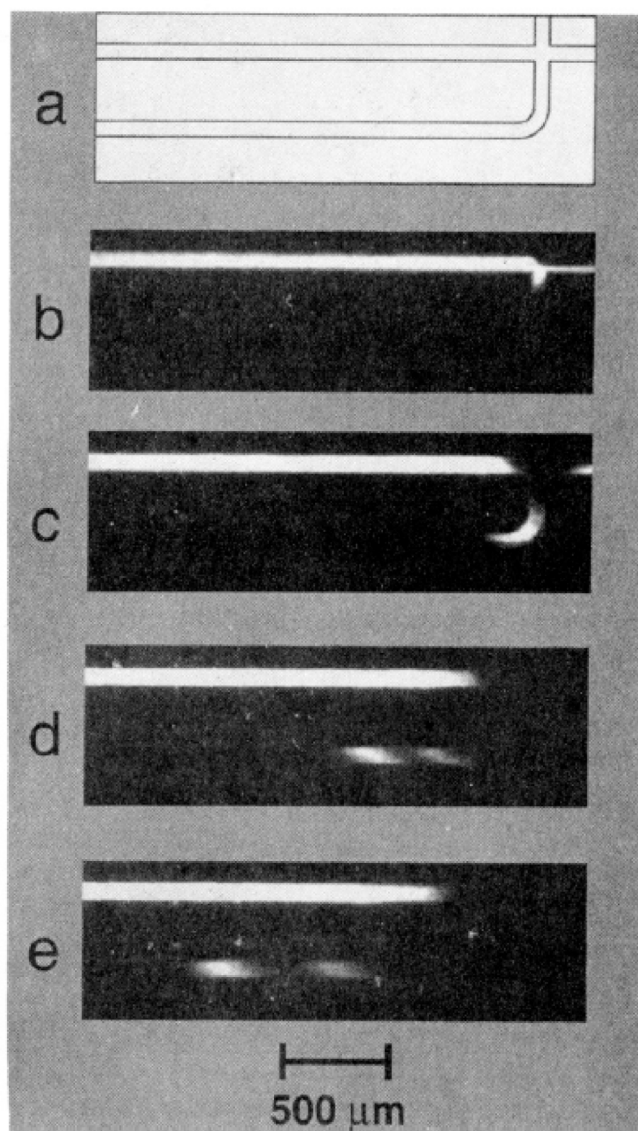


Figure 2.7: A five panel collage of optical micrographs of the serpentine device described in [30], reprinted with permission from [30], Copyright 1994 American Chemical Society. A) bright field image of the intersection of the loading and separation channels. The beginning of the serpentine separation channel extends to the bottom and bottom-left of the image. B-E) 1 s interval fluorescent images of plug injection and separation. B) Loading fluorescent dye through the intersection. C) The plug just after injection into the serpentine separation channel. D) The plug has separated into its two constituents, rhodamine (faster) and sulforhodamine (slower). E) The samples are fully resolved. Note that the slight back-bias along the loading channel has drawn the sample in the loading channels away from the intersection, preventing sample leakage into the separation channel.

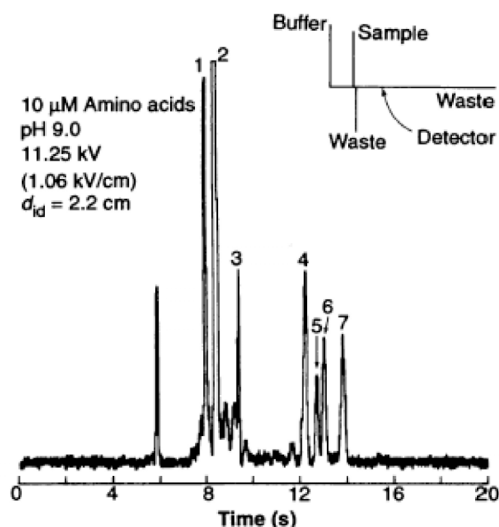


Figure 2.8: Results showing the separation of six amino acids in a microfluidic device, reprinted with permission from [31], Copyright 1993 AAAS. Peaks 1 and 3-7 are the amino acids. Peak 2 is a reactive by-product involving the fluorescent dye used in the experiments. The unlabeled peak at ~6s is not mentioned in the paper. The schematic in the upper right portion of the image shows the channel configuration. Translating the inset names into the name of Fig. 3,A, ‘sample’ is ‘1’, ‘buffer’ is ‘3’, (lower) ‘waste’ is ‘2’, and (right) ‘waste’ is ‘4’. Electrokinetic pumping is used to move analytes throughout the microfluidic network. The separation efficiency of the microchip capillary electrophoresis device is about 50,000 theoretical plates which is comparable to conventional techniques.

There are basically two types of polymer solutions that can be used to fill microfluidic channels: polymers that are cross-linked to form a gel-like matrix, and linear polymers that do not cross-link. For polymers that cross-link to form gels, the viscous nature of the gels makes introducing gels into microfluidic channels difficult. Due to the laminar nature of microfluidic flows, unless geometries are specifically chosen to force mixing to occur, mixing is typically difficult to achieve inside the microchannels. Therefore, chemical cross-linking agents can only be used if channels are filled immediately after all chemicals are mixed and a rapid, reliable channel-filling procedure is used.

Then, because gelation of the matrix begins outside of the microfluidic channel, pressure-filling the channels with the mixture is usually necessary. Filling the channels with the polymer and then trying to achieve mixing of the cross-linking agent via diffusion is too slow to be practical. To overcome the problem of filling channels with a viscous polymer solution that is in the process of forming a sieving matrix, researchers often use photoinitiation to induce the gel-forming chemical reaction. Photoinitiation works for most polymers, such as polyacrylamide, and is relatively straightforward to implement. In gel-filled channels, analyte separation is achieved via transient entanglement of the analyte upon the gel fibers, through frictional interactions between the analyte and the fibers, or through the process of an analyte hopping between restrictive regions and voids (a process discussed in Section 2.7.3).

Linear polymer solutions are generally easier to introduce into microfluidic channels than gels. If not too viscous, these polymer solutions can either be pressure-driven into microfluidic channels or carried into and through channels using electrokinetic pumping. Linear polymers that are frequently used are linear acrylamide or hydroxyethylcellulose. Numerous others exist as well (see, for example, the review [35]). Typical polymer concentrations in solution range from 0.05% to 2%. For linear polymer solutions, separation typically occurs as a result of transient entanglement of analyte molecules with the polymer fibers. Because the polymer fibers are not linked to each other or to the channel wall, they can be dragged by the analyte molecules through the microchannel, slowing down the migration of the analytes.

The reason one fills a microfluidic channel with a polymer solution (whether it is cross-linked or not) is to increase the resolution of biomolecular

separations. When DNA and proteins are to be separated, for instance, a sieving matrix is almost always required to facilitate size-dependent mobility differences. Because DNA has a nearly uniform charge-to-mass ratio, frictional interactions with polymer solutions or gels must be used to separate mixed samples of molecules by size. Proteins to be separated by mass are often denatured with chemicals like sodium dodecylsulfate, which effectively renders all proteins globular and of similar charge-to-mass ratio, so a sieving matrix is required to separate these molecules as well.

In one of the first reported realizations of a microchip-based gel electrophoresis system, Effenhauser *et al.* separated single-stranded DNA oligonucleotides 10-25bases in length [36]. Though slightly modified in layout, their devices had essentially the same injection and separation geometry that has been previously discussed. Electrophoresis was used to move samples throughout the microfluidic channels. The researchers were able to separate DNA oligomers differing in length by a single base in a 10% polyacrylamide gel, a similar concentration to what would typically be used in a conventional slab gel. The ability to resolve length differences for these short DNA fragments is potentially useful for analytical DNA techniques such as single nucleotide polymorphism detection or for screening short DNA fragments used in hybridization experiments. The separation takes approximately 40s in the microfluidic format, as opposed to tens of minutes in a conventional slab polyacrylamide gel. Additionally, the microfluidic format offers highly automated and reproducible electrokinetic sample injection. The researchers showed a series of repeated, back-to-back injections across which the migration times varied by less than 1% and peak heights varied by less than 2% (relative standard deviations).

Shortly after the work of [36], Mathies' group used a sieving matrix of hydroxyethylcellulose (HEC) to separate short DNA fragments in glass microfluidic channels [37]. Separations of ϕ X174/HaeIII digested DNA fragments were performed in microfluidic channels with acrylamide bound to the channel surfaces (to reduce surface interactions) and 0.75% (w/v) HEC in the separation channel buffer. The HEC matrix was pressure-driven into the separation channel. Researchers were able to separate the DNA digestion fragments in less than two minutes with resolution comparable to that of conventional capillary gel electrophoresis experiments. The microfluidic-based separation time is approximately ten times faster than possible with conventional techniques. The researchers report comparable run-to-run variability as with conventional techniques and with other microfluidic capillary gel electrophoresis experiments, and note that at least 75 consecutive separation experiments could be performed in the microfluidic channels without replacing the sieving matrix.

These works, and others, established that gel-filled capillary electrophoresis techniques could be miniaturized successfully. Many commercially available microchip separation products incorporate (usually proprietary or non-disclosed) sieving matrices in their fluidic channels. A wide range of polymers exist that can be more or less easily incorporated into microfluidic systems. One of the ultimate measures of system performance is whether or not long DNA strands (500-1000bp) can be separated with single base pair resolution. This is the resolution achievable with current capillary electrophoresis techniques employed to sequence DNA. Just as we examined the move to miniaturize free solution and gel-filled capillary electrophoresis techniques, we briefly discuss the effort to miniaturize sequencing techniques.

One of the primary motivations for developing microchip-based capillary gel electrophoresis technology was to speed up and reduce the cost of sequencing DNA. During the 1990s, the Human Genome Project was begun with the goal of sequencing the entire human genome [4]. The project was actually completed ahead of the original schedule because of new technology (capillary electrophoresis and computational techniques) that was developed and implemented within the timeframe of the project. It was recognized by astute researchers that the potential benefits of microfluidic technology (such as decreased sample volumes and sample handling, automation, and decreased analysis time) for highly demanding sequencing applications were worth investing time and effort into developing.

One of the first demonstrations of a microchip device capable of achieving single base resolution for sequencing was published in 1995 by Mathies' group [38]. In their work, they used polyacrylamide-filled microfluidic channels for fully resolve (at the 0.5 resolution level that is standard for declaring adjacent peaks resolved) single stranded DNA fragments differing by one base out to fragment lengths of about 150bases. A biochemical reaction is used to generate DNA fragments differing by one base where the DNA fragments are terminated by a fluorescent dye molecule. This fluorescent dye is correlated with the last base in the fragment. For example, fragments ending in the base A are red, fragments ending in the base T are blue, and so on. Sequencing is then a two-dimensional process. One separates DNA fragments by length and correlates the length information with the color information obtained in the detection process. A sample electropherogram from a sequencing experiment is shown in Figure 2.9. The gel-filled microfluidic channels were capable of a read accuracy of 97% over the fully

resolved region of 150bases. While not quite comparable to gel-filled capillary electrophoresis techniques available at time and used in the Human Genome Project (>99% read accuracy), the gel-filled microchannel results demonstrated that even the technically challenging task of sequencing DNA is possible in microfluidic channels.

Work towards developing microchip-based sequencing systems continues. Additionally, integration of detection and sample preparation steps are being incorporated into these microfluidic systems. The ability to manufacture micro- and nanoscale structures, however, has enabled researchers to explore entirely new separation mechanisms. It is to these new, fundamentally nanoscale systems that we now turn.

2.7 FABRICATED MICRO- AND NANOSTRUCTURES

The miniaturization of conventional bioanalytical techniques proved that microfluidics was a platform capable of competing with existing technology. Currently, work continues along the lines of miniaturizing conventional techniques and developing commercial products [39, 40]. Some of the most exciting bioanalytical work, however, has taken place in micro- and nanofluidic devices containing novel structures. Because of the ability to manufacture structures on the same size scale as the biomolecules, physical interaction mechanisms can be more carefully studied and new interaction mechanisms can be leveraged for separation applications. Below we describe a number of devices that are essentially nanoscale obstacle courses. These devices have found great utility in DNA studies and applications.

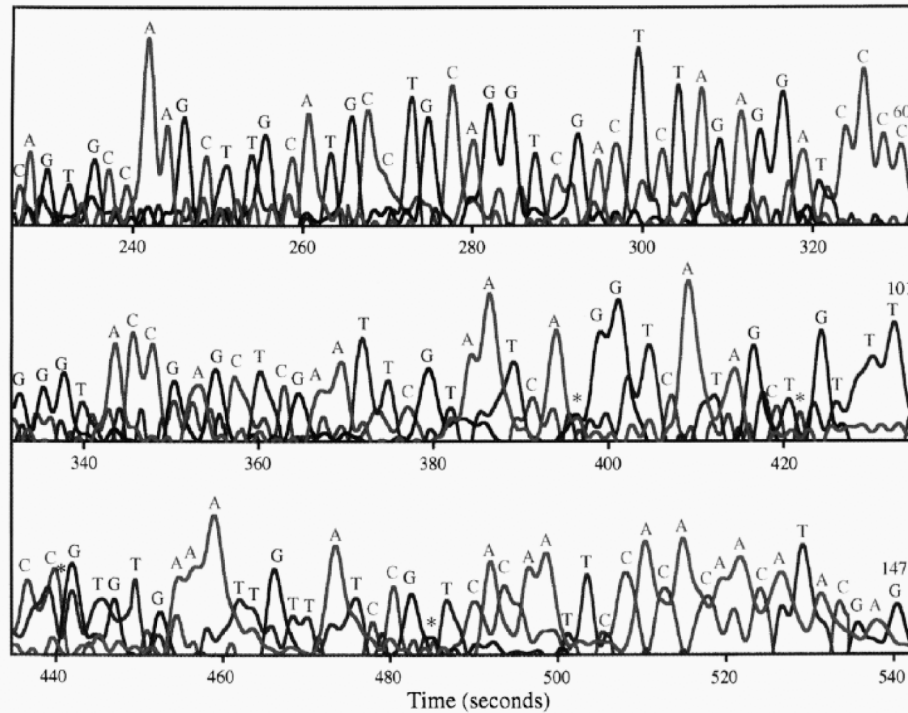


Figure 2.9: A black and white version of four color sequence data obtained using a microchip-based gel electrophoresis experiment, reprinted with permission from [38], Copyright 1995 American Chemical Society. Bases A, G, C, and T would normally be color-coded in the image to correspond to the fluorescent dyes attached to the DNA fragments that end with each base (bases and fluorescent dyes are matched during the sample generation process). The experiment was performed using a polyacrylamide gel in a microfluidic channel. Good resolution of peaks was obtained up to about 150bases before signal-to-noise in two of the color channels caused peak resolution to degrade below the 0.5 level required to “call” each base. 97% accuracy was obtained for the 150bases sequenced (asterisks denote the 3 bases that were incorrectly read, at times ~395s, ~440s, and ~485s).

2.7.1 Artificial Sieving Matrices

In one of the first reports of a microfabricated sieving matrix, Volkmuth and Austin describe a two-dimensional array of posts through which a variety of sizes of DNA molecules are driven [41]. Posts are patterned with optical lithography and have diameters of 1 μ m. The entire device (walls, floor and ceiling, and posts) is made from SiO₂. The post centers are spaced by 2 μ m

and they are 150nm tall. In their work, the authors deliberately shear 100kb DNA (~30mm contour length) to produce a DNA sample of mixed lengths.

When compared with an agarose gel typically used for separating long DNA molecules by size, the microfabricated post array corresponds to a very low concentration (~0.05%) gel that would not be stable. The radius of gyration of the longest DNA molecule is about 1.5 μ m which is comparable to the distance between the edges of adjacent posts. DNA molecules are observed to move through the post array and periodically collide with posts in such a way as to elongate around the posts in a rope-over-pulley fashion. This configuration results in both arms of the elongated DNA molecule being extended along the direction of the flow. Eventually, the longer arm of DNA will lead the disentanglement of the molecule with the post. Once disengaged from a post, the DNA molecule will relax into its blob configuration as it migrates through the array.

When longer molecules entangle upon posts they must spend more time extracting themselves from the posts. Thus, their net velocity through the array is smaller than that of shorter molecules. With fluorescent microscopy and a CCD, it is possible to observe individual fluorescently labeled DNA molecules in the post array. Individual molecules can be tracked and their velocities in the array determined. In their work, Volkmuth and Austin show that a nearly two-fold velocity difference is observed between the longest (~28 μ m or ~100kb) DNA molecules and the shortest (~3 μ m or ~10kb) DNA molecules.

This early work established the principle of using a microfabricated, artificial gel to separate DNA in essentially the same manner as conventional gels. A few years later, one of the same scientists, along with others,

established that pulsed field electrophoresis could be achieved in similar arrays of posts [42]. One advantageous feature of using microchip-based separation techniques is that it is straightforward to observe individual molecules migrating through the microfluidic channels. Thus, it is possible to carefully study physical phenomena such as molecular entanglement with obstructions, molecular response to the electric field, and what happens to molecules elongated in an array of pillars when the direction of the electric field is switch from being essentially parallel to the direction of molecular elongation to being perpendicular to the direction of elongation. This last point is particularly helpful in optimizing pulsed field electrophoresis experiments as there is a balance that must be established between switching frequency, duration, and electric field angles. With microfluidic systems and fluorescence microscopy, one is able to observe individual molecules as these parameters are adjusted and qualitatively get a feel for what is happening. Alternatively, the effects can be quantified by performing multiple separations using a variety of parameters and determining what combination of parameters produces the best resolution in the shortest time for the widest range of molecular sizes.

Sacrificial layer fabrication has also been used to manufacture microfluidic sieving structures (see Figures 2.2 and 2.10). In one of the first demonstrations of the process, Turner *et al.* used a sacrificial layer, patterned with electron beam lithography, to produce 100nm diameter posts separated by 100nm gaps extending 400nm between the floor and ceiling [43]. Figure 2.10 shows two cross-sectional scanning electron micrographs of the structures. The microfluidic elements of the device are made from silicon nitride and polysilicon is used as the sacrificial layer. These devices were used to measure the velocities of linear and circular DNA as it migrated through the

pillars under a DC electric field. The results indicate that circular, M13mp8 phage DNA (7kb) travels more slowly than does linearized lambda phage DNA (48kb) in the artificial gel. This is in contrast to what one would expect based upon gel electrophoresis of the same fragments. Typically circular DNA moves faster than linear DNA, and shorter DNA moves faster than longer DNA. The authors attribute the altered behavior to supercoiling of the circular DNA that might cause the DNA to entangle more readily upon pillars than linear DNA does. Additionally, if the supercoiling is insufficient to relieve stress in the DNA polymer, then the polymer may actually be stiffer than the linear DNA. This stiffness would probably cause DNA molecules to have a more difficult time moving through the array.

Artificial sieving matrices like those described above are necessary for μ TASs as putting gel-based sieving matrices in microfluidic channels is not always possible or desirable. Being able to combine the manufacturing of the microfluidic system with the creation of the sieving matrix greatly simplifies the entire production process. Furthermore, conditions not realizable in gel environments are possible with microfabricated structures. As individual molecules can readily be observed in these environments, polymer properties such as supercoiling and stiffness can be directly measured. Both of these latter properties are relevant for understanding how DNA is packed in cell nuclei and how genes are regulated.

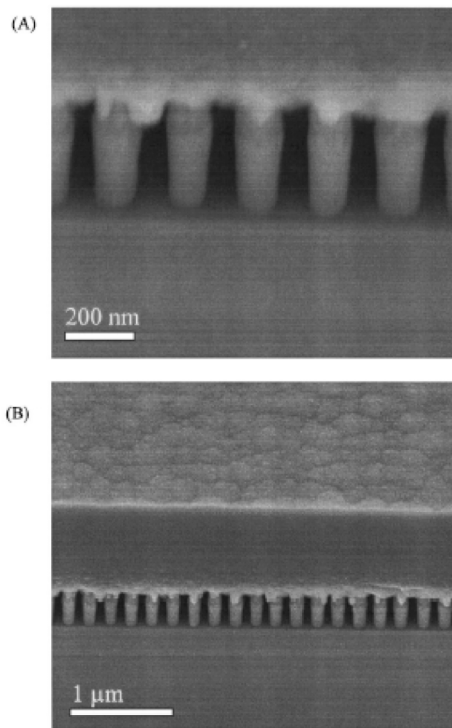


Figure 2.10: Scanning electron micrographs of a cross-section of an artificial sieving matrix fabricated using a sacrificial layer process, reprinted with permission from [43], Copyright 1998 American Institute of Physics. The image is taken at a 45° angle and shows the silicon nitride structures after removal of the sacrificial layer. The pillar aspect ratio is approximately 5:1.

2.7.2 Entropic Recoil

Turner *et al.* used essentially the same devices as described above to harness the configurational entropy of DNA molecules for separation [44]. A DNA polymer, being composed of flexible monomer units (the bases), exists in a relaxed blob configuration when in a spatial environment with dimensions larger than the radius of gyration of the molecule. When forced into an environment with dimensions smaller than its radius of gyration, the DNA molecule is squished into a more confined state. The molecule loses entropy. If the molecule straddles two regions, one in which the molecule is not squished and another in which the molecule is squished, there is an entropy

associated with each region. Assuming that the molecule is free to move, it will maximize its entropy by extricating itself from the region of low entropy.

This effect, dubbed entropic recoil, was investigated and used to separate DNA molecules of different lengths [44]. Pillar-filled regions were created using electron beam lithography and the sacrificial layer fabrication technique described previously. Pillars were roughly 35nm in diameter with a center-to-center spacing of 160nm resulting in gaps of about 130nm through which DNA molecules could move. The researchers used long DNA molecules (T2, T4, or lambda DNA) which have radii of gyration of at least 300nm. Thus, DNA molecules were forced to elongate to enter the pillar-filled region.

In entropic recoil experiments, DNA molecules are brought to the interface between a pillar-filled region and a pillar-free region (which has dimensions large enough that DNA molecules are in their relaxed, blob configuration). DNA are forced to partially extend into the pillar-filled region by applying an electric field. When the driving field is turned off, molecules that straddle the interface extricate themselves from the low entropy-pillar region. An example of this process is shown in Figure 2.11.

To separate molecules by length using this technique, a multi-step electric field program is used. First, a collection of molecules of different lengths is brought to the interface region using an electric field small enough not to drive the molecules into the pillar region. Then, a higher electric field is briefly pulsed to drive a portion of the molecules into the pillar region. The high field pulse duration is chosen to be long enough to push the shortest molecules into the pillar region. The short molecules that find themselves entirely within the pillar region do not see the high entropy region and remain within the pillar matrix. Longer molecules that straddle the boundary

experience the pull of the high entropy region and recoil into the high entropy region where they can relax. Subsequent gathering steps and high field pulses drive the short molecules already in the pillars through the pillar region and separate them from the long molecules. This process can be repeated with suitable high field pulses so as to separate molecules of different lengths from each other. Cabodi *et al.* separated T2 DNA (167kb) and T7 DNA (40kb) in an entropic recoil experiment [44]. Their experimental demonstration of the technique took hours, though this time could likely be significantly reduced by choosing electric field pulse durations more suited to the time required to drive DNA molecules into the pillar matrix. The authors speculate that based upon their results, a multi-stage entropic recoil separation device could be developed capable of separating DNA molecules in under an hour with 1% length resolution.

In the aforementioned entropic recoil experiments, polymers were observed to herniate in the pillars. This reduced the resolution of the entropic recoil separation technique. Recent work within the Craighead research group has focused on nanometer scale channels that preserve the advantageous entropy-reducing, confining effect but prevent molecule motion perpendicular to the driving electrical field. Using nanochannels as opposed to pillar-arrays prevents looping and herniation. These newer devices were fabricated with electron beam lithography directly in fused silica substrates, circumventing the need to use sacrificial layer fabrication. Mannion *et al.* showed that similar recoil and frictional effects are obtained in these nanochannel structures [45]. Additionally, because the nanochannel design prevented herniation, a much more detailed study of the motion of the DNA polymers in the confining regions was permitted. The scientists discovered that molecules enter nanochannels

stretched beyond their relaxed contour length. Furthermore, molecules often enter nanometer-scale spaces significantly folded. This means that in addition to a de-stretching process (caused by the initial over-stretching), and a recoil process (caused when the molecule straddles the boundary), there is also an unfolding process in which the molecule behaves much like a string sliding off of a table. An example of an unfolding process coupled with the entropic recoil process is shown in Figure 2.12. Similar channels were used by Reccius *et al.* to investigate the physics of DNA molecules in the nanochannel as they are compressed against an impenetrable constriction and then allowed to expand back to their full contour length [46].

Entropic recoil-based separation of DNA is an excellent example of a technique made possible through the use of micro- and nanofabrication techniques. No macroscale analogue technique exists. The physics of the polymers – their stiffness and entropy – can be studied directly with these devices. Additionally, long DNA molecules can be readily separated. A multi-stage entropic recoil separation device has the potential to eliminate diffusion-based band broadening, which is a ubiquitous resolution-limiting factor in conventional separation techniques.

2.7.3 Entropic Trapping

Entropy can be used in other ways to effect a molecular separation based upon length. Extensive theoretical work was done in the 80s and 90s that described the effects of confining environments on polymer diffusion, entanglement, and mobility [47-51]. Experiments in gels confirmed that when polyelectrolytes such as DNA are forced to move through entropically restrictive environments, the polymer mobility is not accurately described by

either the Ogston sieving model or the reptation model [52-55]. Instead, a regime of entropic trapping exists where molecules are effectively trapped in pores larger than their relaxed blob size and only periodically hop through restrictive areas into new pores.

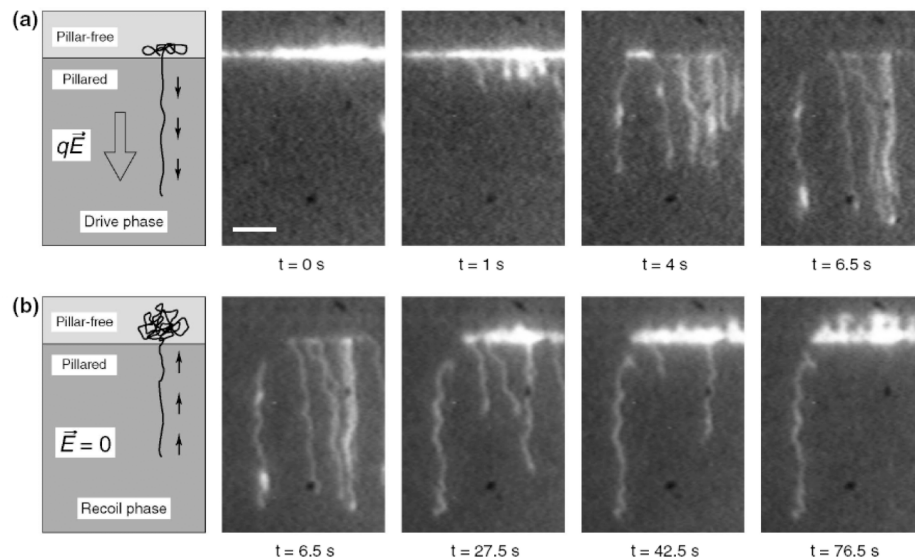


Figure 2.11: Schematics of the drive and recoil phases shown with fluorescence micrographs of T2 DNA molecules in the drive and recoil phases, reprinted with permission from [44], Copyright 2002 American Physical Society. A) In the drive phase of the process a high electric field is used to enable the molecules to overcome the energy barrier poses by the confining pillars. The boundary between the pillar-free and pillared regions shown in the schematic is at the same place as in the micrographs to the right of the schematic. During the drive phase, molecules are driven into the pillared region. The initial insertion is probabilistic in nature, so not all molecules enter at the same time. Thus, for a given drive duration, some molecules may end up straddling the boundary. B) In the recoil phase the driving field is turned off. Those molecules left straddling the boundary are essentially driven out of the pillared region by the high entropy of the pillar-free region. After 76.5s, all molecules straddling the boundary have recoiled and one molecule that was fully inserted remains in the pillared region.

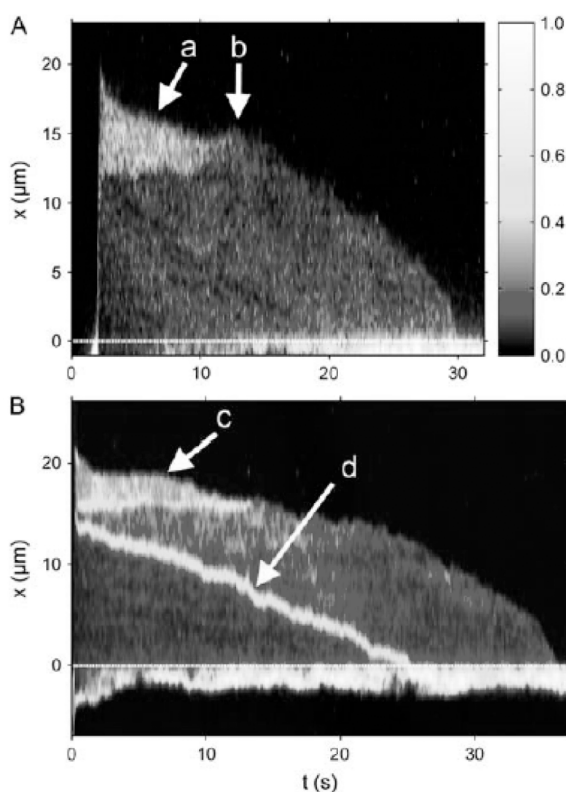


Figure 2.12: A time-series of intensity images along nanochannels in which T4 DNA molecules are inserted, reprinted with permission from [45], Copyright 2006 Biophysical Society. The vertical dimension shows the intensity along the length of the molecule. Bright parts of the graph correspond to more dyed DNA than do dim parts of the graph. The horizontal dimension shows the time evolution of the molecule in the nanochannel. The dashed white line at $x=0$ marks the boundary between the regions of high and low entropy. A) A DNA molecule is driven into the nanochannel region at about $t=2$ s. It is initially inserted about $20\mu\text{m}$ into the channel and straddles the high and low entropy interface (the dashed line at $x=0$). Once the molecule is inserted the field is immediately turned off and the molecule is left to recoil. Note the high intensity region near the far end of the molecule ($13\text{-}20\mu\text{m}$). This portion of the molecule is folded-over on itself, an occurrence that is not uncommon when long molecules are forced into nanochannels. The molecule simultaneously undergoes relaxation, unfolding, and recoil. The relaxation process is very fast and most evident from $t=2$ until about $t=5$. The unfolding process occurs until 'b', at which point the remaining folded portion flops open. From 'b' onwards, the motion is entirely recoil as the molecule extricates itself from the nanochannel. B) Another molecule inserted into a nanochannel undergoing relaxation, unfolding, and recoil. Additionally, the molecule contains a knot that never unties. The knot is apparent as the short, bright segment that recoils with the leading end of the molecule (highlighted by the arrow 'd').

Well-characterized, “ideal” periodic structures were used in modeling the motion of polymers through restrictive environments, yet the experimental work involved random gel-matrices similar to those conventionally used to separate DNA molecules by length. It was not until the work of Han *et al.* that a lithographically defined array of entropic traps was used to show that DNA molecules are trapped and can be separated by length in a real “ideal” structure [25]. In their first work, Han *et al.* showed that 40kb DNA molecules and 160kb DNA molecules exhibit significantly different trapping times when forced to hop across barriers and into large “pores”. Subsequent research showed that the mobility difference caused by the difference in delay times at each trap was sufficiently large to separate these molecules by length in a device 1.5cm long containing thousands of traps. In a variety of experiments with so-called entropic trap arrays, Han *et al.* were able to separate a wide range of DNA lengths [56, 57]. T2 and T7 phage DNA (160kb and 40kb respectively) were separated in 15 minutes in an entropic trap array. A comparable experiment using pulsed field gel electrophoresis would have required between 12 and 24 hours. Additional experiments showed that DNA from 5kb to 40kb could be separated in about 30 minutes with resolution comparable to that obtained using gel electrophoresis.

As originally described, entropic trapping relies upon an energy barrier and interfacial contact between a molecule and that energy barrier. DNA is a flexible polymer that has a characteristic radius of gyration set by the total number of bases in the polymer chain. When a relaxed blob of DNA is forced against a constriction in a microfluidic channel by an electric field, the blob makes interfacial contact with the restriction. This contact area is proportional to the radius of the blob: larger molecules “contact” the gap more than do

small molecules. The molecule is subjected to two forces: an electric driving force and an entropic force discouraging it from entering the restriction. This free energy landscape is depicted in Figure 2.13. The entropic barrier energy is sharp and significant. However, once a portion of the molecule overcomes the barrier, the large electric field in the restricted region pulls the entire molecule into the restriction and toward the next open region. Because the DNA molecule is “free draining” to both the electric field and whatever fluid flow is present, the process of entering the restriction is local in nature. Portions of the molecule randomly diffuse near the entrance to the restriction and when one happens to find itself on the downhill side of the energy landscape, it is pulled in and the rest of the molecule follows. To summarize: larger molecules have more interfacial area with the restriction and make more attempts to enter the high field shallow region. Consequently, larger molecules move between restrictions more readily than do smaller molecules.

Quantitatively, the following model was proposed to describe the entropic trapping process [58]. The energy landscape is composed of an electric and entropic component

$$F \sim xT - x^2E, \quad (2.4)$$

where x is the distance the molecule has penetrated the shallow region, T is the temperature, and E is the electric field. Equation 2.4 represents the energy barrier that must be overcome to pass through the restriction. The probability of escape is then given by

$$P = a \exp(-\Delta F / kT), \quad (2.5)$$

where k is the Boltzmann constant, and the prefactor a depends upon the number of escapes attempted (that is, the interfacial area). Equation 2.5 is the crux of the size-dependence in entropic trapping: the prefactor contains all of

the size-dependence while the exponential term represents the thermodynamics of the energy barrier and does not depend on any aspect of the molecule. The time molecules remained trapped is given by

$$\tau = \tau_0 \exp(\Delta F / kT) = \tau_0 \exp(b / E_s kT), \quad (2.6)$$

where t_0 is the size-dependent prefactor, b is a geometric constant, and E_s is the electric field at the edge of the shallow region. From the trapping time, the mobility can be written

$$\mu = \frac{\mu_0}{1 + \tau / t}, \quad (2.7)$$

where t is the time required for a molecule to move through a distance equal to the length of the restriction if the restriction were not there. The length dependence in the mobility comes from t and the length dependence is such that longer molecules migrate faster than shorter ones. Later work by Han *et al.* confirmed the applicability of the model over a wide range of DNA lengths and discussed optimizing the device for maximizing resolution and separating chromosomal-length DNA [56, 57].

After the original entropic trap array separation experiments were published, a new wave of theoretical and experimental papers surfaced [59-61]. In the first of such theoretical comparisons, Tessier *et al.* confirmed that the model proposed by Han was essentially correct in that Monte Carlo simulations based upon Han's model produced results qualitatively similar to the experimental results [59]. The shapes of the experimental and theoretical mobility versus electric field graphs, for instance, are identical. Furthermore, the essential physical mechanism of escape – herniation of a portion of the molecule into the restrictive region leading to the entire molecule moving through the gap – is confirmed by the theoretical results. Chen and Escobedo examined wider ranges of molecule sizes and electric field strengths than

were examined experimentally [60]. Even though their results indicate that the physical model proposed by Han *et al.* might not fully describe the system at low electric fields or for very short DNA molecules, their simulations match Han's results for the conditions used in experiments. Additional simulations by Streek *et al.* showed that there might be a second, independent physical mechanism contributing to the time molecules spend migrating between restrictions [61]. In their simulations, they show that while in transit across the deep regions, molecules can diffuse out of the high field region of the channel. That is, molecules can diffuse into the corners of the entropic traps where the electric field is weak. In the corners, molecules are effectively left to diffuse back into a region of higher electric field. This phenomenon operates on a much slower time scale than the mechanism proposed by Han *et al.* and was probably not observed because of the sizes of molecules and electric field strengths used in their experiments.

Entropic traps separate DNA molecules by length and have been used to separate quite long DNA molecules. This artificial sieving matrix is straightforward to fabricate and has great potential as a separation matrix within a μ TAS environment. The entropic trap array could potentially be used to handle the large DNA molecules that would be released from a cell lysed within a chip. Judicious use of entropic trap-like restrictions could also be used to separate or filter cellular debris and proteins from the DNA. Recent work has shown that by using very thin shallow regions in entropic trap array-like devices, one can separate very short DNA molecules and proteins [62, 63]. Thus, the general model of patterning very narrow restrictions followed by relatively large gaps can be used for biological applications across a wide

range of biomolecular sizes. This broad-utility is exactly what is needed for μ TAS systems that start with whole cells and end with useful analytical results.

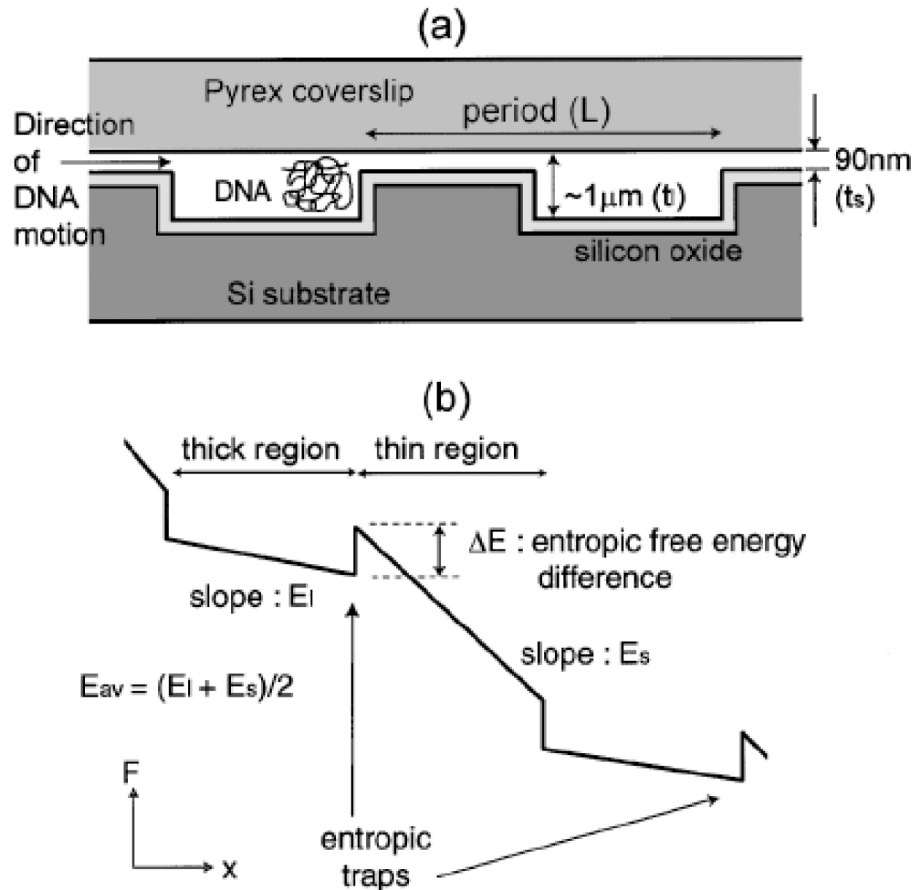


Figure 2.13: A) A cross-sectional schematic of an entropic trap device, reprinted with permission from [58], Copyright 1999 American Physical Society. DNA is “trapped” in deep regions of high entropy and forced against shallow regions. The shallow regions are smaller than the radius of gyration of the molecule, and entry into those regions would require sacrificing configurational entropy. B) The energy landscape of consecutive entropic traps. Molecules require considerable energy to overcome the barriers. The energy is attained when random, “beachhead” events extend a portion of the molecule a critical distance into the shallow region. Once a critical insertion length is obtained, the electrical force is sufficient to overcome the entropic force and the molecule jumps the barrier.

2.7.4 Asymmetric Potentials

In one of the famous Feynman lectures, Richard Feynman discusses a pawl and ratchet device that under certain conditions turns in the expected direction, but in other, quite realizable, conditions the ratchet device can be “made” to turn in the opposite direction [64]. It has been proposed theoretically that asymmetric potentials, with shapes that look like the teeth of a ratchet, could be used to separate biomolecules [65-70]. A number of physical properties of the biomolecules could in principle be used to separate them with asymmetric potentials, though the molecular diffusion constant is the focus of the cited studies. Essentially, the proposed devices act as diffusion rectifiers, allowing net motion in only one direction. Another similarity of these proposals is that the asymmetric potential is established via arrays of asymmetric structures.

Figure 2.14 shows examples from each of the proposals. Molecules are driven through an array of obstacles (electrophoresis is typically used). The obstacles are asymmetric to the flow. That is, as one moves from row to row, moving to the left looks different than moving to the right. The asymmetry can be accomplished by “tilting” the structures relative to the direction the molecules are driven (through the fabrication process), or by bringing the molecule flow into the array slightly skewed. As molecules move from row to row they diffuse laterally (they also diffuse forwards and backwards but this motion is not important for the separation). If they are moving fast enough, then it is highly unlikely that they will move to the left by an entire column (for the structures shown in Figure 2.14B-C). It is not so unlikely that they will move sufficiently far to the right to jump to the next column to the right. The likelihood of jumping to the next column depends upon the ratio of the diffusion

constant to the product of the velocity and the structure width. Note that if the molecules move very slowly, then they will have a significant chance of moving to the left column (and forward and backward diffusion will start to matter). Also, if the molecules move very quickly, then they will never have a chance to diffuse to the next right column. The sweet spot of the molecular velocity for the separation is entirely dependent upon the diffusion constants of the molecules and the dimensions of the device (both the structure dimensions and the spacing between structures). The diffusion array is an excellent example of a separation device that is only possible with carefully designed micro- and nanoscale structures.

In one of the first experimental demonstrations of this phenomenon, Chou *et al.* showed that DNA molecules with different diffusion constants (lengths) had significantly different probabilities of moving from column to column across an array of asymmetric obstacles [71]. 15kb DNA exhibited more lateral displacement than did 33.5kb DNA when they were driven electrophoretically through the array. These researchers encountered problems when loading mixed DNA samples, so they were unable show that their device could be used for separating DNA. Though a true separation of the species was not performed in their experiments, the authors note that the resolution of the displacements is 6% of the molecular length for the lengths studied, suggesting that about fourteen equally size-spaced DNA molecules could be separated using this technique.

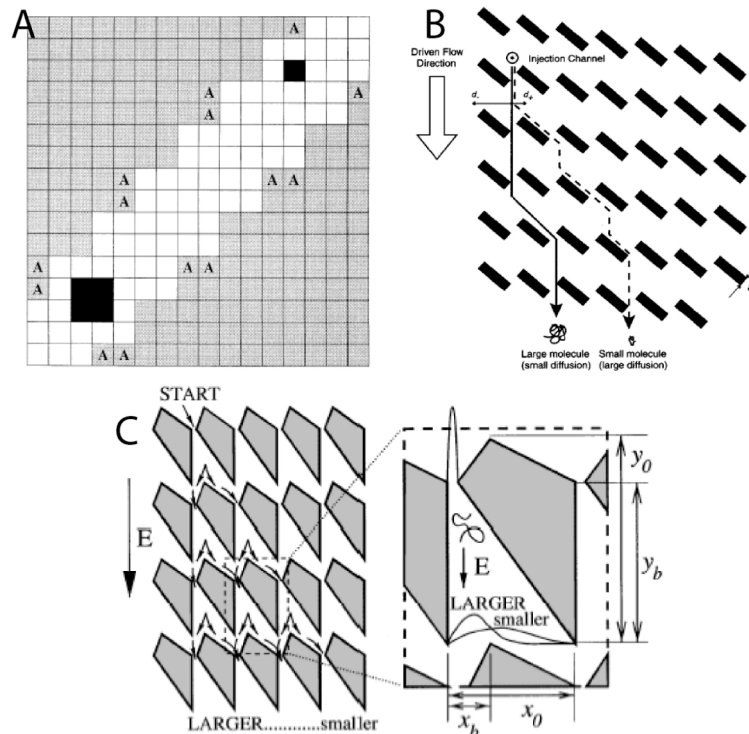


Figure 2.14: A) The channel modeled by Slater *et al.*, reprinted with permission from [67], Copyright 1997 American Physical Society. The shaded squares are the boundaries of the channel and when the squares labeled with 'A' are removed, the channel is asymmetric. In the symmetric channel, Slater *et al.* showed that for 2x2 and 1x1 hard, diffusing objects can be made to move along the diagonal even when the net driving field is zero. Furthermore, when the channel is made asymmetric, there are critical AC field pulses (field strength times time) such that the 2x2 and 1x1 objects move in different directions. B) The asymmetric diffusion array of Cabodi *et al.*, reprinted with permission from [28], Copyright 2002 Wiley-VCH Verlag GmbH & Co KG. Once molecules pass the downstream edge of an obstacle, they must diffuse a distance d^- in order to skip a column to the left, d^+ to skip a column to the right, or continue to move down along the same column. Due to the asymmetric shape of the obstacles, it is nearly impossible that molecules move to the left d^- . Larger molecules have a significantly smaller chance of moving to the right a distance d^+ than do smaller molecules with larger diffusion constants. Thus, smaller molecules tend to skip columns to the right, whereas larger molecules tend to move straight down the array. C) A different array of asymmetric obstacles proposed by Ertas, reprinted with permission from [69], Copyright 1998 American Physical Society.

Shortly after Chou *et al.* published their results, Cabodi *et al.* solved the technical problem of sample loading that prevented the earlier researchers from separating multiple DNA sizes from each other [28]. Their work describes separation of T2 DNA from T7 DNA in essentially the same type of asymmetric array as [71] used. Out-of-plane sample injection permitted a thin stream of molecules to be drawn from the sample reservoir and into the separation array portion of the device. 3.8cm from the injection point (about 2200 rows), the two DNA molecules were observed to be separated by about 440 μ m. Based upon the theoretical model proposed by Austin and Duke [68], the molecules should have been nearly twice as far apart (750 μ m). The authors note that the discrepancy is likely due to the observed deformation of the molecules as they interacted with the obstacles. This would cause the molecules to deform into non-spherical shapes or elongate, either of which would certainly alter the diffusion constant of the molecule. Additionally, the original model supposed conducting obstacles which is not the case in the experiment. The insulating obstacles cause the electric field lines to deform leading to electric field gradients in each unit cell of the array. These gradients could contribute to molecular deformation such as elongation [72].

van Oudenaarden and Boxer used an array of asymmetric obstacles to separate charged molecules in lipid membranes [73]. Lipids are polar molecules that are of biological interest because they constitute cell membranes. Many proteins reside in and interact with lipid bilayers. Scientists often use lipid bilayers to study molecular diffusion. In their lipid membrane experiments, van Oudenaarden and Boxer observed that diffusion was rectified by an array of asymmetric obstacles and net lateral motion was observed even though the driving force (an electric field) was oriented directly

along a column. In addition to supporting the theoretical aspects of the previously discussed DNA separation experiments, the lipid experiments prove that the phenomenon of rectified diffusion is generalizable and useful across a range of biological systems.

It should be pointed out that all of the previously described molecular separation experiments (those described prior to this sub-section) are essentially discrete in nature. That is, biomolecules are loaded into a device and a band of molecules is defined. The band is then separated based upon some interaction with the device or environment within the device. While bands may be loaded and separated in rapid succession, each experiment has a definite beginning and a definite end. The primary reason for this “discreteness” is that all molecules must traverse the same path as they are separated and detected. Note that this is true of conventional molecular separation experiments as well (slab gel electrophoresis, for example). All of the diffusion array devices described in this sub-section can be operated in a continuous mode, however, setting them apart from most other separation schemes. Molecules are introduced to the obstacle array from a reservoir and are separated laterally in space as they move through the array. There is no need to define plugs of molecules as the separated molecules move along entirely different physical paths. In addition to the continuous nature afforded by this scheme, another distinct advantage of laterally separating the molecules is that sample recovery is potentially much easier than in the discrete separation process. If one wanted to do analysis, purification, and sample recovery, then an asymmetric obstacle course would be very useful.

2.8 CONCLUSIONS

We have described one version of the history of microfluidics as it progressed from microchip-based capillary electrophoresis experiments to novel structures capable of elucidating new physics and permitting previously unrealizable methods of separating biomolecules. The story has focused on the myriad of applications made possible through creative uses of standard CMOS fabrication techniques. None of the advances in microfluidics would have been possible were it not for the preceding efforts of the solid state physics and electronics communities.

Our focus has been highly separation-centric, and we have omitted discussing exciting work that is taking place with applications as diverse as microfluidic-based cell and tissue culture [74-76] and micro-chemical reactors [77-81]. There are numerous excellent reviews available covering a wide range of topics within the discipline of biological applications of micro- and nanofluidic devices. Many of the devices discussed herein are further discussed in [1, 7]. A variety of microchip-based capillary electrophoresis-like devices and many applications of these devices are discussed in [82]. In addition to separating biomolecules by size through some kind of charge variability or frictional interaction, microchip capillary electrophoresis affords other possibilities for analyzing biological samples. Many of these are discussed in [83]. From the standpoint of examining the new directions that standard CMOS-type fabrication tools are being employed, our focus on separation techniques tells essentially the same story as if we had considered any of these other applications.

One of the primary future applications of micro- and nanofluidics is to develop μ TASs. This effort will almost certainly involve an even stronger bond

between the CMOS fabrication, optics, electronics, fluidics, and systems integration communities. Packaging and power requirements may prove difficult, though even these issues are currently being addressed [84]. Current engineering efforts include integrating microfluidic chips with micro-optical lenses, lasers, and detectors, all of which can be miniaturized in some way [21, 85-88]. Once substantially all of these components are put on-chip, these μ TASs could be widely deployed for applications such as rapid DNA sequencing and inexpensive medical diagnostics.

CHAPTER 3

DNA AS A POLYMER

3.1 Introduction

In this chapter I describe DNA molecules from the standpoint of the DNA molecule as a polymer. The biochemical structure of DNA is considered, with points relevant for electrophoresis being emphasized. Then, the polymeric qualities of DNA are described, especially the scaling of the size of the molecule with the number of bases. Finally, electrostatic properties of DNA in electrolyte solutions are briefly mentioned.

3.2 Biochemical Structure of DNA

DNA, deoxyribonucleic acid, is generally thought of as a fairly long polymer chain (at least, say, a tens of monomers). The DNA polymer is comprised of four monomer building blocks, the so-called bases. These four bases are attached to each other by identical pieces of “backbone” consisting of a ribose sugar and phosphate group. In this sub-section, we discuss aspects of the biochemistry of the DNA polymer that are relevant for effecting the separations discussed later in this dissertation.

A generic DNA polymer chain is shown in Figure 3.1. A DNA monomer consists of three separate parts: the phosphate group, the ribose sugar, and the base. A ribose sugar lacking an oxygen atom (hence, “deoxyribonucleic”) acts as a bridge between the phosphate group and the base. Along the entire polymer the sugar-phosphate backbone repeats exactly once for every base. The bases vary amongst adenine, cytosine, guanine, and thymine. A single polymer consisting of some pattern of A, G, C, and T bases is a single-

stranded DNA molecule (ssDNA). This pattern of bases is commonly referred to as a sequence.

Single-stranded DNA polymers are physically stabilized by so-called base-pairing interactions. The chemical make-up of the bases is such that A and T, when spatially close enough, are able to gain free energy by forming hydrogen bonds with each other [89]. Similarly, G and C are capable of forming stabilizing hydrogen bonds. Thus, when distant parts of a single strand of DNA or two different strands of DNA are in close proximity with each other, there is a chance that they will bond with each other in those locations where As and Ts can bond and Gs and Cs can bond. For ssDNA, the free energy gain from base pairing is offset by the free energy lost due to the bending that must take place for the strand to pair with itself. Figure 3.2 schematically depicts ssDNA base pairing and dsDNA base pairing. When two strands of dsDNA are exactly complimentary to each other, as is the usually the case with genetic DNA, a stable double helix forms.

From a genetic perspective, the pattern of bases in a DNA polymer is certainly important. It is the specific pattern of bases (often called a sequence) that gives rise to genes that encode proteins during DNA transcription and subsequent RNA translation. Furthermore, there are sequences of DNA that serve as chemical or physical recognition sites for molecules such as DNA polymerases or for segregating chromosomes during cell division (as when central regions of DNA, called centromeres, are bound to the mitotic spindle) [89].

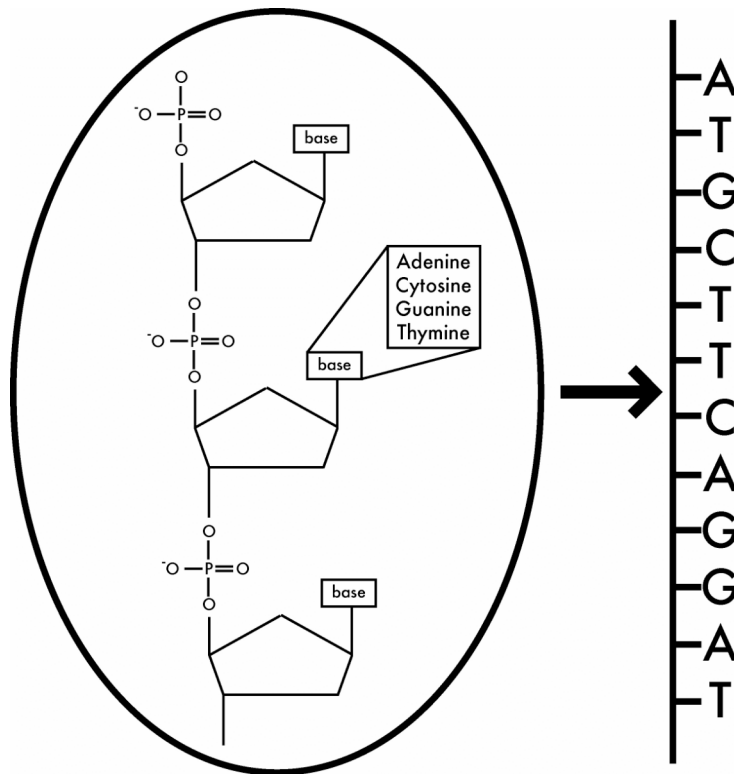


Figure 3.1: A generic DNA polymer chain. Circled on the left is shown the ribose sugar-phosphate backbone. Each base is linked to each unit of backbone. Each unit of the backbone carries one negative charge under physiological pH conditions. There is a slight variation in the masses of the bases, though the masses are typically approximated as being equal. This leads to the comparable scaling of the molecular weight and the charge directly with the total number of bases in the polymer chain. A more familiar view of the DNA polymer is shown at the right, where the sugar-phosphate backbone is “ignored” schematically.

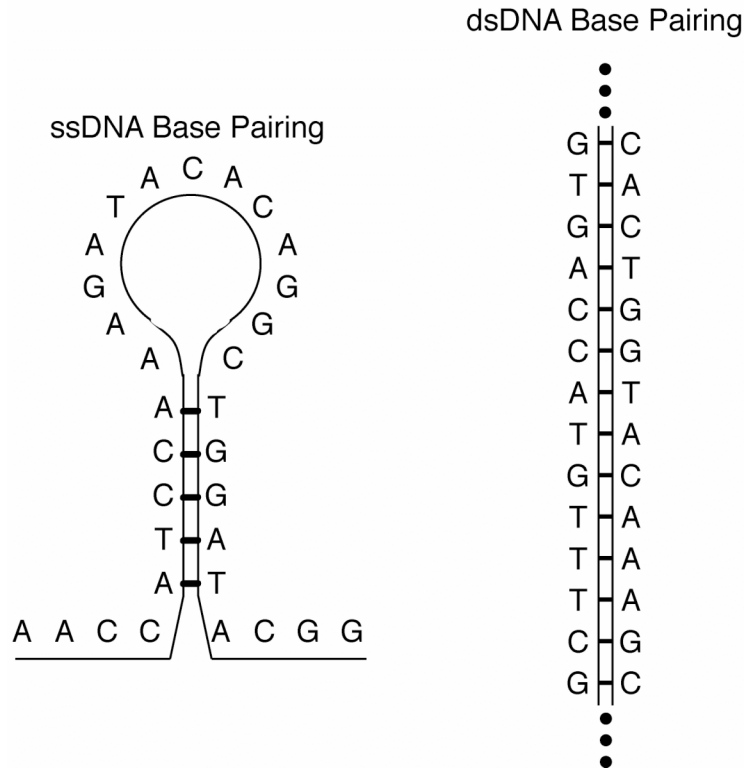


Figure 3.2: DNA base pairing shown schematically for single and double stranded DNA. The bases A and T are complimentary to each other in the sense that stable hydrogen bonding can occur when these bases are near each other. Similarly, G and C are complimentary to each other. As shown on the left, regions of ssDNA can fold on themselves and form intrastrand base pairing when enough distance separates the base pairs so that the flexibility of the strand is not an issue (energetically). On the right, the standard DNA double helix is shown as composed of two strands of exactly complimentary single stranded DNA.

3.3 Statistical Description of DNA

While the sequence of a DNA molecule is important from a genetic perspective, the sequence is not that important when the molecule is treated as a polymer. From the perspective of the DNA molecule as a polymer, there are more relevant ways of describing the molecule than by elucidating its base sequence.

Physically, the monomer length of DNA, a , is about 0.34nm. The width of a dsDNA helix is about 2nm. If the backbone of the DNA polymer was very stiff, then the total length of the molecule would be

$$L = aN, \quad (3.1)$$

where N is the total number of bases (or base pairs for dsDNA). The backbone of DNA is not, however, so stiff that the molecule cannot relax into a three-dimensional, globular state in most physiologically relevant buffers.

Because DNA molecules are flexible, their overall “length” is not given by Equation 3.1. In the most extreme case – from the perspective of polymer physics – one can calculate the three dimensional, relaxed size of infinitely flexible molecules from a random flight (freely jointed chain) model without self-avoidance. The result is that the average end-to-end distance is

$$R_g^2 \propto nl^2, \quad (3.2)$$

where n is the number of joints and l is the length of each joint [90, 91]. For persistent polymers, one generally considers a joint to be a region of bases about 50nm in length for dsDNA and about 3nm in length for ssDNA (this length depends upon the salt concentration, among other things) [16, 92]. This persistence length can be mathematically defined (see, for example [93]), but qualitatively it is the length over which the polymer behaves a semi-rigid rod.

The freely jointed chain model gives a reasonable first estimate of the size of a persistent polymer, but there are better models. If one takes the volume excluded by adjacent and distant monomers into account, then one arrives at a radius of gyration of

$$R_g \approx R_0 \left(\frac{N^{1/2} v_c}{l^3} \right)^{1/5} \propto N^{3/5}, \quad (3.3)$$

where R_0 is the random flight radius of gyration (Equation 3.2), and v_c is the excluded volume parameter [46, 90, 94, 95]. Equation 3.3 is further discussed

in chapter 7, where we look at an approximation of the excluded volume. Note that the excluded volume causes the molecule to swell in size.

Double-stranded DNA that is two thousand base pairs in length has a radius of gyration of about 100nm. Equation 3.3 is the most relevant means of describing the size of DNA molecules within the context of the separations discussed in chapters 6-8. Many of the nanoscale approaches to separating DNA rely upon the radius of gyration of the molecule being on a comparable size scale as the device features.

3.4 General Considerations When Dealing With DNA

There are a few general considerations that should be noted when performing separation experiments with DNA in microfluidic environments. These considerations are not entirely obvious from either the biochemical or physical perspectives previously considered, so they are explicitly pointed out below.

3.4.1 Debye Screening

Because the sugar-phosphate backbone of the DNA molecule is negatively charged, there is an element of stiffness caused by electrical repulsion of adjacent bases. This electrostatic repulsion is dependent upon the effective charge on each phosphate group. The effective charge in turn depends upon the concentration of ions in the buffer solution. The more ions there are in the buffer solution (or the greater their valence) the more effective the buffer is at neutralizing the charge along the backbone of the molecule.

Debye screening is the general term given to the effect of counterions effectively neutralizing the electric field between two charged particles in

solution (bases being the charged particles of interest for this discussion). Normally, one would write down a standard Coulomb interaction for adjacent bases. However, counterions in solution effectively mitigate the electric field between these adjacent bases, reducing their repulsion from each other.

To quantify the effect of the buffer ion concentration on the screening of charge along the DNA backbone, one commonly introduces the Debye screening length. The Debye screening length gets its name from the basic theory of counterion condensation introduced by Debye and Huckel almost 100 years ago [96, 97]. One begins by writing down the Poisson equation in spherically symmetric coordinates

$$\nabla^2\psi(r) = \frac{1}{r^2} \frac{d}{dr} \left(r^2 \frac{d\psi(r)}{dr} \right) = -\frac{\rho(r)}{\epsilon\epsilon_0}, \quad (3.5)$$

where r is the radial coordinate, ψ is the potential, and ρ is the charge distribution. One takes the ion concentration of the solution to be given by

$$c_i(r) = c_{i0} \exp(-z_i e \psi(r) / kT), \quad (3.6)$$

where c_{i0} is the bulk ion concentration, z_i is the charge of the i -th ion, and e is the fundamental charge. Note that Equation 3.6 is a Boltzmann distribution of charge where we have taken the energy as the electrostatic energy equal to $z_i e \psi(r)$. From Equation 3.6, one writes down the charge distribution as

$$\rho(r) = F \sum_i z_i c_i = F \sum_i z_i c_{i0} \exp(-z_i e \psi(r) / kT), \quad (3.7)$$

where F is Faraday's constant. If one now puts Equation 3.7 into Equation 3.5, one finds a beast of a non-linear, inhomogeneous differential equation. While this can be solved analytically (given a few assumptions about the valence of the ions), the exact solution is not required to obtain the so-called Debye length, the quantity with which we are interested. Debye and Huckel approximated the exponential term of Equation 3.7 as the first two terms of the Taylor series expansion to obtain

$$\nabla^2\psi(r) = -\frac{F}{\epsilon\epsilon_0} \sum_i z_i c_{i0} \left(1 - \frac{z_i e \psi(r)}{kT}\right) = \kappa^2 \psi(r), \quad (3.8)$$

where we have introduced $\kappa^2 = \frac{Fe}{\epsilon\epsilon_0 kT} \sum_i c_{i0} z_i^2$, and explicitly evaluated the sum $\sum_i z_i c_{i0} = 0$, which is the case for an electrically neutral bulk solution. Note that the Taylor expansion of the exponential amounts to the statement that the counterions do not come too close to the ions. That is, that the solvent is dilute. While this is almost never the case practically, the exact solution of Equation 3.5 leads to the same important result for the length over which electrical screening occurs [96]. Most importantly, I should point out that κ has units of reciprocal length, and κ^{-1} is usually referred to as the Debye length. This length gives a rough estimate of the size of the counterion cloud that an ion draws near it in solution. Note that the Debye-Huckel approximation is only valid for the case of dilute counterion concentrations. Finally, I point out that for most buffers used in microfluidic experiments, the Debye length is <1nm at room temperature. That is, charges are effectively screened beyond 1nm so that no electrical repulsion between ions is felt beyond this distance.

It should be pointed out that the Debye screening length is an important parameter to consider when thinking about electrophoresis through nanochannels as well [23, 24, 26, 96, 98]. Glass channels are typically ionized at the surface, so that there is a fixed negative charge on the walls. This charge is similar to the fixed charge along the backbone of DNA, and draws counterions in solution. These counterions form a diffuse layer of positive charge near the wall. For relatively low ionic concentrations of buffer, the Debye length at the channel wall is greater than 1nm, and this large Debye layer causes a phenomenon known as electroosmosis. In the experiments described herein, electroosmosis is essentially eliminated by using relatively high ionic concentrations (5x TBE buffer which has a molarity of 445mM), in

conjunction with the low molecular weight polymer, polyvinylpyrrolidone, which screens the fixed surface charge on the channel walls [8, 99].

Because the Debye screening length is so small, the interior of the molecule is essentially “exposed” to the liquid environment. That is, charge condensation does not occur solely on the exterior surface of the blob of DNA, but everywhere along the polymer chain. This is the origin of the free-draining property of DNA, which in turn leads to the direct linear scaling of the liquid friction of the molecule with the total number of bases of the molecule.

3.4.2 Confinement-induced Conformation Changes

When DNA is found in large volumes of liquid it is able to relax into its three-dimensional blob state as described by Equation 3.3. In many micro- or nanofluidic experiments, however, DNA molecules are forced into confining environments. Confining environments are those areas in which at least one dimension of the volume is smaller than the radius of gyration of the relaxed DNA blob. Examples of confining environments include nanopores through which DNA must linearly elongate [100, 101], nanochannels in which DNA molecules elongate in a cylinder-like configuration [45, 46, 102-104], and nanoslits through which DNA either rapidly hop or in which DNA fills a pancake-like, two-dimensional volume [25, 57, 58, 62, 63, 105](and see chapter 8). Given an external force, DNA molecules can be forced into confining environments, but they must squish to do so. Bouchard has considered the free energy available to DNA molecules to describe the polymer volumes (or areas) when forced into these spaces [106].

The confining geometry that is relevant for my work is a quasi-two-dimensional, or slit-like, geometry. Given a three dimensional scaling as in

Equation 3.3, DNA deforms into a pancake-like structure composed of sub-blobs of monomers. Each sub-blob composing the pancake is treated as a relaxed blob with a diameter equal to the slit height (so that the volume is $\sim h^3$, where h is the slit height). Each sub-blob is composed of a number of bases

$$g_h = \left(\frac{h}{a}\right)^{5/3}, \quad (3.9)$$

where a is the monomer size. The radius of the pancake structure composed of these sub-blobs of DNA is

$$R_{2D} = \left(\frac{N}{g_h}\right)^{3/4} \times h \sim N^{3/4} h^{-1/4}. \quad (3.10)$$

Equation 3.10 highlights that the scaling of the size of the DNA structure is different when the DNA is confined in a quasi-two-dimensional environment than when it is in a three-dimensional volume in which it can relax. I will turn our attention back to this pancake structure in chapter 7.

3.5 Conclusions

In this chapter, I have described many of the physical and chemical properties DNA polymers that are important for the applications described later in the dissertation. DNA molecules have weight and charge that scale (essentially) linearly with the number of bases in the polymer. A polymer can be described by a three-dimensional relaxed volume based upon its persistence length, or stiffness. The ionic strength of the buffer affects the persistence length of the molecule as counterions in the buffer are able to effectively neutralize the electrostatic repulsion between adjacent regions of negatively charged backbone. Finally, I considered how confining geometries affect the volume occupied by DNA molecules. All of these concepts will come into play as I describe nanofluidic devices used to separate DNA molecules by length throughout the rest of this dissertation.

CHAPTER 4

THEORY OF ELECTROPHORESIS

4.1 Introduction

In this chapter I lay down the theoretical framework of DNA electrophoresis. A significant amount of the experiments presented later in this dissertation are variations on the basic idea of DNA electrophoresis in free solution. Even the more intricate separation techniques in nanofluidic channels build their theoretical models upon the foundation of standard DNA electrophoresis. Therefore, this chapter is devoted to starting at the beginning of DNA electrophoresis and moving toward the more complicated theories used to describe various micro- and nanofluidic experiments.

4.2 Free Solution Electrophoresis

As is often the case when trying to understand a physical process, a good place to start is with Newton's second law. To construct a simple model for free solution electrophoresis, I initially assume that there is a charged, spherical particle in a macrofluidic channel. I apply an electric field through the channel and write down the equation of motion for the particle.

The electric force, F_E , drives the molecule through the channel,

$$F_E = QE, \tag{4.1}$$

where Q is the total charge of the particle and E is the magnitude of the electric field (V/cm; note that I assume that the electric field is directed exactly along the axis of the channel so that the direction of the field and the ultimate motion are collinear. Consequently I will ignore the vector-nature of the electric

field, velocity, and so on). There is also a drag force on the particle resulting from the interaction of the particle with the fluid,

$$F_d = Dv, \quad (4.2)$$

where D is the drag coefficient of the particle and v is the particle velocity. These are the only two forces acting upon the particle, so the equation of motion is

$$m\dot{v} = QE - Dv. \quad (4.3)$$

For biological molecules smaller than cells, inertia forces are typically negligible. I point out that terminal velocity is reached nearly instantaneously, so the acceleration is effectively 0. Equation (4.3) becomes

$$QE = Dv \rightarrow \frac{v}{E} = \frac{Q}{D}. \quad (4.4)$$

The term v/E occurs so frequently in electrophoresis that it is given the name “mobility”, $\mu \equiv v/E$. Upon inserting the mobility into Equation (4.4), one arrives at the “equation of motion” for a charged particle moving under the influence of an electric field in a fluidic environment

$$\mu = \frac{Q}{D}. \quad (4.5)$$

4.3 “Pathologic” Scaling

As pointed out in the previous chapter, both the mass and the charge of DNA molecules scale directly with the length of the molecules. The Canadian physicist Gary Slater has described this unfortunate coincidence as “pathologic” for the reason that it makes separating DNA by length somewhat difficult (from an engineering perspective) [107]. In this section, I will look at the charge scaling and the relationship between base pairs, mass, and drag for DNA molecules.

For DNA molecules, the electric charge scales directly as the number of base pairs. The reader can refer to Figure 3.1 to see that there is one unpaired electron for each monomer unit of the DNA polymer. This is true across most of the pH range and all of the physiologically relevant pH range. As discussed in Section 3.4.1, counterions in the buffer can screen the charge along the backbone of the DNA molecule. This screening process is, however, statistical in nature, so on average all charges on all molecules are screened equally. Therefore, at the end of the day, one can write down the total effective charge of a DNA molecule as

$$Q = qN \propto N, \quad (4.6)$$

where q is the charge per base pair (or base), and N is the total number of base pairs (or bases). Note that Equation 4.6 assumes an average q and that implicit in q is a prior calculation of the degree of counterion screening.

If the DNA molecule is treated as an impermeable, spherical particle, then one can estimate the drag by relating the size of the sphere to the size of the molecule. The relationship between the size of the sphere of DNA and the length of the DNA molecule was shown in Section 3.3 in Equation 3.3. Using Stokes' theory of fluid dynamics, the drag for a spherical particle is

$$D = 6\pi\eta R \propto N^{3/5}, \quad (4.7)$$

where R is the radius of the sphere, and η is the fluid viscosity [108].

Substituting Equations (4.6) and (4.7) into Equation (4.5) yields $\mu \propto N^{2/5}$. This relationship actually looks pretty good as it suggests that length dependent separation is possible in free solution.

Unfortunately, however, Equation (4.7) is not correct for DNA in solution. The reason is because DNA does not relax into an impermeable sphere. As described in chapter 3.4.1, the Debye screening length for most buffer

conditions is quite small (~ 1 nm). Thus, counterions not already screening the DNA backbone can get quite close to the molecule before they are repulsed by electrostatic interaction with the counterions already screening the backbone. Thermal effects and diffusion then make it quite possible for the nearby counterions to swap places with the screening counterions. Furthermore, one should not disregard the attraction the counterions feel for the electric field, which is in the opposite direction as the motion of the DNA molecule. When this dance of counterions is considered along with the low density of monomers in the interior of the relaxed blob of DNA, one realizes that DNA is free-draining to counterions. That is, rather than dragging counterions along with it as it moves, DNA molecules continually wash away currently screening counterions with new counterions.

The net result of the free-draining property of DNA is that the Stokes model for the drag on an impermeable sphere is not applicable to DNA in buffer solution. The drag scales directly as the length of the molecule because every monomer is able to interact with the fluid. Thus, the drag on the molecule is actually given by

$$D = \delta N \propto N, \quad (4.8)$$

where δ is the drag per base pair (or base).

The pathology of the scaling is now more apparent. Upon substitution of Equations (4.6) and (4.8) into Equation (4.5) the mobility is seen to be independent of the length of the DNA molecule. Essentially the remainder of this dissertation is devoted to addressing this problem. And recall that this is a problem because there are many things that can be learned about biology, disease, and evolution if one can separate DNA molecules by length.

4.4 Drag Tags & Charge Thrusters

While not proposed theoretically or attempted experimentally until recently [19, 107, 109, 110], one can break the charge-mass scaling symmetry by adding a particle to all DNA molecules that one wants to separate. If the particle added is electrically neutral, then the particle acts as a drag on the DNA molecule. If the particle is negatively charged, then it acts as an electromotive thruster for the DNA molecule.

The added particle adds some drag which is equivalent to the drag of some number of base pairs. Thus, adding the particle to the DNA is equivalent to adding the drag of that many base pairs to the DNA molecule. Similarly, the added particle has some charge which is equivalent to the charge that would be added if some number of base pairs were added to the DNA molecule. It is common to call the added drag α and the added charge β . For small or streamlined particles, $\alpha = 0$. For neutral particles, $\beta = 0$.

The total charge of the DNA molecule is now $Q + \beta$ while the total drag of the DNA molecule is $D + \alpha$. Upon substitution into Equation (4.5), we have

$$\mu = \frac{Q + \beta}{D + \alpha} = \mu_0 \frac{1 + \beta/Q}{1 + \alpha/D}, \quad (4.9)$$

where I have made the common substitution of $\mu_0 = Q/D$, which is often referred to as the free-solution mobility. Equation (4.9) highlights that by adding charge or drag to the DNA molecule, the DNA mobility changes by the amount of fractional change in the charge or drag. If one adds a charge thruster (increases β), then smaller molecules migrate faster than longer molecules. If one adds a drag tag (increases α), then larger molecules are slowed less than smaller molecules. This theoretical framework was proposed

a decade ago and then refined in the following years. Experiments involving so-called drag tags were performed using proteins [111, 112].

Adding drag tags or charge thrusters are a means by which to separate DNA molecules by size without resorting to changing the DNA's environment (such as by adding a gel). However, one must change the DNA molecule by doing chemistry before trying to separate them. While the chemistry is no more difficult, in many cases, than that already required to fluorescently label the molecules, it is an extra step that one would prefer not to have to do. In order to avoid having to add drag tags or charge thrusters to DNA molecules, one generally forces the DNA molecules move through an environment that breaks the charge-to-mass scaling symmetry. A gel is one such typical environment and we turn our attention there next.

4.5 Gel Electrophoresis

Gel electrophoresis of DNA is perhaps the most commonly employed technique for separating molecules by size. Gels are easy to manufacture, and the process of “running” a gel is straightforward. Gels typically consist of polymers like agarose or polyacrylamide, formed in such a way as to irreversibly entangle the fibers. The consistency and appearance of a gel is very similar to that of clear or slightly opaque (white) Jell-O®. Gel electrophoresis is primarily analytical, though sample recovery methods do exist. Here, I will discuss the phenomenological theory that explains how DNA migrates through gels.

In the 60s, Ferguson developed an empirical model that accurately matched electrophoresis data obtained at that time [92, 113]. Electrophoresis was focused on separating small polyelectrolytes, such as proteins. The

mobility of these polyelectrolytes was found to be exponential with respect to what was thought of as a geometric parameter

$$\mu = \mu_0 \exp(-Kc), \quad (4.10)$$

where c is the gel concentration (usually measured in the weight-to-weight ratio of powdered gel to water), and K is known as the retardation coefficient. K essentially measures the volume excluded by the gel fibers. Readers familiar with gel electrophoresis will recognize that a logarithmic plot of the mobility produces a negatively sloping line. This type of plot is commonly referred to as a Ferguson plot and is primarily used to judge when molecules are moving in the “linear” regime, in which fairly accurate size estimates can be made when unknown samples are run adjacent to a “ladder” of molecules of known sizes.

The empirical model of Ferguson had been formalized by Ogston in the 50s, then generalized by numerous others in the 70s [114-119]. The formal model takes as an essentially axiomatic assumption that

$$\mu = \mu_0 f, \quad (4.11)$$

where f is the free, fractional volume through which molecules can move in a gel. Again, this model is geometric in nature. All of the “hard part” of the model lies in estimating f for various gel geometries. As described by Viovy, various models exist for f [92]. If the obstacles are planar in nature and the molecule has one large dimension, then

$$f = \exp(-sL), \quad (4.12a)$$

where s is the surface area per unit volume of the obstacles, and L is the large dimension of the molecule. If the obstacles look like long, impenetrable fibers, then

$$f = \exp(-hA), \quad (4.12b)$$

where h is the length per unit volume of the fibers, and A is the surface area of the molecule. Finally, if the particle is suspended in a volume of point-like obstacles with a number density n , then

$$f = \exp(-nV), \quad (4.12c)$$

where V is the volume of the molecule. Note that substitution of any of Equations 4.12a-c into Equation 4.11 leads to Equation 4.10. Equations 4.12a-c are estimates of the product Kc , the geometric factor in Ferguson's original model. It should be pointed out that if the molecule is essentially spherical in nature, then L , A , and V can be estimated given the radius of the molecule and the small dimension of the obstacle.

Rather than belaboring this theory, I want to end by noting that Equations 4.10-4.12 “start” not with an equation of motion, but with some data that needs to be fit. A researcher uses one of Equations 4.10-4.12 to fit the mobility of separated molecules and compares those data to a standard. There is nothing wrong with this approach (I'm speaking as an engineer and experimentalist now), but one of the great virtues of micro- and nanofabricated structures is that one can start with equations of motion for molecules that are forced to move through the structures. Because we have intimate control over what the structures look like, and because the structures can be made very simple, we can draw things like force diagrams or free energy landscapes and have some assurance that the models reflect both the molecule and the environment. This is an often overlooked perk of nanotechnology, and it is a point to which we will return our attention in chapters 7 and 8.

CHAPTER 5

MICROCHANNEL FABRICATION & EXPERIMENTAL SETUP

5.1 Introduction

More or less all of my graduate student research has been dedicated to engineering micro- and nanoscale devices for separating DNA by length. Many of the practical reasons for manufacturing small devices for DNA separations were described in chapter 2. In this chapter, I give an overview of the micro- and nano-fabrication techniques used to manufacture the devices that I talk about in subsequent chapters. The devices used for experiments all have a number of features in common, and each specific device is only a slight variation on a “standard” microfluidic design. I will describe that standard design in this chapter, and the basic means of manufacturing wafers with that standard design. I also discuss the basic microfluidic experimental setup in this chapter. Details regarding devices and the experimental setup will be described in the following chapters as necessary.

5.2 Generic Microchannel Fabrication

The generic device described in the fabrication steps below is what is commonly referred to as a T-junction (or offset T-junction) injection channel. These devices can be used to separate proteins by length (based upon the unbalanced scaling of a protein’s charge-to-mass ratio) or can be filled with a sieving matrix to separate DNA molecules or denatured proteins by length. The variations taken in my research (and described in chapters 6, 7, and 8) primarily involve “filling” the separation channel with an artificial sieving matrix, making the separation channel very thin (a nanoslit), or filling the separation

channel with a periodic array of nanoslits (an entropic trap array). An understanding of this generic device is necessary in order to understand the variations presented in the following chapters.

The fabrication procedure described below is not “symmetric” in its capabilities with regards to features defined in the planar dimensions versus the vertical dimension. That is, planar-oriented features are defined with an entirely different set of tools than are vertical features. Namely, planar-oriented features are limited in their dimensions and resolution by lithography. This means that sub-500nm features require electron beam lithography (expensive), and sub-2 μ m features require stepper lithography (somewhat less expensive). Larger planar-oriented features can be made with contact lithography (relatively inexpensive) and have very high tolerance for environmental changes (such as temperature, humidity, how much “crud” is in the bottle of photoresist, et cetera). Planar-oriented features are always the channel widths for the devices described in this dissertation.

In the vertical direction, the etching tool and the bonding process set the limits on the feature sizes. In this dissertation, the vertical direction is always the channel depth. Using fused silica affinity bonding, very high aspect ratios can be achieved [45, 46]. The practical limit is then: how little time can one run an etcher? As will be described in chapters 7 and 8, nanoslits have been fabricated and tested with channel depths as thin as 15nm.

As has been the standard practice in the Craighead research group for a number of years now, microchannels are fabricated in fused silica substrates. The process is described for one wafer, though most frequently between two and six wafers are shuttled through the entire process simultaneously (taking advantage of the manufacturing scaling and parallelism

that most of the tools in the cleanroom afford). A general overview of the process is described, with specific etch depths and channel widths given in close proximity to the descriptions of the specific experiments.

The wafer manipulated through the fabrication process and in which the microchannels reside is a 500 μm thick, 100mm diameter piece of fused silica (sometimes hereafter referred to as glass when ambiguity with other types of glass or SiO_2 is unlikely). Figure 5.1 shows a schematic of the two-level fabrication process described in detail below. Note that most microfluidic devices are not two-level, but one-level devices. The schematic accommodates a one-level device by omitting steps 5-8; that is, proceed directly to step 9 from step 4, bypassing steps 5-8.

Photoresist is spin-coated onto the wafer. Typically, Shipley 18-series resists are used, such as Shipley 1805, 1807, 1813, or 1823. Photolithography is used to define microchannels in photoresist. As almost none of the devices described in this dissertation have (planar) dimensions smaller than 5 μm , a contact or proximity exposure tool offers sufficient resolution to expose the photoresist through a chrome photomask. Exposure times are typically between 0.5s and 10s, but vary with the photoresist thickness and environmental conditions. The photoresist is developed using MIF300 developer for 60s or a Hamatech-Steag automated wafer developer that uses MIF300 developed in a pre-programmed, optimized recipe determined by Cornell NanoScale Science & Technology Facility (CNF) staff.

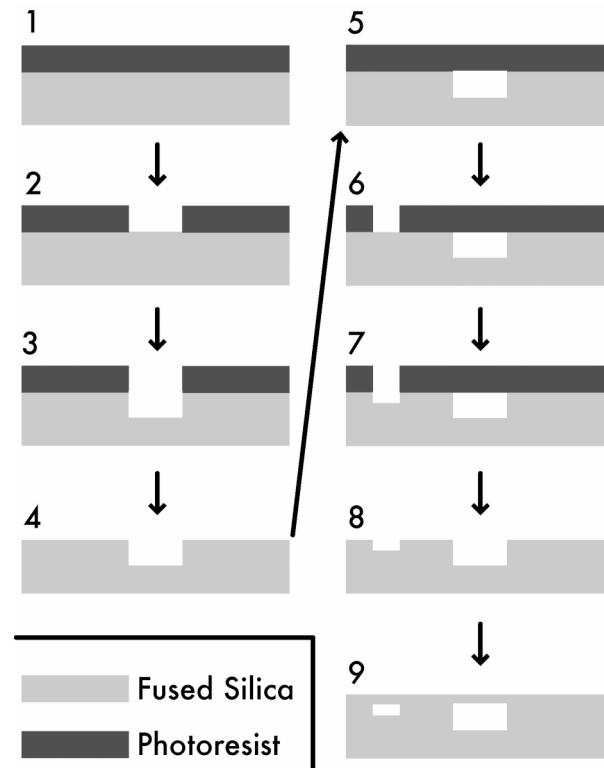


Figure 5.1: A schematic overview of a two-level fabrication process. Photoresist is spun onto a glass substrate. The resist is patterned and developed. Reactive ion etching is used to transfer the pattern into the substrate. The resist is removed and the wafer is cleaned prior to repeating the process with a different photomask (steps 5-8). After a final cleaning, the patterned substrate wafer is bonded to a cover wafer to encapsulate the fluidic channels.

The photoresist pattern is transferred into the glass wafer through reactive ion etching. Etch depths between 15nm and about 1 μ m are possible and reproducible with currently available tools in the CNF. Devices described in this dissertation were etched using either the PlasmaTherm 72 (PT72) or Oxford 80 reactive ion etchers. Both CF₄ and CHF₃+O₂ process effectively etch glass substrates, though all of the devices described herein were etched using CHF₃+O₂ processes (50sccm and 2sccm, respectively). Most of the devices I manufactured were made using the PT72 at a chamber pressure of

40mTorr and a power density of $0.34\text{W}/\text{cm}^2$. These conditions result in etch rates of about 20nm/min (again, this is highly variable and should always be tested and monitored throughout the fabrication process).

After the substrate wafer is etched, the photoresist is cleaned off. This is effectively the end of the first level of the device. Cleaning is accomplished using any or all of the following, perhaps iteratively if the photoresist is resistant to removal: an acetone and isopropanol bath, the CNF resist strip hot bath, an automated Hamatech-Steag wafer spinner implementing a “piranha” process, or oxygen plasma etching in the CNF’s Branson/IPC P2000 barrel etcher or Glen 1000p Plasma Cleaning System.

Once the wafer is cleaned, the above process is repeated for multilayer lithography processes (starting at: spin coat the wafer with photoresist). Multilayer lithography processes are required whenever multiple etch depths are required, and most of the devices I use for DNA separation experiments require multiple etch depths. After the last iteration of lithography-etching-cleaning is performed, the wafer is prepared for sand blasting of access holes by spin coating a thick protective polymer film on the etched surface. We have found that Shipley series 10 photoresists work well as a protective film (these spin to $>10\mu\text{m}$ thickness in many cases). After sand blasting holes to provide access to the sealed microchannels, the wafer is cleaned one last time. This last cleaning is typically frustrating, as sand from the blasting step is difficult to fully remove from the wafer surface. Often, many iterations of the cleaning steps described above are necessary.

After the final cleaning, the etched wafer is ready to be bonded to a $170\mu\text{m}$ thick fused silica cover wafer. $170\mu\text{m}$ thick wafers are used because this is a standard microscope slide thickness and many microscope objectives

are engineered to accommodate looking through this thickness of glass to see the specimen on the other side. If well cleaned, the two wafers bond immediately upon applying a small contact force between them. Often some effort is required to fully “squeeze” out air bubbles that get trapped during the initial bonding process. This is a delicate process, as enough force is required to bend the glass, though one must be careful not to break the glass. To make the bond between cover wafer and device wafer permanent, the wafer stack is placed in a furnace and annealed. For the fused silica wafers that the Craighead group has used for the past few years, a temperature ramp of 100-200°C/hour from room temperature to an annealing temperature of 1050°C works well. The annealing temperature is held for at least two hours and the result is essentially a solid piece of glass embedded with microfluidic channels. Aspect ratios of >1000:1 (width:depth) have been made using this affinity bonding of glass to glass, which is generally better than can be achieved with anodic bonding of glass and oxidized silicon.

The sandblasted holes act as interfaces between the macro- and microworlds. Fluid reservoirs (pipet tips) are glued around the holes, offering 100-200µl capacity. It is through these reservoirs that new fluids or samples are introduced to the microfluidic channels. Parafilm is used to cover the reservoirs, and if placed on the reservoirs with an appropriately firm yet gentle touch, can create a nearly airtight environment (meaning that the devices can be stored for days or weeks without needing to be refilled).

A completed, generic, microfluidic device schematic is shown in Figure 2.4. I will always refer to the channel connecting reservoirs 1 and 2, and the channel from reservoir 3 to the intersection as the loading channels. In a two-level device, these loading channels are always at the deeper etch-depth and

never contain a sieving matrix. The channel from the intersection to reservoir 4 is the separation channel. The separation channel is always filled with a sieving matrix (chapter 6), is thinner than the loading channels (chapter 7), or contains entropic barriers (chapter 8). Sometimes I will describe the separation channel as being offset from the intersection. When the separation channel is offset from the intersection, it means that the loading channel actually continues partially along the direction of the channel towards reservoir 4 before the separation matrix or thin slit begins. Typically the offset is 50-250 μm . The offset is critical in many experiments that involve sample concentration as will be described in detail in chapter 6.

Note that a standard T-junction device is one in which the four channels intersect at the same point (like a typical street intersection). An offset T-junction is one in which the channels from reservoirs 1 and 2 are slightly offset from each other where they intersect the channel connecting reservoirs 3 and 4 (like the street intersection at the corner of N. Aurora and E. Lincoln near the Fall Creek Cinemas in Ithaca). Offset T-junctions offer a geometric means by which to define sample plugs, so they are sometimes more useful than standard T-junction intersections.

5.3 Generic Microfluidic Experimental Setup

All of the experiments I performed to evaluate the microfluidic separation devices were conducted using essentially the same apparatus. This setup is described in detail here and modifications, where they are made, will be described for each specific experiment. A schematic diagram of the experimental setup is shown in Figure 5.2.

An inverted microscope (Olympus IX-70) is used to image microfluidic channels. The wafers containing the channels are mounted on the microscope stage. Gold, silver, or platinum electrodes are used to conduct electricity through the fluidic channels from a power supply. This establishes an electric field which is used to drive DNA molecules by electrophoresis. Voltages used in experiments vary between about 1V and 10,000V (~1-2000V/cm electric field) depending upon the specific application and desired effect.

DNA molecules are made “visible” by staining or dyeing them with fluorophores. These fluorophores absorb incident photons and reemit those photons at a lower energy. AlexaFluor 488 is a commonly used fluorophore and is covalently attached to the end of DNA molecules (single- or double-stranded). Only one such “end-label” fluorophore can be attached to a molecule. SYBR Gold and YOYO-1, on the other hand, are fluorophores that bind along the entire length of the DNA molecule. In the case of YOYO-1, it is an intercalating dye which means that it inserts itself between adjacent bases. The intensity of a molecule stained with SYBR Gold or YOYO-1 is proportional to the length of the molecule, and DNA molecules stained with either of the dyes are typically much brighter than those stained with end-labels like AlexaFluor 488. A mercury arc lamp is used to illuminate the microfluidic channels and to excite the fluorophores attached to DNA molecules. Band pass filters are used to remove the unwanted wavelengths of light from the excitation source. This is necessary to reduce background light intensity. An excitation filter selects the wavelength required to excite the fluorophore. An emission filter then selects the wavelength at which the fluorophore reemits.

All of the raw data presented in this dissertation are intensity data. The light emitted from the fluorophores is collected and quantified by a detector

such as a Cascade 512B CCD camera. Typically, intensity data is taken over time (that is, a channel is observed with the camera for some time) and intensity versus time graphs are produced. From these raw data, derived quantities such as the mobility or concentration of molecules can be calculated. Custom MATLAB routines are written and used to analyze the intensity versus time data.

Perhaps the most important choice one makes when performing a microfluidic experiment is what objective one uses to observe the channels. Luckily, owing to having a rich history of microfluidic experiments performed within the group, the Craighead research group has a collection of very good objectives from which to choose. Three commonly used objectives for the experiments I describe in this dissertation are a: 40x, 1.15 numerical aperture (NA), water-immersion; 60x, 1.2NA, water-immersion; and 100x, 1.35NA, oil-immersion. Usually there is an environmental factor that necessitates the decision to chose one objective over the others, and in all of my experiments that environmental factor was the required field-of-view. That is, I tended to use the highest magnification objective that would permit me to see everything that I wanted to see.

5.4 Conclusions

In this chapter, I have described a generic microfluidic fabrication process as well as a generic experimental setup. In the next few chapters, I will discuss the experiments that were performed to evaluate the DNA separation capability of several micro- and nanofluidic device designs. Details about fabrication will be given tersely, and the reader is asked to refer back to this chapter if the overall picture slips their mind.

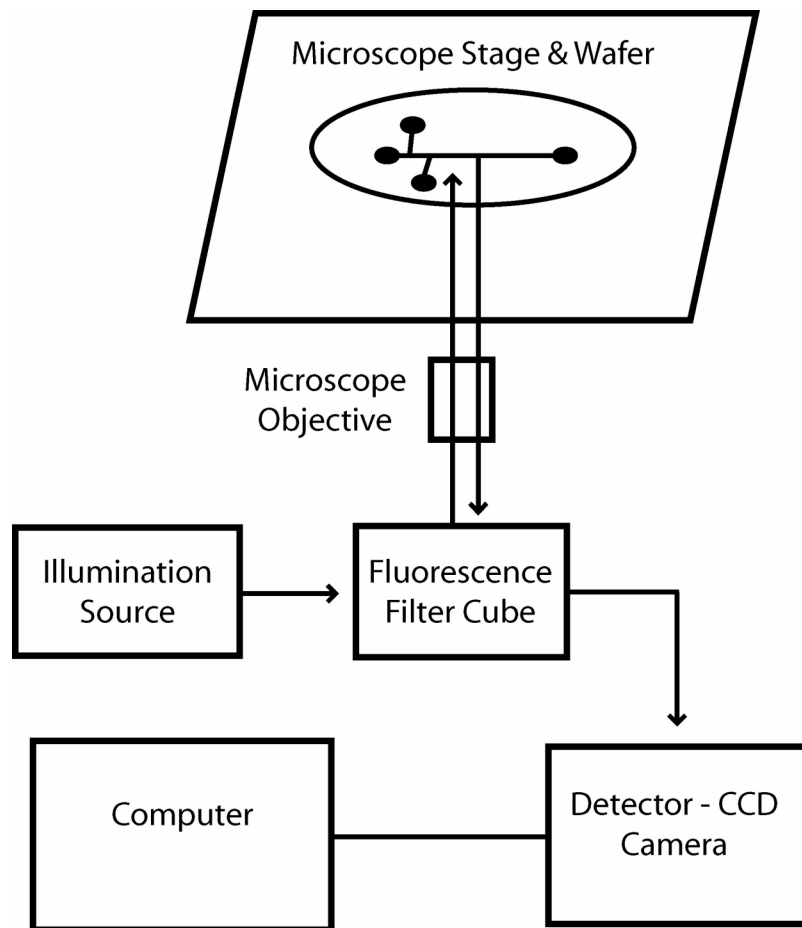


Figure 5.2: A schematic representation of a generic microfluidic experimental setup. The illumination source is either a mercury gas arc lamp or laser. Fluorescence filters are used to selectively pass and cut certain wavelengths of light. Data is collected from the area localized by the microscope objective. Emitted light is detected by a photomultiplier tube or a CCD camera. Real-time and post-experiment processing is performed using a computer, typically with experiment-specific MATLAB routines.

CHAPTER 6

NANOPILLAR DEVICES

6.1 Introduction

In this chapter, I describe the fabrication of a high-surface area, nanopillar-like structure that was made in a microchannel and used to separate DNA molecules by length. The artificial sieving matrix was used to separate DNA molecules between 2kb and 50kb by length in relatively short periods of time (less than ten minutes). The artificial sieving matrix is relatively easy to fabricate and incorporate into a microfluidic channel. Furthermore, the size and spacing of the pillars is comparable to the inter-fiber spacing observed in high concentration polyacrylamide sequencing gels: 10-20nm diameter pillars spaced by 5-20nm channels through which DNA molecules move [120, 121]. Results are described for DNA separations, and the chapter concludes with a discussion of other applications for which the artificial sieving matrix may be well suited.

6.2 Fabricating Nanopillar Structures

Most of the fabrication process for making nanopillar structures in microfluidic channels is identical to the process described in chapter 5 and shown in Figure 5.1. To make the pillars, a gold evaporation step is included in the process between steps 2 and 3 (or alternatively, between 6 and 7). The evaporated gold is used in conjunction with the developed photoresist to act as an etch mask for pattern transfer into the glass substrate. A schematic of just the gold evaporation and etch process is shown below in Figure 6.1.

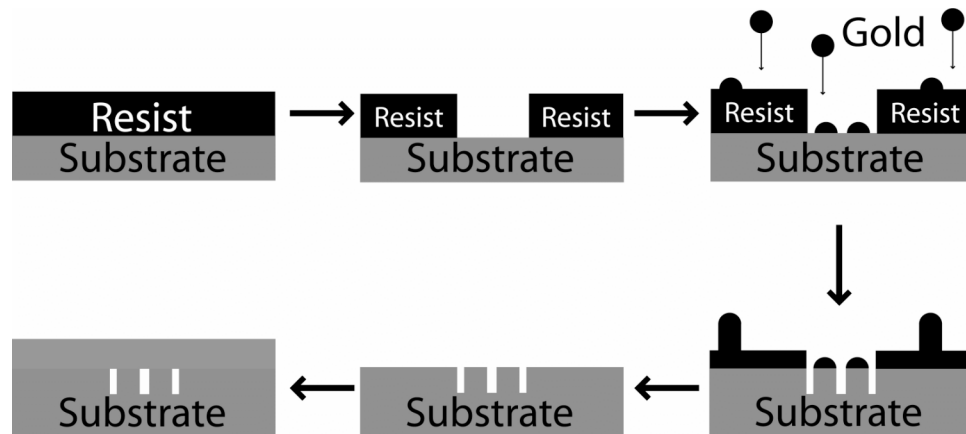


Figure 6.1: A schematic flow chart of the nanopillar fabrication process. Resist is patterned lithographically to define the microfluidic channels. Gold is evaporated into the lithographically defined channels and subsequently acts as the mask for the nanopillars. Reactive ion etching etches away the substrate creating a microfluidic channel filled with nanopillars. The gold and photoresist are removed from the substrate (in two separate chemical processes). If another layer of lithography is required, then the process can be repeated (with or without the gold). Otherwise, the devices can be bonded (as shown in the above) to seal the nanopillar-filled channels.

The gold is evaporated using a CVC SC4500 electron beam evaporator. The chamber pressure is less than 2×10^{-6} Torr, and the evaporation rate is about 0.1 nm/sec. A crystal monitor is used to measure the thickness of the evaporated film. For the gold island mask pattern, the gold does not form a film, but instead forms isolated islands of gold due to a repulsive interaction between silicon and the metal. For “film” thicknesses below about 7.5nm, isolated islands form. At about 10nm the gold islands begin to form a percolating network and the mask is no longer useful for forming pillars (one wants the gaps to percolate, not the gold). Throughout this dissertation, references to the film thickness should be interpreted to mean the amount of material evaporated as measured by the crystal monitor.

A collection of scanning electron micrographs is presented below. The quantity of micrographs is intended to illustrate the variety of structures possible with different etch conditions, melting conditions, and substrates. To summarize the figures: substrates for gold are silicon, fused silica, and photoresist; melting is done on a hot plate at 200C in atmospheric conditions; and etching is done using SF_6 , CHF_4 , or CHF_3+O_2 . To summarize the conditions ultimately used to make nanopillar devices for separating DNA (approximately the best conditions found): fused silica substrates, with 5nm of gold that is not melted, and the etching gas is CHF_3+O_2 . In all of the images, the darkness indicates the substrate.

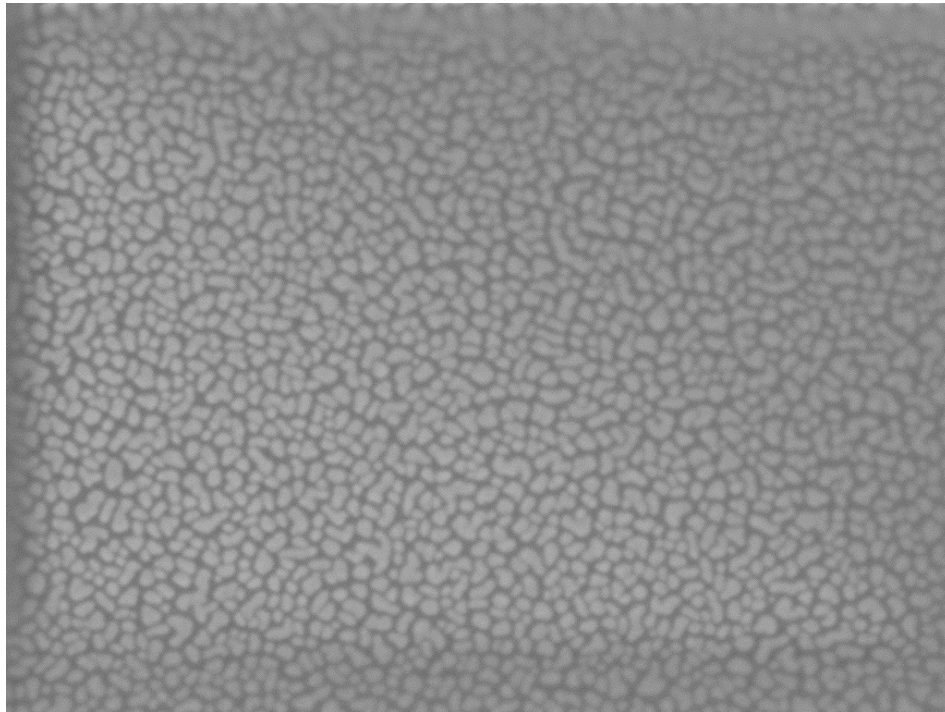
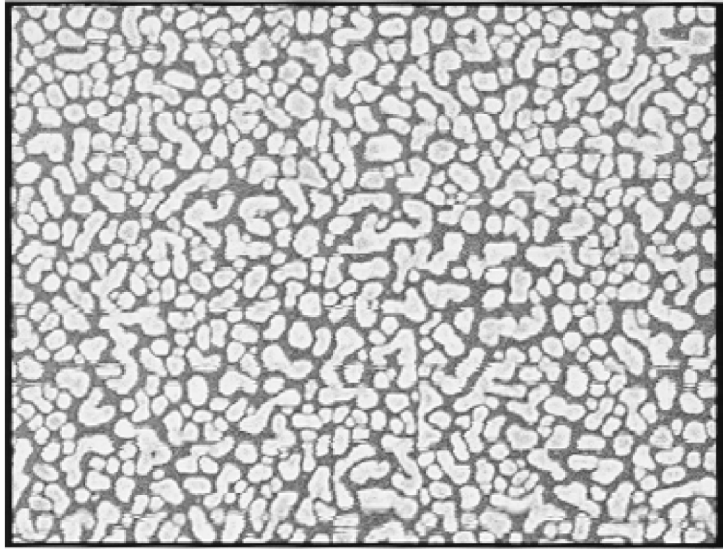


Figure 6.2: A scanning electron micrograph of a 5nm gold “film” on a silicon substrate. The gold forms the gold island pattern that is used as an etch mask for nanopillar structures. In this, and subsequent images, the brightness is the gold (or pillars) while darkness is the substrate.

5nm gold, 10min melt
100,000x magnification



5nm gold, 40min melt
100,000x magnification

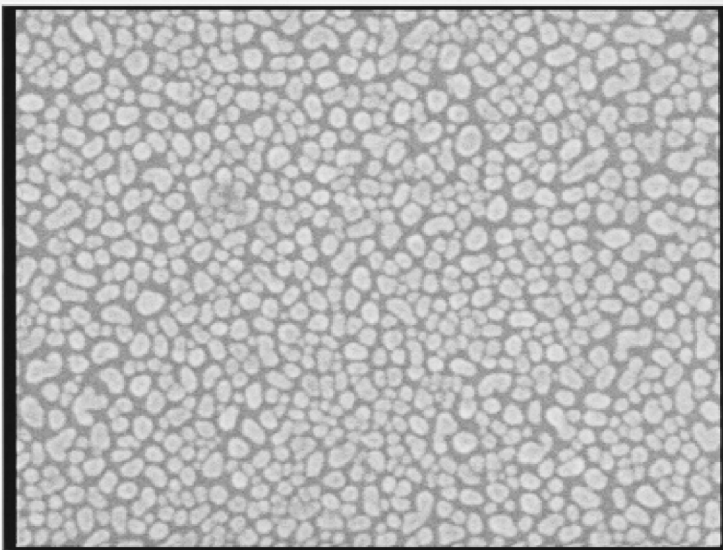


Figure 6.3: A comparison of scanning electron micrographs of 5nm of gold evaporated onto a silicon substrate and then heated at 200C for 10 minutes (top) and 40 minutes (bottom). The bottom image shows the effect of longer heating: the gold islands form more homogeneous, round structures.

5nm gold, 20min melt, 1min etch
150,000x magnification



Figure 6.4: 5nm of gold evaporated onto silicon, heated for 20 minutes, and then etched for 1 minute. The gold remains on the tops of the pillars, and this serves to highlight the three-dimensionality of the features. Note that near the edges of some of the bright spots (the gold), there is a fading of intensity. This indicates that the features drop down, into-the-page, and out of the depth of focus. Note the overall similarity of this mask pattern with that shown in the top image of Figure 6.3 (both were similar processes except for the etching).

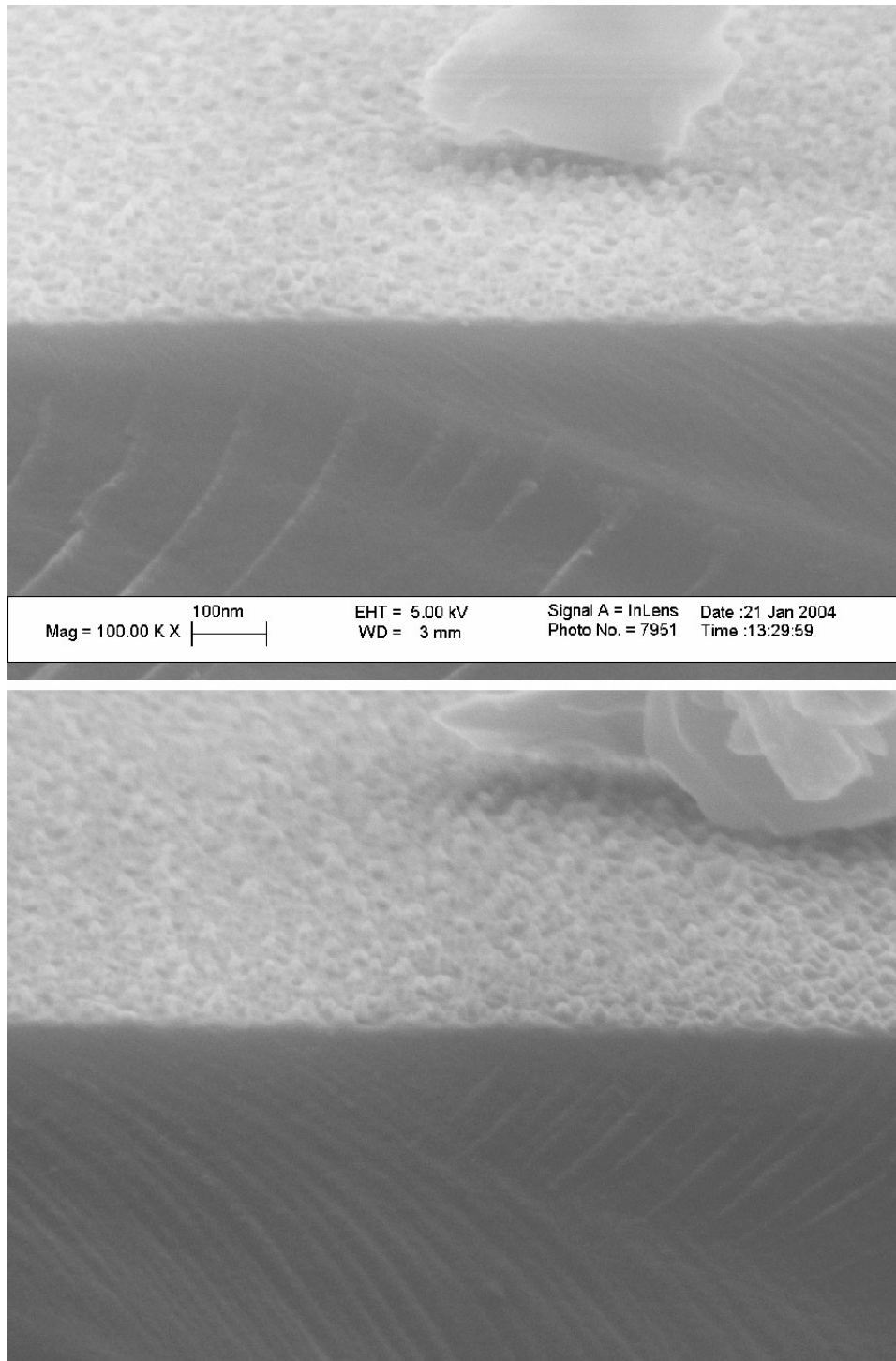


Figure 6.5: Top and bottom panels both show cross-sectional scanning electron micrographs of pillar structures formed after etching. The substrate is silicon. By comparison with the scale bar, pillars appear to be approximately 20nm tall, though there is clearly significant variation.

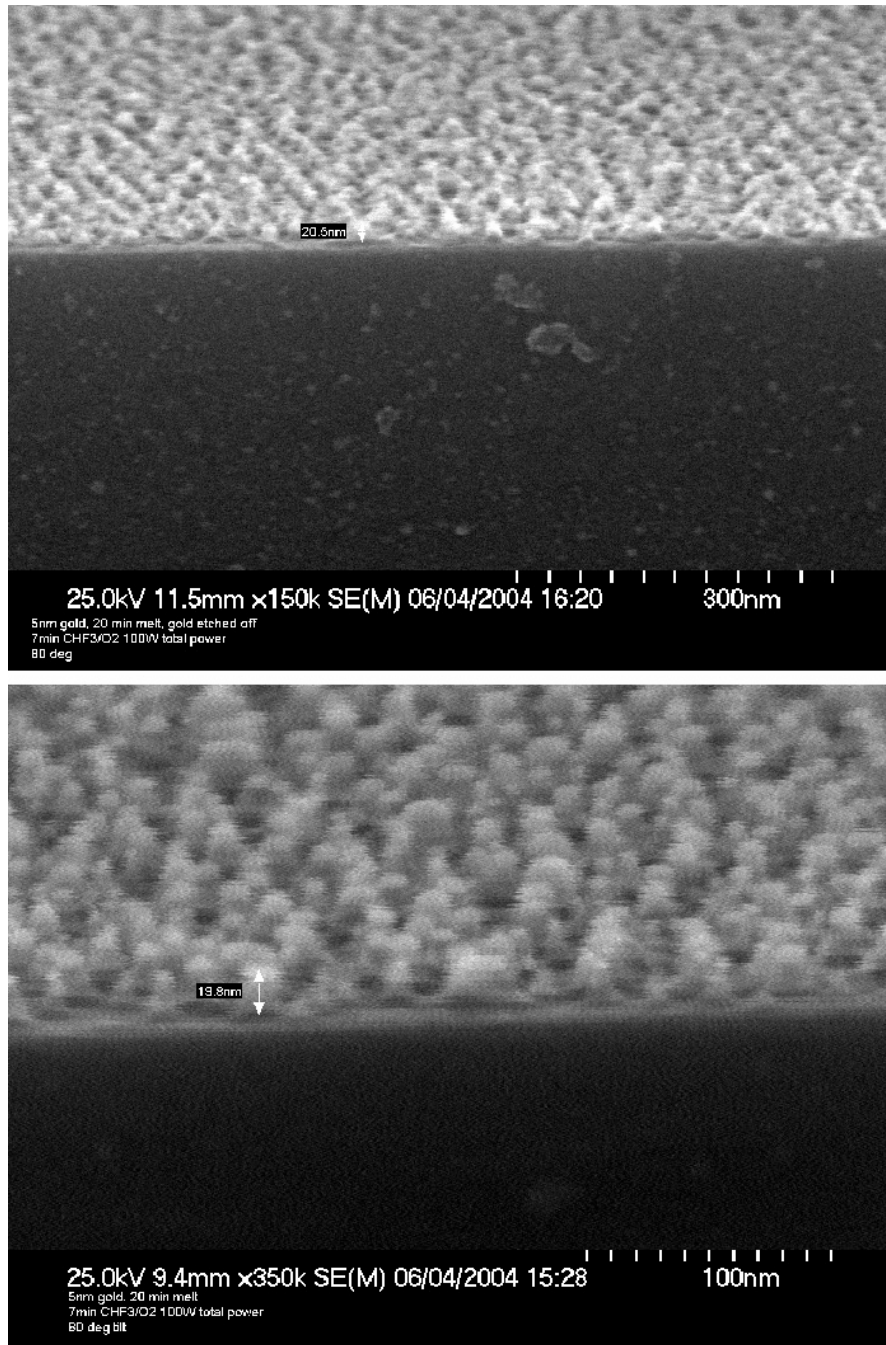


Figure 6.6: Two approximately 80° cross-sectional scanning electron micrographs of nanopillars fabricated using the gold island etch mask and CHF₃+O₂ for 7 minutes. The pillars appear mostly intact even though they have a slight taper to their tops. The arrow in the upper figure (difficult to see) marks an approximately 20nm tall pillar. The arrow in the bottom figure also marks an approximately 20nm tall pillar.

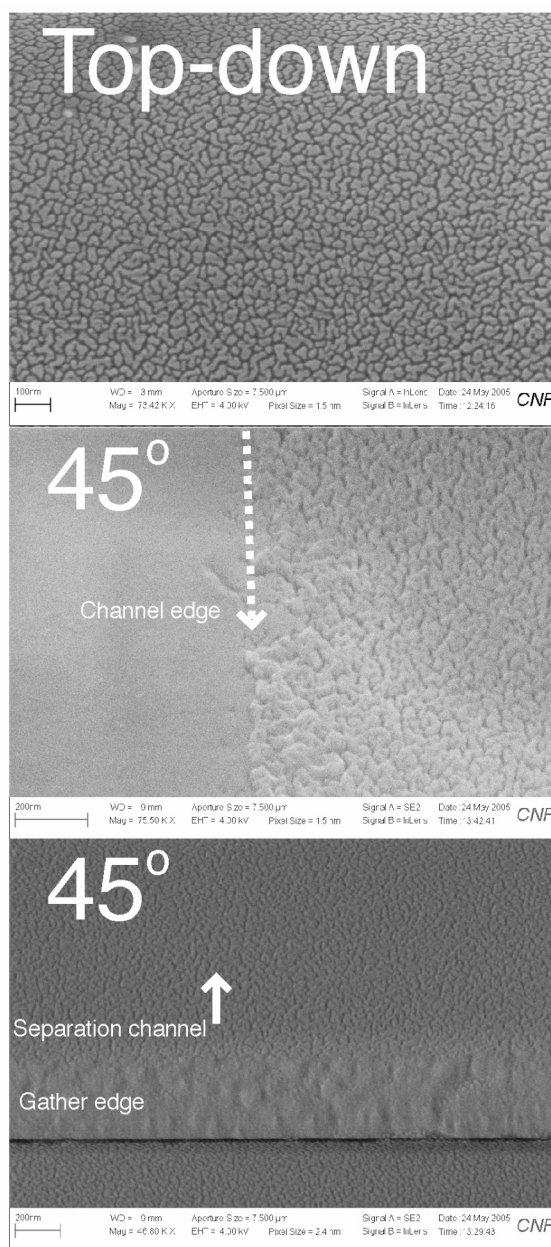


Figure 6.7: A collage of scanning electron micrographs of the gold island mask etched (and removed) into a fused silica substrate. The middle and lower images are taken at approximately 45°. The middle image shows the raggedness at the edge of the channel (at the edge of the protective photoresist). The lower image shows the step created by the two-level lithography process. The step defines the beginning of the separation channel and is used to collect and concentrate (gather) DNA.

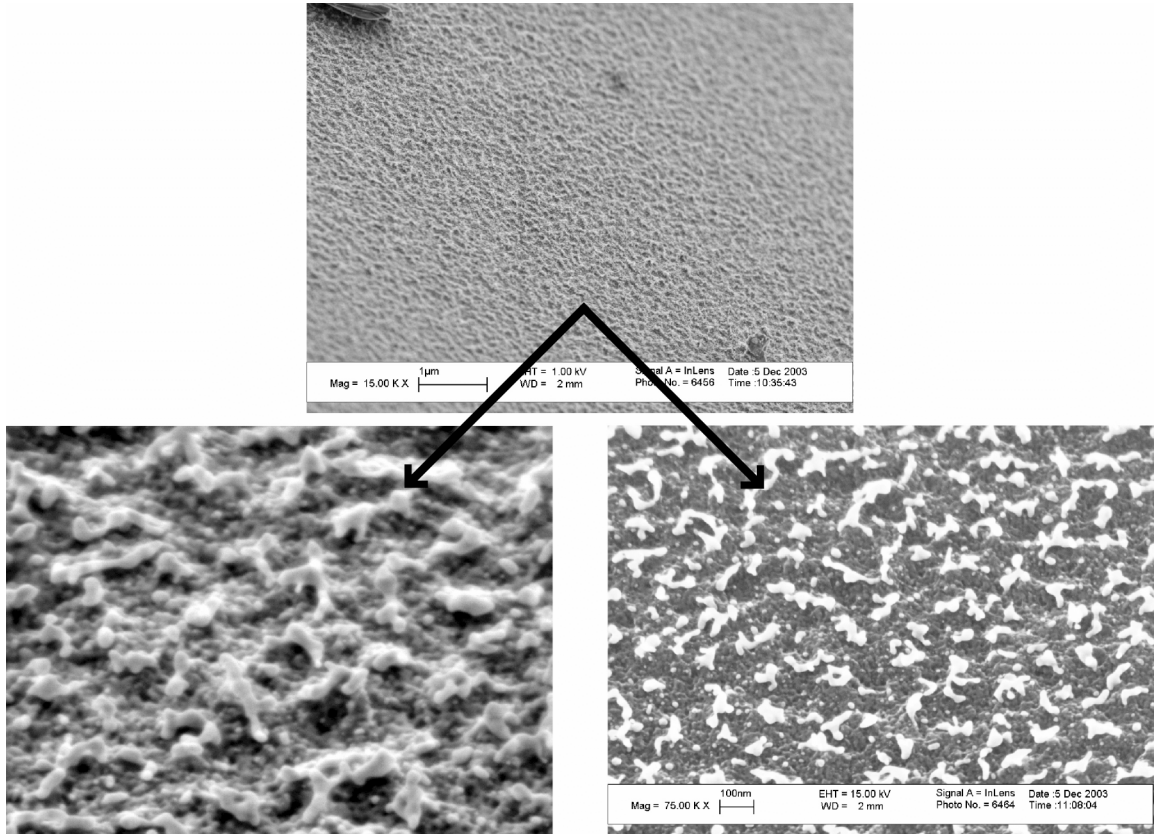


Figure 6.8: Examples of the gold island mask being destroyed by an SF₆ etch process. The upper image is a zoomed-out view of a wide area of roughened silicon, the remains of a short etch using SF₆. The lower left and right images show cross-sectional, close-up views (not of the same location) of the surface. The anisotropy commonly attributed to the SF₆ etch process is apparent in the overhangs visible in some of the features. Note also that the globular nature of the features is likely the result of re-deposition or sputtering of the gold during the etch process. For nanometer-scale, roughened, high surface area applications, this etch process might be ideal.

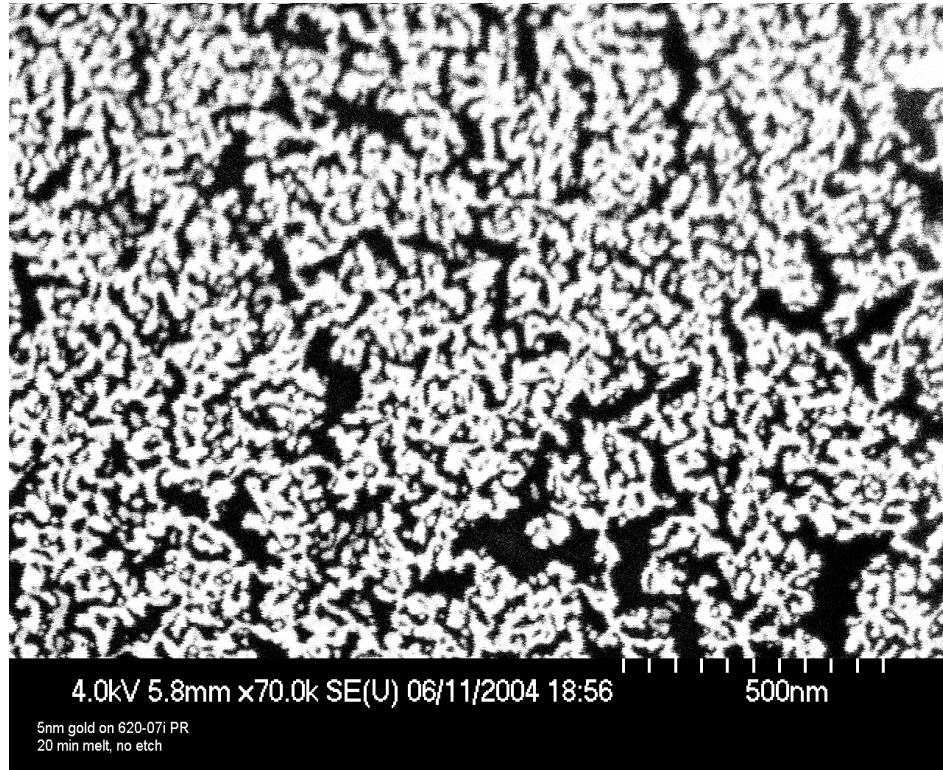


Figure 6.9: Gold evaporated onto photoresist. Gold exhibits a greater affinity for photoresist and the same quantity of gold evaporated onto photoresist is seen to form a nearly continuous film as opposed to the island-like film formed when the gold is evaporated onto silicon or glass. Because of the affinity of gold for photoresist, pattern transfer into photoresist is not feasible.

Various “treatments” were applied to the gold mask pattern to determine if the pattern could be manipulated to control the pillar size, the polydispersity of pillar sizes, or the width of the inter-pillar channels. ImageJ (NIH) and ImagePro+ software packages were used to quantify the “diameter” of the pillars and the inter-pillar channel widths from micrographs like those shown above. The following figures summarize the results.

As seen in Figure 6.10, heating tends to reduce the polydispersity of the pillars. The gold is mobilized on the surface by the heat and tends to coagulate. The free energy of gold on the surface sets the lower limit of the

droplet size. For each “film” thickness, there seems to be a lower limit on the droplet size achievable through heating. From Figure 6.10, this lower limit seems to be around 5nm for a 2.5nm thick film of gold. As shown above in Figure 6.9, gold tends to “wet” photoresist much better than it does silicon or silicon dioxide. Any amount of gold that was evaporated onto the photoresist surface was found to percolate, forming a continuous path of gold. Percolating gold is undesirable as it leads to nanopillar structures that are not open from one side to the other. That is, DNA cannot migrate through the structure.

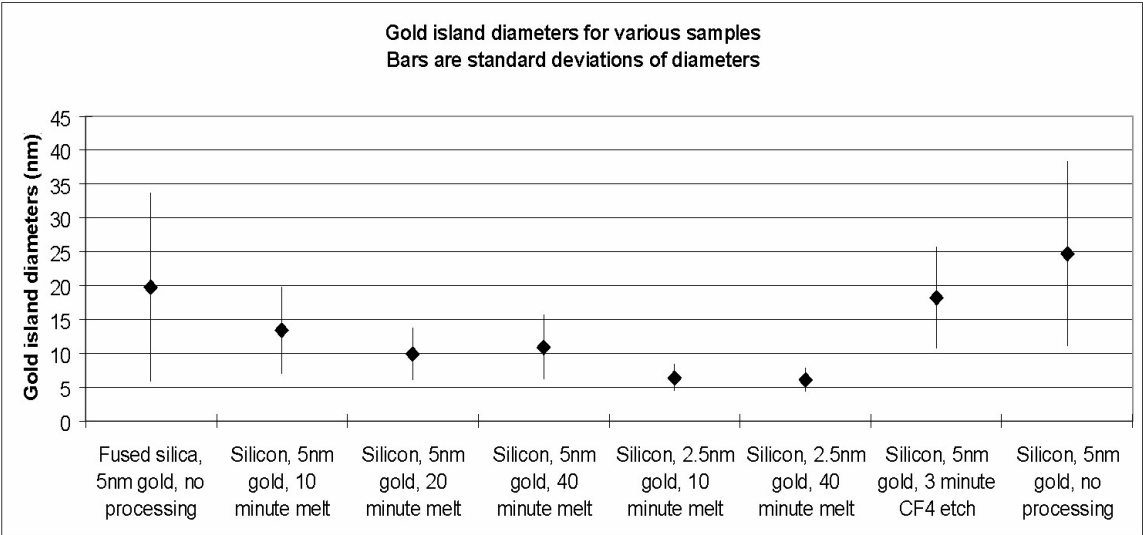


Figure 6.10: A figure showing the gold island diameters on silicon and glass wafers after various heating and etching process were performed. The bars are one standard deviation of the measured sizes. The sizes were quantified using ImagePro+. A “diameter” is taken to be the largest distance across each isolated, island-like structure. Heating for 10-40 minutes was used to mobilize the gold on the substrates. This process is referred to as “melting” in the figure labels. Evaporating less gold and heating for longer periods of time produces smaller diameter islands with less polydispersity.

**Histogram of diameters of gold islands
5nm gold on fused silica
Objects smaller than 10nm diameter rejected**

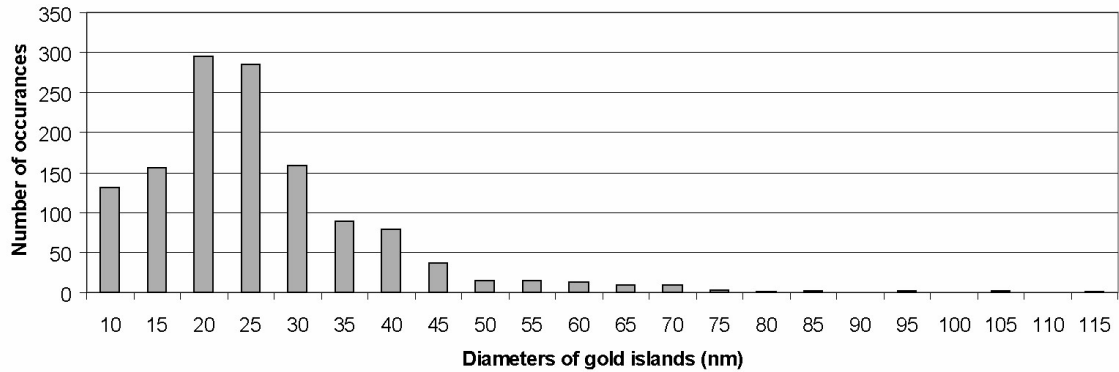


Figure 6.11: A histogram showing the polydispersity of gold islands using the most common evaporation recipe: 5nm of gold evaporated at 0.1nm/sec in a chamber pressure of $<2.0 \times 10^{-6}$ torr.

Figure 6.11 shows a histogram of diameters of gold islands on fused silica.

The figure gives an indication of the polydispersity of gold island sizes obtained for a typical 5nm gold evaporation. Most of the gold islands fall in the size range of less than 30nm.

6.3 Nanopillar Experiments

A schematic of the experimental setup is shown in Figure 6.12. DNA samples were stained with SYBR Gold (Invitrogen, Carlsbad, CA). SYBR Gold stock (at 10,000x concentration) was initially diluted 1:100 in 5x TBE. Then, the diluted SYBR Gold solution was added to DNA solutions at a further 1:10 dilution resulting in a 1:10 final concentration of SYBR Gold from the stock. DNA used in these experiments included 2kb, 10kb, λ -*Hind* III digest, and λ DNA molecules (all DNA from New England Biolabs, Ipswich, MA).

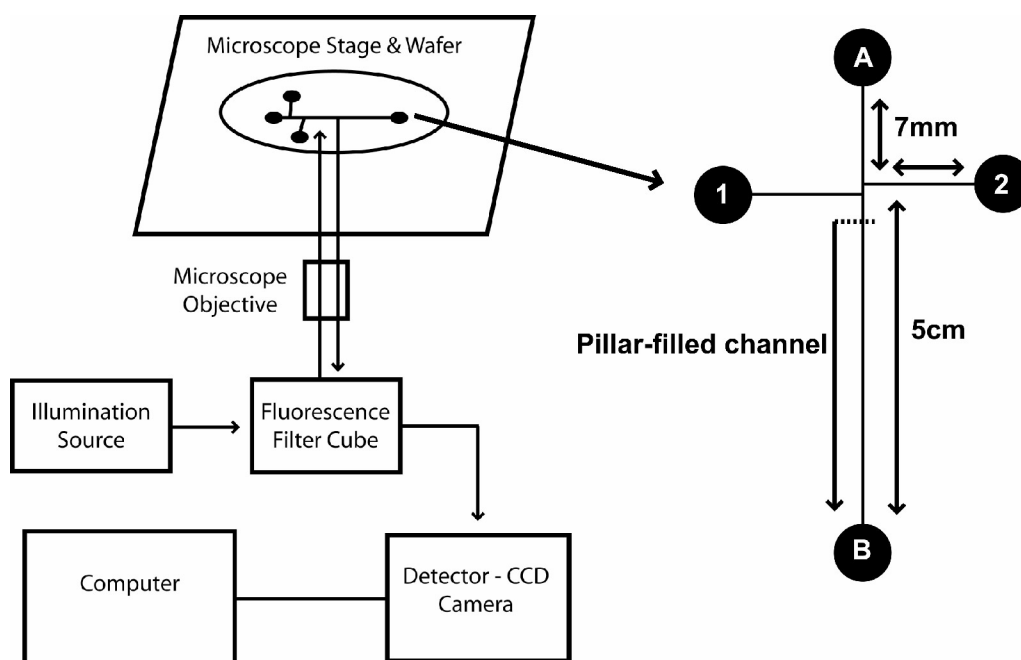


Figure 6.12: A schematic collage of both the experimental setup (left) and the microfluidic device (right). The pillar-filled separation channel is offset from the intersection by 250mm. Observations of the fluorescently labeled DNA molecules are made along 5cm length of the separation region.

For these experiments, DNA sample stocks were prepared at $5\mu\text{g/ml}$ in 5x TBE buffer containing 4% (v/v) β -mercaptoethanol as an anti-photobleaching agent and 2% (w/w) polyvinylpyrrolidone (PVP; MW = 10,000) used to suppress electroosmotic flow (all chemicals obtained from Sigma, St. Louis, MO). All channels were initially filled with 5x TBE with 2% PVP. Between experiments, channels were flushed with 5x TBE with 2% PVP by applying 2000V between opposite reservoirs. All experiments were done with DNA concentrations lower than the $5\mu\text{g/ml}$ stock concentration. DNA was introduced into the device via reservoir 2. Whenever DNA was diluted to a lower concentration from the stock solution, the dilution was performed in

reservoir 2 on the wafer by adding a volume of the DNA stock solution to an appropriate volume of buffer already in the reservoir.

Excitation of the fluorophores was accomplished with an Exfo X-Cite 120 fluorescence illumination system (Vanier, Quebec, Canada), and Chroma Technology Corporation (Rockingham, VT) filter set 41001 or Omega Optical (Brattleboro, VT) filter set XF100-2 were used. All data were collected using a 100x magnification oil-immersion objective from Olympus with a numerical aperture of 1.35. Experiments were performed at room temperature. To generate an electric field within the channels, a Stanford Research Systems (Sunnyvale, CA) DC power supply was used and gold wires were inserted into the reservoirs on the device.

Images and video were collected using a Photometrics (Tucson, AZ) 512B back-illuminated, thermoelectrically cooled CCD camera. MATLAB (The MathWorks, Natick, MA) was used to process and analyze images and video files. Intensity data were obtained from images or videos by adding the intensity values stored in the pixels of selected regions of each frame. An initial frame and a portion of each analyzed frame were used to adjust for variations in the background intensity caused by instability of the illumination source. No image processing was performed to generate intensity data.

To load DNA into the fluidic channels from reservoir 2, an electric field was established between reservoirs 1 and 2 (between 700V/cm – 1500V/cm). Within 30 -120 seconds a uniform stream of DNA filled the loading channels and the intersection. DNA in and near the intersection of the device was then gathered at the entrance to separation channel by holding reservoirs 1, 2, and A at ground relative to reservoir B. In the devices with artificial gel-filled separation channels, DNA molecules longer than 1000bp were not observed

to migrate beyond the interface between the open channel and the separation channel at gathering electrical fields of less than 99V/cm. In non-gel-filled separation channels, molecules as long as 2kb periodically crossed the interface at electrical fields as low as 49V/cm. The duration of the gathering phase was used to control how much DNA there was in the plug that was launched into the artificial gel. All experiments reported herein used gathering steps between 5 and 10 minutes in length with electrical fields of 24-99V/cm (25-100V applied between reservoirs). See Figure 6.13 for an example of the concentration process.

After the gathering phase, the DNA that was not in the plug was driven back towards reservoirs 1 or 2 by holding reservoir A at ground relative to reservoirs 1 and 2, which were held at 500V. Because the interface between the open channel and the separation channel is offset from the intersection by 250 μ m, the DNA in the plug was not disturbed during the drive-off phase. After the drive-off phase, a re-gather phase was performed holding reservoir A at ground relative to B with the same electrical field as used in the initial gather step. This was necessary because during the drive-off phase, the plug diffused slightly and some molecules in the 250 μ m length region between the beginning of the separation channel and the intersection were not driven to reservoirs 1 or 2. It was therefore necessary to “regather” those molecules and re-form the slightly diffuse plug prior to running the separation experiments. The drive-off phase was critical because when not performed, DNA left in the intersection entered the separation channel after the main plug was launched and showed up as noticeable signals late in the electropherogram. The regather phase is also critical both because the plug diffuses slightly during the drive-off phase and because there remains the potential for late-coming

DNA in the 250 μ m of channel between the intersection and the start of the separation channel.

6.4 Results

Concentration and electrophoresis experiments using the 2kb and 10kb DNA samples described above were performed in both pillar-filled devices and in pillar-free devices. In the pillar-free devices, which were used as control devices for the separation efficacy of the pillars, it was difficult to concentrate DNA at the loading channel-separation channel interface and no clear separation of DNA by length was observed. In contrast, the pillar-filled devices were capable of concentrating DNA even at relatively high electric fields and fully resolved a mixture of the 2kb and 10kb DNA fragments within minutes.

Figure 6.13 consists of three fluorescence micrographs showing how DNA molecules are concentrated at the interface between the pillar-filled channel and the loading channel. Panel A shows DNA in the intersection of the device. White lines are added to indicate the edges of the channels. The contrast is enhanced to more clearly show the 2kb molecules; the less prevalent, brighter spots are 10kb DNA molecules. If one were to operate these devices without the gathering phase, and simply inject the amount of DNA in the intersection down the separation channel, only the amount of DNA shown in panel A would go through the separation channel. The data would more resemble that of a single molecule experiment than a separation experiment in which bands of large numbers of molecules are observed. Panel B shows the interface between the loading channel and the pillar-filled separation channel at the beginning of the gather phase. The black dashed line indicates the interface between the two regions. The total voltage applied

between the reservoirs is 25V. Panel C shows the interface after 10 minutes of gathering DNA. The fluorescence saturates the camera and causes the gathered plug to appear as if it is entering the pillar-filled channel. The amount of DNA in the gathered plug in panel C is such that bands, not individual molecules, are observed when the separation experiment is performed.

Gathering steps were typically carried out at 50-100V applied between the reservoirs. Even when 200V were applied, however, little if any “leaking” of 2kb and 10kb DNA into the separation channel was observed. In contrast, in the control devices that did not contain the artificial gel structure, 2kb DNA was observed to leak into the separation channel even when only 25V was applied between the reservoirs. Thus, it is possible to use the interface between an open channel and an artificial gel-filled channel as an integrated structure for concentrating DNA. In experiments conducted using a λ -*Hind* III DNA digest (1-2.5mg/ml concentration), the smallest fragments (125 and 564bp) were observed to leak into the artificial gel at higher applied voltages (above 50V). It is therefore possible to use the interface between the loading channel and the artificial gel-filled channel as a size-selective (and voltage-dependent) concentrator or filter.

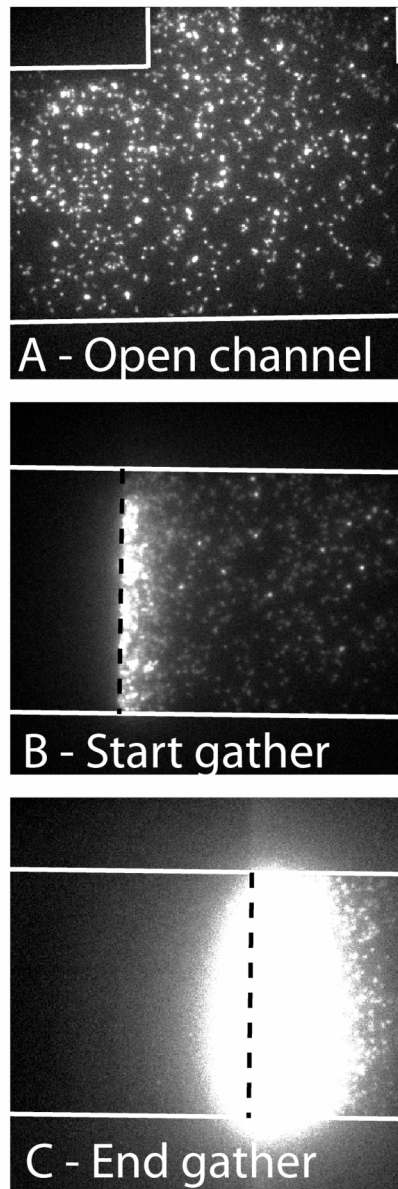


Figure 6.13: A collage of fluorescence micrographs showing the evolution of the gathering plug of DNA at the entrance to the separation region. A) The intersection is shown (not the boundary between the separation region and the loading channel). Larger, brighter dots are 10kb DNA molecules and smaller dots are 2kb DNA molecules. B) Less than one minute into the gathering phase. This image is taken at the boundary between the separation region and the loading channel (demarcated by the black dotted line). Note that the intersection shown in A is not visible in B (or C). C) The same region as shown in B, but after having waited 10 minutes. The intensity “spills” over the demarcation line because the camera is saturated, not because DNA actually extends across the boundary.

Electrophoresis experiments were conducted at distances of up to 3.5cm in the gel-filled devices over a range of applied electric fields. Figure 6.14 shows the results of experiments as observed 3.5cm along the gel-filled separation channel at a number of applied voltages. There was separation of the 2kb and 10kb DNA fragments even at relatively high electric fields (700V or 693V/cm; inset). At the highest field at which separation occurred (693V/cm), the process took about 155 seconds. Within the bands, single molecules were observable in the videos of the separation process, and it is clear that the 2kb DNA fragments moved faster than the 10kb DNA fragments.

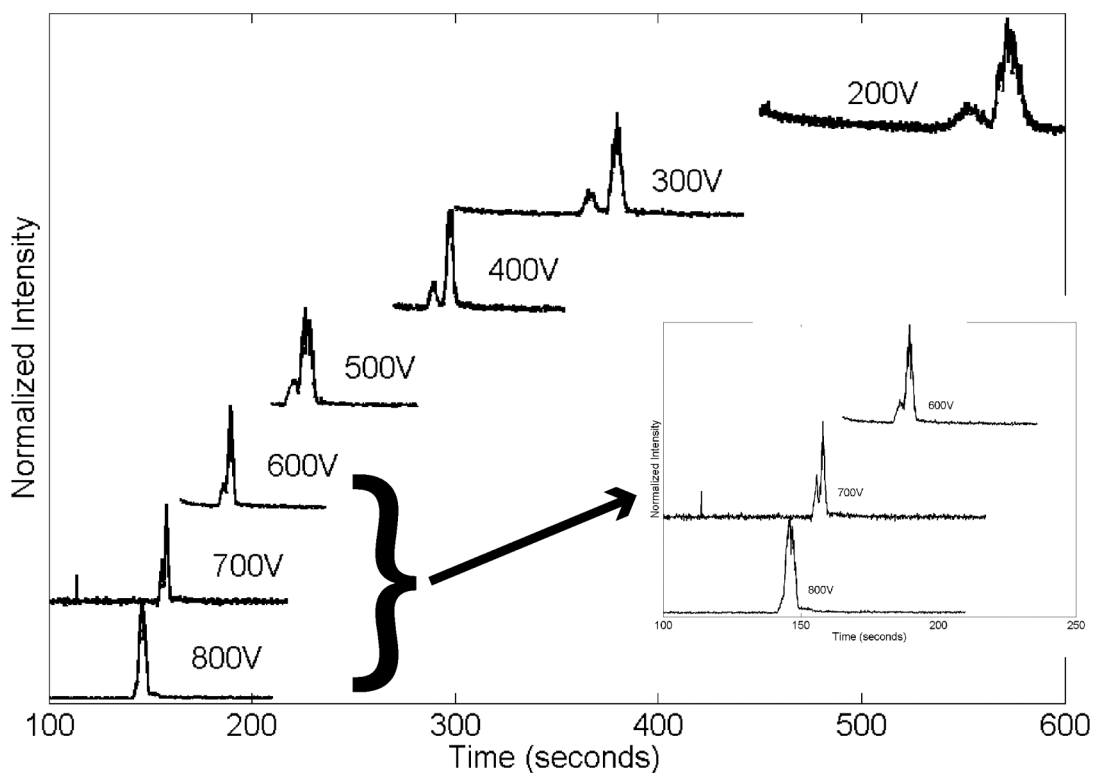


Figure 6.14: Results of running 2kb and 10kb DNA through a pillar-filled channel at various voltages. For applied voltages up to 700V (see inset for clarity) the two fragments fractionate. At 800V the resolving power of the matrix fails.

As others have reported that surface interactions are sometimes sufficient to separate DNA molecules by length [122, 123], and as the separation channels used in these experiments had a relatively substantial surface to volume ratio, channels without the pillars were used to control for the effect of surface interactions on the separation process. Experiments performed in the pillar-free separation channels showed that the 2kb and 10kb DNA fragments were not separated even after 3.5cm (Figure 6.15). Experiments in pillar-free separation channels were performed at electric fields as low as 49V/cm and no separation of the DNA species was observed.

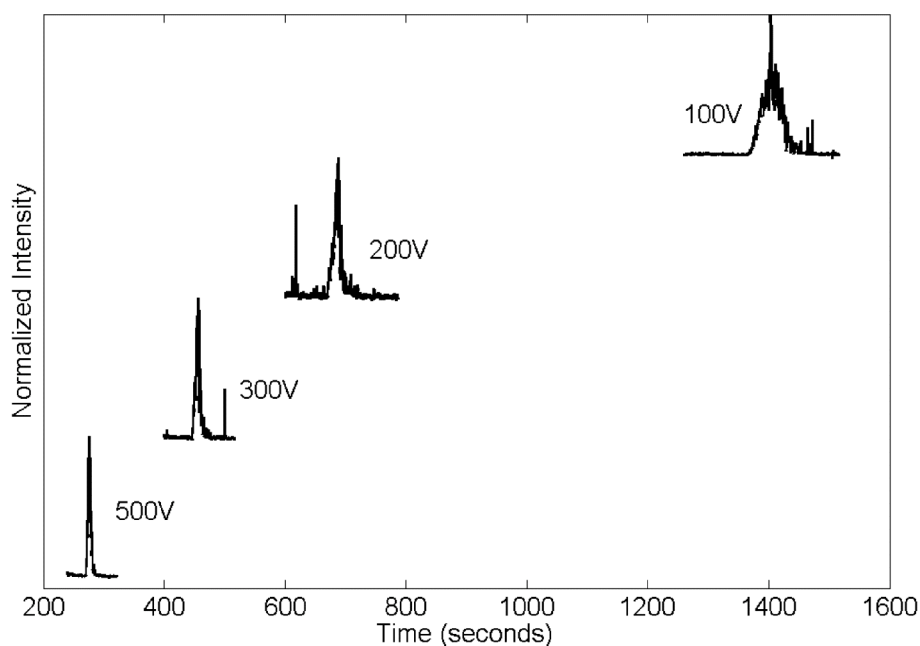


Figure 6.15: Results of running 2kb and 10kb DNA in a pillar-free separation channel. Even at the lowest applied voltage, no separation of the fragments is achieved. Note that in the 100V, 200V, and 300V curves, there are sharp spikes (behind the main peak in the 100V and 300V curves, and ahead of the main peak in the 200V curve). These spikes are clumps of DNA, transiently stuck to the channel walls, that happened to unstick and pass through the observation region during the experiment. After performing tens of experiments in these devices such sticking and releasing is often observed.

A common way of defining the resolution of an electrophoresis experiment is

$$R = \frac{\Delta t}{.5 \times (w_1 + w_2)}, \quad (6.1)$$

where Δt is the time between the centers of two peaks, and w_1 and w_2 are measures of the widths of the two peaks. Gaussian curves were fit to the peaks and the full width at half of the maximum peak value was used as a measure of the peak width. Table 6.1 summarizes the separation resolution of the 2kb DNA and 10kb DNA fragments for conditions at which separation experiments were performed. A resolution of 0.5 indicates that two peaks overlap at their half-maximum values; this is generally the criterion used to declare that two peaks have been resolved.

Table 6.1: The resolution of the separation of 2kb DNA from 10kb DNA using the artificial gel-filled channels at various observation lengths and total applied voltages (voltage listed is voltage applied over the entire 5.7cm length of the device). Resolution is computed using Equation 6.1.

<i>Length, Voltage</i>	<i>Resolution</i>
2cm, 50V	2.5
3cm, 50V	3.5
-----	-----
2cm, 300V	1.6
2cm, 400V	1.6
-----	-----
3.5cm, 300V	2.6
3.5cm, 400V	2.4
3.5cm, 500V	1.5
3.5cm, 600V	1.4
3.5cm, 700V	1.6

The separation resolution increases as the length of the separation region is increased. In all of the experiments except the experiment at 3.5cm

and 700V, the resolution also decreases as the total applied voltage is increased. This is consistent with the idea that at sufficiently high voltages the DNA molecules transition from the regime of Ogston sieving to reptation. It is also consistent with a model in which surface interactions (such as fast, transient sticking, and friction) dominate the separation process. In such a model, high driving forces would dominate transient surface interactions and no separation would occur.

Figure 6.16 shows four fluorescence images of λ DNA and concatemers of λ DNA moving through the pillar-filled channel. The four-image sequence takes place over 325ms and highlights how molecules interact with the nanopillar structures. There is an applied electric field of 297V/cm throughout the sequence and the molecules are moving to the left in each image. There is a molecule in the upper center of each image that is apparently stuck in the matrix and elongated to about $10\mu\text{m}$ (the length of the white scale bar just above the stuck molecule is $10\mu\text{m}$). There is also a cluster of at least two molecules in the lower right of each image that is also stuck throughout the entire sequence. Eventually these molecules release from the structure and continue moving through the separation channel.

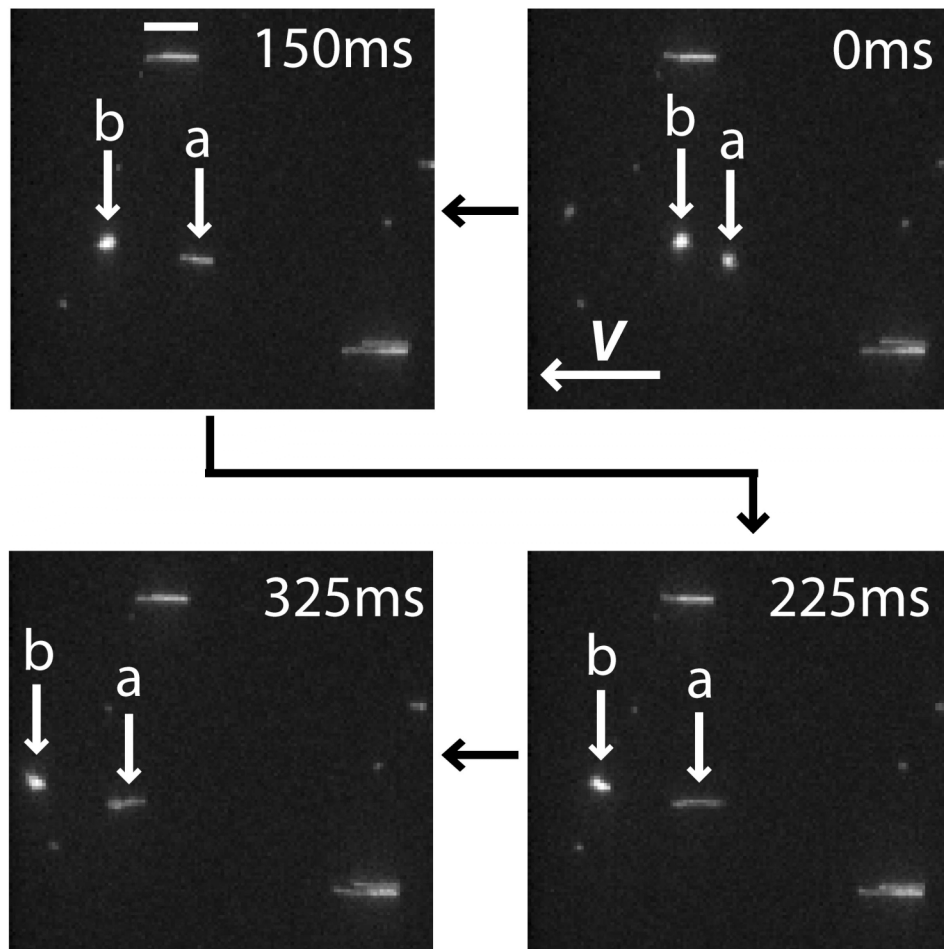


Figure 6.16: A four-panel collage (325ms elapsed time) showing two I DNA molecules moving through a pillar-filled channel. The molecules are driven to the left by an applied electric field of 297V/cm. At 0ms, both molecules are in relaxed states. In the 150ms frame, molecule A has gotten stuck on a pillar and is elongated. Molecule B remains globular. After 225ms, molecule A remains entangled with the pillar, though it appears to have partially slid off the pillar, while molecule B appears to deform slightly as it interacts with a pillar. After 325ms, molecule A disentangles from the pillar while molecule B has nearly moved out of the field of view.

Two molecules are highlighted in each image of Figure 6.16. Molecules A and B begin the image sequence in their relaxed states. In the second image, molecule A elongates upon a fiber of the artificial gel. In the third

image, molecule A has just finished sliding around the fiber and has come free. Finally, in the fourth image, molecule A begins to relax again, starting with its leading edge. Throughout the entire sequence, molecule B moves just alongside molecule A but does not appear to interact strongly with the artificial gel structure.

I performed separation experiments with the 2kb and 10kb DNA with the addition of λ DNA in the mixture. Figure 6.17 shows the results of two such experiments, with differing concentrations of each species. The transient sticking of λ DNA molecules (and λ DNA concatemers) is apparent in both panels A and B. Even with a relatively low concentration of λ DNA, as in panel A, the λ DNA peak is very broad. At higher λ DNA concentrations, as in panel B, the “noise” from unsticking molecules significantly degrades the resolution of not only the λ DNA peak, but also the 10kb and 2kb peaks. The noise occurring before the main λ DNA peak in panel B is caused both by relatively fast λ DNA from the actual experiment performed and from λ DNA stuck for a very long time in the channel between experiments (such as those in Figure 6.16 that remain stuck throughout the four image sequence).

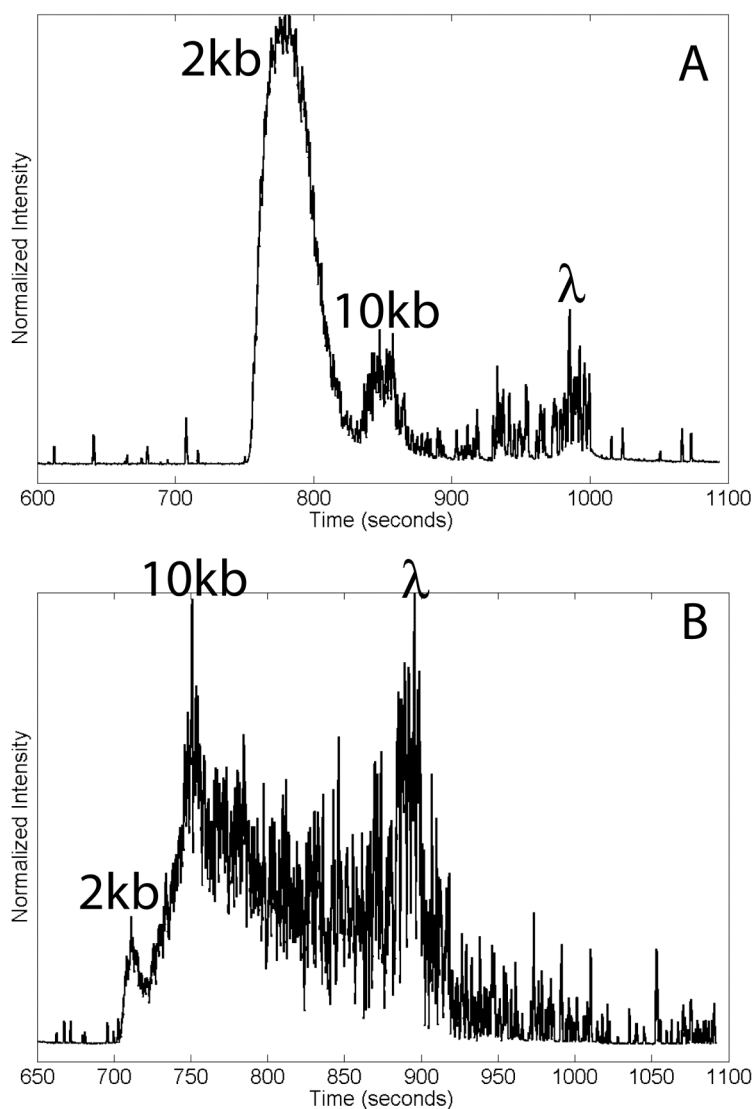


Figure 6.17: Two experiments showing the separation of 2kb, 10kb, and λ DNA (48kb). A) 100V, 2cm, 2kb at 1.875mg/ml, 10kb and λ DNA at 625ng/ml. B) 200V, 3.5cm, 2kb DNA at 217ng/ml, 10kb DNA at 434ng/ml, and λ DNA at 2.17mg/ml. The effect of long molecules unsticking is prevalent in both data sets (the high frequency spiky-ness that overlays the three elution peaks).

Others have observed that DNA molecules in nanometer-scale channels stretch out to a significant fraction of their contour length, even when they are allowed to relaxed [45, 46, 103, 104]. Such elongation is not observed

in our devices, even though the channel dimensions in the artificial gel appear to be about 10nm×50nm. Our observations of DNA in the nanopillar separation region suggest that the DNA molecules are not highly confined (see Figure 6.16, for example). This in turn suggests that the structure of the fully bonded artificial gel is not well represented by the scanning electron micrographs in Figure 6.7. The micrographs suggest that the gold island pattern is faithfully transferred into the fused silica substrate. However, it is possible that the ceiling of the device (formed by the 170 μ m thick wafer during bonding) is slightly bowed away from the top of the structure. Roughness at the edge of the channel, the photoresist edge, might be responsible for such bowing if it exists. Gold is also observed to sputter during reactive ion etching, so during the etch process the etch mask is actually redepositing on the surface or being removed from the surface entirely (see Figure 6.4). Redeposition would cause the channels to be shallower and the pillars to be more pyramidal than cylindrical in shape (as seen in Figures 6.5 and 6.6). Removal of the gold from the surface would have the effect of creating short pillars or pyramids that would not touch the channel ceiling. Thus, the cross-section through which the DNA molecules move is – even in the best possible scenario – not a uniformly ~10nm wide by 70nm tall channel. It is also possible that during the annealing step, the artificial gel structure deforms. The glass transition temperature of fused silica is 1042C (the devices were annealed at 1045C) and the softening temperature is 1585C. Though it seems unlikely, another possibility is that the free energy associated with the approximately 10nm×70nm pillar-like structures may decrease the softening temperature sufficiently so that the structures deform during the annealing step.

With optical microscopy, one observes the artificial gel structure to be clearly different than the gel-free channels. The difference is not simply that the gel-filled region is etched less than the open channels. The gel-filled areas appear hazy and quite dim, indicating that significant scattering of light is occurring. This is consistent with the idea that the pillar-like structures are at least partially intact in the bonded device. A cross-sectional scanning electron micrograph of a bonded and cleaved gel-filled channel may indicate what the structure actually looks like after bonding and annealing. No such images have been obtained.

When filling the device with buffer for the first time, the gel-filled channel fills significantly differently than smooth, square cross-sectional channels do. The liquid fills the gel-structure with thin, branching tendrils that advance through the channel very haltingly. The concave meniscus observed during normal capillary filling is observed when the gel-free loading channels are filled.

As one last piece of evidence in support of at least partial preservation of the pillar-like gold island pattern, if one tries to perform experiments in the devices using only 5x TBE buffer (the same buffer used in these experiments without the addition of 2% PVP), significant electroosmotic flow is observed in the gel-filled region. Typically, 5x TBE is of sufficiently high ion concentration that electroosmotic flow is suppressed even in devices as thin as 70nm in one dimension [25, 28, 43-46, 58, 124]. I found that when using only 5x TBE, electroosmotic flow from the gel-filled region into the open channels was sufficiently high that DNA could not be driven into the gel-filled region. The large electroosmotic flow is probably due to the significant fraction of the total channel area filled by the charged double layer in the artificial gel region. That

is, in the nanometer-scale channels, the small Debye layer was still a significant fraction of the total channel width. It is only with the addition of 2% PVP in the buffer that the electroosmotic flow in the gel-filled region is decreased to the point of being able to perform electrophoretic experiments. PVP has been used by others as both a sieving medium and as a method of controlling electroosmotic flow [8, 125, 126]. Note that in the Kaji *et al.* reference, no mention is made to the possibility of PVP causing the separation they observe. In our experiments, the use of PVP was crucial in controlling the electroosmotic flow, though I did not observe it to act in a sieving capacity (the lack of separation in the control devices without the artificial gel structure supports this claim, as PVP was used in the buffer in these devices).

Finally, I performed experiments using λ -*Hind*III digested DNA. Examples of the results of trying to separate λ -*Hind*III in pillar-filled channels and pillar-free channels are shown in Figure 6.18. In panel A, one sees that the digest was separated into approximately four peaks (the “peak” assignment was done by comparing the quantitative information – that shown in the figure – with the video in which the sizes of the molecules are clearly distinguishable). The digest normally consists of the following lengths of DNA (all in bp): 125, 564, 2027, 2322, 4361, 6557, 9416, 23130. During the gathering phase, it was clear that the smallest two fragments (125 and 564bp) were not trapped by the boundary at the gathering voltage used. Furthermore, I did not heat the sample prior to electrophoresis, so the cohesive, sticky ends of the 23130bp and 4361bp fragments were probably joined (this was confirmed by gel electrophoresis of the sample; data not shown). Not heating the sample effectively created a single 27kbp fragment. Therefore, the four

peaks in Figure 6.18A represent a nearly complete separation of the λ -*Hind*III digest in the pillar-filled channel.

From an engineering perspective, the λ -*Hind*III results shown in Figure 6.18A are not that impressive. Obviously, the digest was not fully separated. If the digest had been heated, breaking the 23kb and 4kb fragments apart, then it is likely that these fragments would have blurred the results and degraded the resolution (by shifting to the left the slowest peak and by adding a peak somewhere in the middle where there is not that much extra room). Even if the digest had fully separated, the experiment took about 12 minutes, which is only 2-4 times faster than separating the molecules using agarose gel electrophoresis. While the separation presented in Figure 6.18A is not that impressive, the results shown in Figure 6.18B are (or, at least, are interesting).

In Figure 6.18B, the λ -*Hind*III digest is driven through a channel that is otherwise identical to the pillar-filled separation channel except that it contains no pillars. Note that the time resolution of the experiment presented in Figure 6.18B is less than that of other, similar experiments; hence the coarse nature of the data. As can be seen in Figure 6.18B, there is a minor amount of fractionation of the DNA molecules. When one analyzes the video and compares the observed DNA molecules with the quantitative data, one sees that the slower peak is wholly comprised of the longest molecules (27kb), whereas the faster moving peak is comprised of all of the shorter molecules.

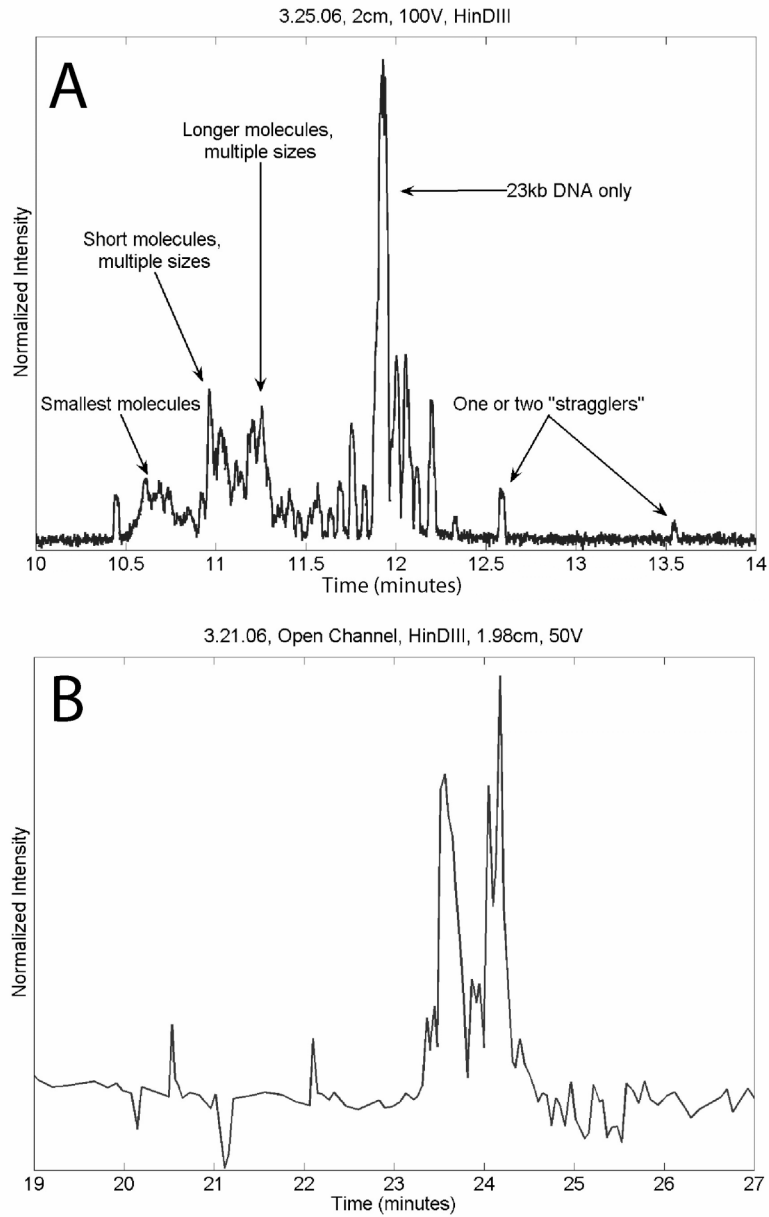


Figure 6.18: Electropherograms of λ -*Hind*III digest, 1.98cm effective column length. A) Results in a pillar-filled channel using an effective electric field of 99V/cm. B) Results in an open channel using a 49V/cm applied electric field.

6.5 Conclusions

Using the artificial sieving matrix incorporated into a microfluidic channel, I was able to separate relatively long DNA molecules by length in a relatively short period of time. Loading, gathering, launching, and ultimately separating DNA molecules is straightforward using the nanopillar geometry. Owing to their small sizes and close spacing, it was originally hoped that the nanopillars would be effective for achieving high-resolution separations of short DNA molecules (similar to sequencing). Unfortunately, the structures did not work as well as had been hoped for and single base resolution was not achieved. However, the devices were capable of separating long DNA molecules by length in shorter time periods than currently possible using gel electrophoresis.

Observations of the separation process indicated that the nanopillars were probably not as faithfully reproduced in the microchannels as had originally been thought based upon top-down and cross-sectional scanning electron micrographs of the un-sealed devices. Thus, the fabrication process and the nanopillar structures may be worth revisiting at some future time. Additionally, the high-surface area afforded by the pillars could possibly be used for sample purification applications or for affinity binding applications in which a tag-molecule is bound to a surface and a target-molecule is washed over the surface. This last application is currently being investigated by others within the Craighead research group.

Finally, after staring at DNA moving in these devices for long enough, I was prompted to investigate the surface interactions of DNA molecule in nanoslit-like devices. The observation of at least partial separation in a nanometer-scale channel prompted me to investigate whether or not

interactions with channel walls might cause enough friction to be able to separate DNA by length in a gel-free channel. The channel itself, lacking the pillar structures, is possibly thought of as a free solution environment, though the nano-scale height is such that DNA is forced to interact with the walls as it moves down the channel. Thus, the notion of free solution electrophoresis may no longer be valid for DNA in very thin nanoslit-like channels. In the next chapter, I will discuss a theoretical model for DNA moving in nanoslits as well as present data that validate the theory.

CHAPTER 7

NANOSLIT DEVICES

7.1 Introduction

DNA separation experiments in the nanopillar devices discussed in chapter 6 prompted me to investigate the effect of highly confining environments on DNA mobility. As shown in Figure 6.18, even in pillar-free channels, some fractionation of DNA by length was observed. Frictional interactions between the DNA molecules and the channel walls seemed to be the most likely explanation for the fractionation and testing that hypothesis was relatively straightforward. Elizabeth Strychalski manufactured nanoslit fluidic devices with critical dimensions of 19nm. DNA separation results in these nanoslit channels confirmed the hypothesis that surface interactions caused the DNA molecules to separate by length. While the separation afforded by these nanoslit devices is not remarkable from a technical standpoint, the results highlight that macroscale notions of DNA migration do not always transfer to the microscale. In this case, the notion of free solution electrophoresis (which does not provide length dependent separation for DNA) is seen to be invalid for very thin nanochannels.

This chapter is partly reproduced from a paper submitted to the Physical Review Letters. Modifications to the manuscript have been made to facilitate its inclusion in the whole of this dissertation, and new conclusions have been drawn relating to long DNA separations and estimates of the fit parameters. Co-authors on the paper were Elizabeth Strychalski and Harold Craighead.

7.2 Nanoslit Experiments

Nanoslit devices are used to separate DNA molecules by size. We use DNA molecules between 2kb and 10kb in length for these experiments. Devices are fabricated in fused silica substrates using essentially the same procedure as used to manufacture the nanopillar devices described in chapter 6. However, the nanoslit devices contain no gold evaporation step so they are somewhat simpler to make.

Two devices were used for the experiments reported herein. One device consisted of 540nm deep loading channels coupled to a 70nm deep separation channel. The other device had 650nm deep loading channels coupled to a 19nm separation channel. A schematic of the devices is shown in Figure 7.1A. Note that one of the loading reservoirs is omitted in this device geometry, as compared to the geometry described in chapter 6 (compare to Figure 6.12). The distance from reservoir 1 to the intersection is 2cm, and the distance from reservoir 2 to the intersection is 1cm. There is a 250 μ m offset from the intersection to the beginning of the shallow separation channel. The devices with 19nm deep separation regions had 3cm long separation regions, while the devices with 70nm deep separation regions had 4cm long separation regions. Data were collected 2.4cm and 3.5cm from the injection point for the 19nm and 70nm devices, respectively.

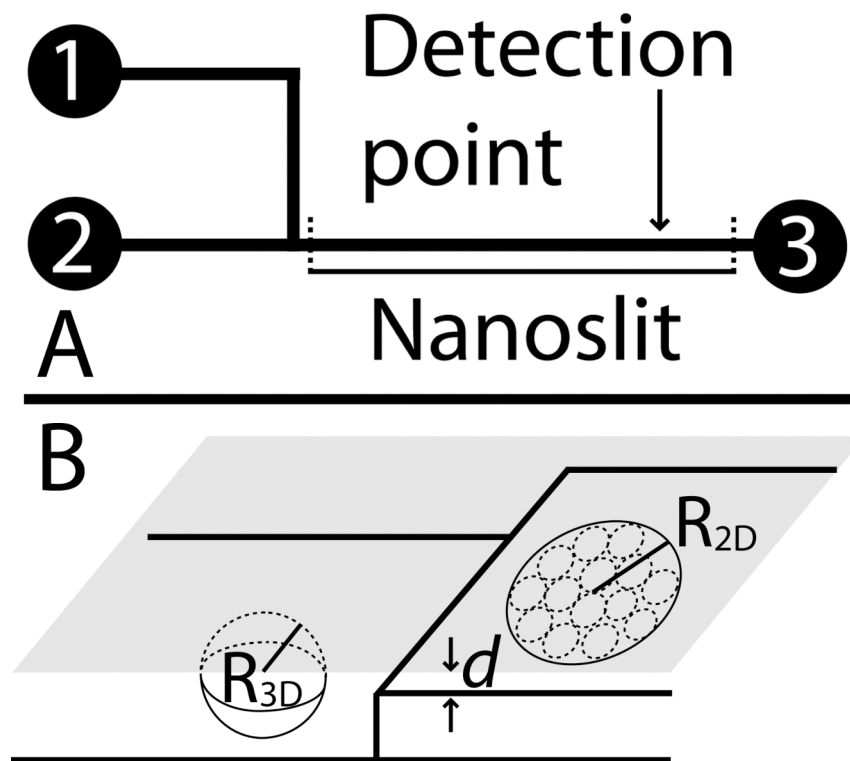


Figure 7.1: (A) A top-down schematic of the nanofluidic device. The nano-slit separation channel is offset from the intersection by 250mm to facilitate DNA plug formation and launch. The separation channel is 3-4cm in length depending upon the device. (B) A cross-sectional schematic of the transition of DNA from its three-dimensional, relaxed state to its two-dimensional squished state when forced into a nanochannel. In two-dimensions, the molecule becomes a pancake-like entity composed of sub-blobs of DNA each with a diameter equal to the channel height. Devices used herein had deep regions of 540nm and slit height, d , of 19nm.

DNA was initially loaded in reservoir 1 and driven into the channels by applying between 700V/cm and 1500V/cm between reservoirs 1 and 2. DNA near the intersection of the device was gathered into a plug at the entrance to the separation channel by holding reservoirs 1 and 2 at ground relative to reservoir 3, which was held between 50V and 200V. The duration of the gathering phase was used to control the quantity of DNA in the plug. After the gathering phase, the DNA that was not in the plug was driven back towards

reservoir 1 by holding reservoir 1 at ground relative to reservoir 2. The drive-off phase is critical; when not performed, DNA left in the intersection enters the separation channel after the main plug is launched and appears late in the electropherograms. Because the interface between the open channel and the separation channel was offset from the intersection by 250 μ m, the DNA in the plug was not disturbed during the drive-off phase. After the drive-off phase, a re-gather phase was performed holding reservoir 3 at ground relative to 2 with the same applied voltage as used in the initial gather step. The regather phase re-groups the DNA into a sharp band, and is necessary due to diffusion of the plug during the drive-off phase. The DNA plug was driven into the separation region by applying a short (1-2 seconds) 1000V pulse. After the molecules were driven into the separation region, the separation voltage was reduced to a constant voltage for the duration of the experiment.

The experimental setup is identical to the setup described in chapter 6. DNA are prepared as described in chapter 6. DNA are obtained from New England Biolabs and include the lengths: 2kb, 3kb, 5kb, 8kb, and 10kb.

We performed electrophoresis experiments in both the 19nm and 70nm deep channels with mixtures of DNA molecules. Examples of three experiments are shown in Figure 7.2. The measured fluorescence intensity is plotted as a function of the elution time. Experiments were performed at applied voltages between 100V and 300V in the 19nm devices and between 100V and 500V in the 70nm devices. Including the approximately 2 second variability caused by manual adjustment of the launching and driving voltages, variations in the elution times for each molecular length were observed on the order of 2%. The variations were caused by differences in the injection time and variability in the injection current.

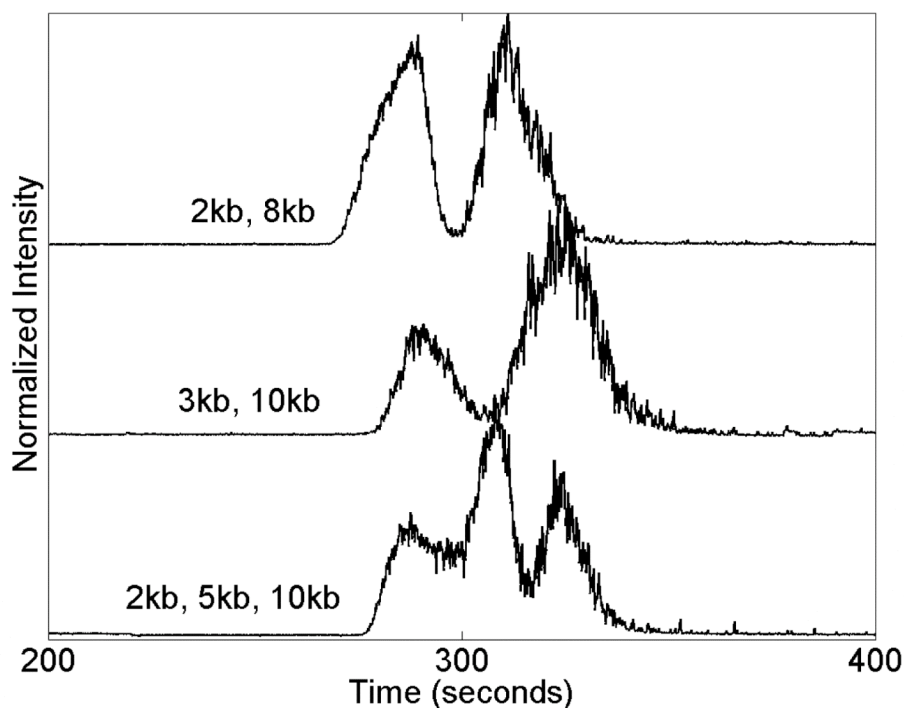


Figure 7.2: Examples of three electropherograms showing the separation of DNA mixtures in the 19nm deep separation channels. These experiments were performed using 100V applied between reservoirs 2 and 3.

Additionally, we performed experiments with 2kb and 10kb DNA molecules in the 70nm separation channels, collecting intensity data 3.5cm downstream from the injection point. Results are shown in Figure 7.3. For applied voltages of 100V to 500V, we observed no separation of the 2kb and 10kb DNA molecules. Note that for the 100V and 200V elution profiles, there are narrow spikes on the trailing side of the main peak. These spikes were caused by adhered clumps of DNA molecules moving through the detection region during the experiments. It is obvious from the videos that these bright DNA clumps are not the 2kb and 10kb DNA molecules of interest.

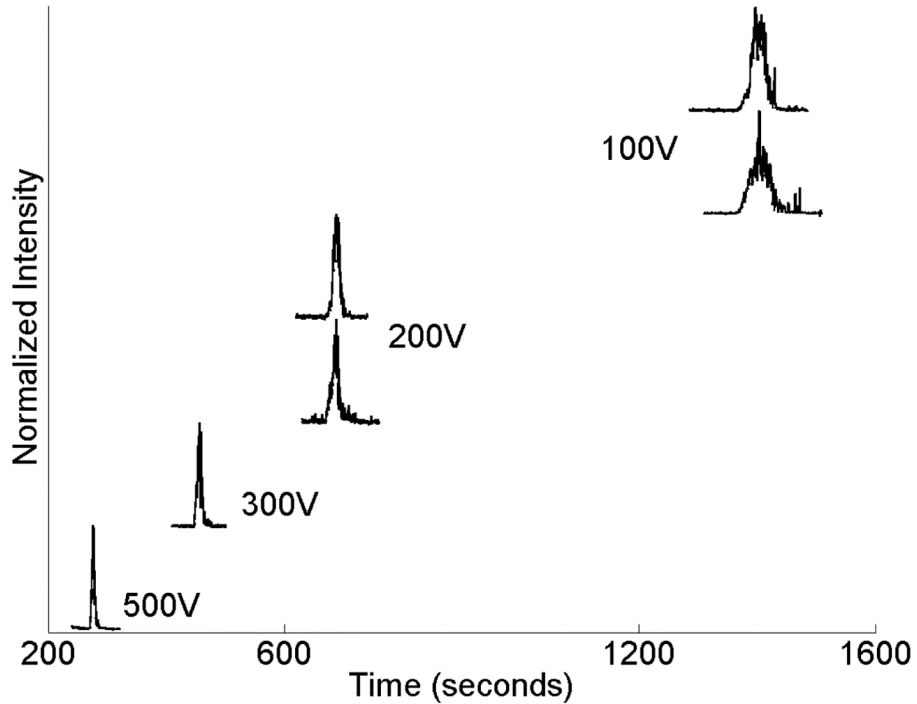


Figure 7.3: Electropherograms showing no separation of 2kb and 10kb DNA in 70nm deep channels. Other than the difference in the channel depth, experimental conditions are identical to those used in the 19nm deep channel experiments. The spikes apparent in the 100V data are from adhered clumps of DNA that happened to release during these experiments.

7.3 Nanoslit Theory

The relaxed, three-dimensional radii of the molecules used in these experiments are at least 117nm (for the 2kb molecule) based upon the standard Flory radius $R_{3D} = (\pi b w a^3 / 4)^{1/5} N^{3/5}$, where b is the polymer persistence length, w is the polymer width, a is the monomer size, N is the total number of monomers, and where we have used of the Onsager excluded volume to cast R_{3D} solely in terms of molecular dimensions [46, 90, 117]. In these experiments, the molecules are forced through nanochannels much thinner than the relaxed radius of the DNA.

Brochard has described the conformation of a polymer confined in two-dimensions based upon its relaxed, three-dimensional conformation [106]. When a polymer blob is confined in two-dimensions, the blob resizes itself into a pancake-like structure with a radius that scales as $R_{2D} \sim (N^3 a^5 / d)^{1/4}$. We assume that the pancake-like structure has a wall contact surface area density of Θ (number of contacts per unit area). The total number of contacts, C , for a pancake-like structure is then,

$$C = \Theta \pi R_{2D}^2 \sim \Theta (a^5 / d)^{1/2} N^{3/2}. \quad (7.1)$$

The fraction of the DNA molecule interacting with the surface is then

$$\alpha = C / N \sim \Theta (a^5 / d)^{1/2} N^{1/2}. \quad (7.2)$$

We use electrophoresis to drive molecules through the devices. There is an electrical driving force on each molecule $F_E = qNE$, where q is the electrical charge per molecule, and E is the applied electric field. The molecules are slowed by friction with the buffer $F_b = f_b v N$, where f_b is the buffer friction per basepair, and v is the molecular velocity. Additionally, there is surface friction $F_s = f_s v N \alpha$, where f_s is the surface friction per basepair. We note that electrophoretically driven molecules achieve terminal velocity nearly instantaneously to arrive at a molecular mobility of

$$\frac{\mu}{\mu_0} = \left(1 + \frac{f_s}{f_b} \alpha \right)^{-1}, \quad (7.3)$$

where the mobility is defined as $v = \mu E$, and the free solution mobility is the ratio $\mu_0 = q / f_b$ [127]. We use Equations 7.2 and 7.3 to write

$$\frac{\mu}{\mu_0} \sim \left(1 + \Phi \frac{N^{1/2}}{d^{1/2}} \right)^{-1}, \quad (7.4)$$

where $\Phi = (f_s / f_b) \Theta a^{5/2}$. The form of Equation 7.4 highlights that in confining nanochannels (small d), the DNA mobility scales as $N^{-1/2}$. Our experimental results indicate that this model works well for DNA molecules between 2kb and 10kb in 20nm thick channels.

We fit the observed DNA peaks with gaussian curves to determine the elution times. Because of the variability in the elution times for each molecular length, we standardized the elution times of all molecules using the average of the 10kb molecule elution times. For each experiment, the ratio of the individual 10kb elution time to the average of all 10kb elution times is calculated. This ratio is then used to adjust the times of the other molecules run concurrently. The ratio preserves the multiplicative scaling of the mobility with the elution time. The mobilities are then calculated from the standardized elution times, the migration distance, and the applied electric field. Error bars shown in Figure 7.4 are one standard deviation of the average molecular mobility.

We fit the mobility data for DNA in the 19nm channels using

$$\mu = \frac{\mu_0}{1 + AN^{1/2}}, \quad (7.5)$$

where both μ_0 and $A = \Phi / d^{1/2}$ are allowed to vary. Close agreement is seen between the data and the fit for the shorter molecules, and the overall shape of the theoretical curve is similar to the data (Figure 7.4). The free-solution mobility from the fit is $1.15 \times 10^{-4} \pm 0.07 \times 10^{-4}$ cm²/Vs and the parameter A is $2.4 \times 10^{-3} \pm 0.9 \times 10^{-3}$ (95% confidence for both). We measured the free solution mobility experimentally in the loading channels of our devices (650nm deep) to

be $1.06 \times 10^{-4} \pm 0.17 \times 10^{-4} \text{ cm}^2/\text{Vs}$ (using 8kb molecules, $N = 20$, 95% confidence), which is in agreement with the value obtained from the fit.

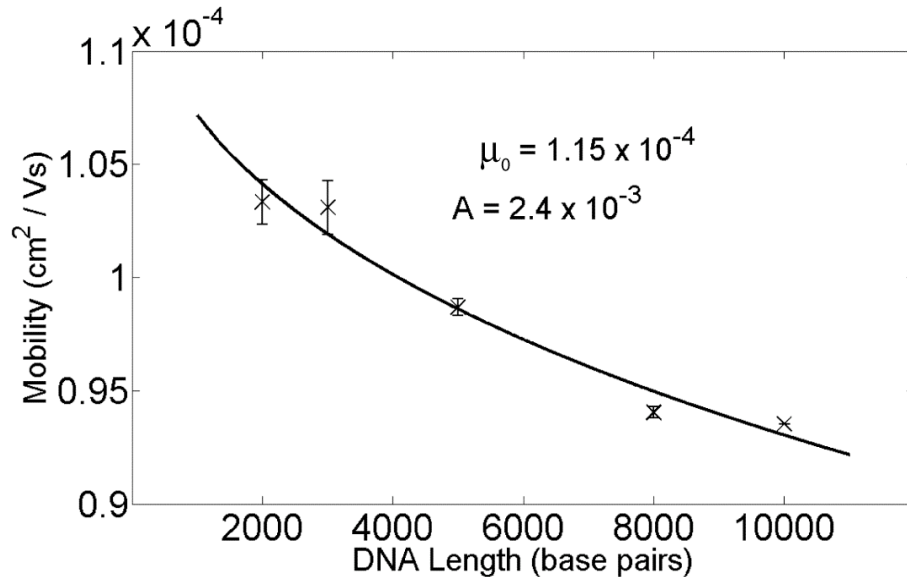


Figure 7.4: Experimental mobility data is plotted along with Equation 7.5. Error bars are one standard deviation.

7.4 Discussion

Let me start by noting that although the loading channels are larger than the radius of gyration of the 10kb molecule ($\sim 300\text{nm}$), some interaction between the molecules and the loading channel walls is possible. Thus, the measured free-solution mobility likely represents a lower bound on μ_0 . The fit parameter A contains information about the surface and buffer frictions (Φ). The mobility data indicate that, at some channel height between 19nm and 70nm, surface friction becomes sufficient to separate DNA molecules by length in channels about 2cm long. Using similar nanoscale devices with channel dimensions of 60nm, Fu *et al.* reported no separation for either double stranded DNA molecules (between 50bp and 766bp) or SDS-protein

complexes [63]. Thus, the onset of significant friction occurs for channel heights below 60nm for molecules less than about 10kb. There also seems to be a length-dependent aspect to the onset of measurable friction in nanoslits. Likely this length-dependence is related to the radius of gyration of the molecule and the overall nanoslit height. Molecules probably need to be significantly larger (as measured by the radius of gyration) than the slit height in order to have enough surface contacts to result in a measurable length-dependent mobility. A fruitful study would be to investigate the relationship between mobility, radius of gyration, and slit height.

Based upon the fit parameter A , one can estimate the ratio of the friction coefficients or the surface area contact density, Θ . From the fit, $A = 2.4 \times 10^{-3} = \Phi / d^{1/2}$. Using known values wherever possible, one then obtains $0.1552 = (f_s / f_b) \Theta$. Experimentally, it is possible to get a rough idea of the size of a particular DNA pancake. The DNA molecules are typically about 5 pixels in diameter, and for the Cascade 512B camera and the 100x objective, this means that a molecule is about $80\mu\text{m}$ across. The pancake surface is therefore about $1600\mu\text{m}^2$. If we let the friction ratio “vary”, then we can estimate the total number of surface contacts that a pancake structure has. At a friction ratio of unity (equal strength of surface friction and buffer friction), then there are approximately 250 surface contacts for the entire pancake (for a 10kb molecule). A ratio of 10 leads to about 25 contacts and a ratio of 100 yields 2.5 contacts.

To get a feel for the validity of the aforementioned contact values, let us turn our attention in another direction. Given a pancake diameter of $40\mu\text{m}$ and a slit height of 20nm, the volume of the entire pancake structure is $100\mu\text{m}^3$. For a 10kb molecule, this leads to a monomer density of 100bp per μm^3 . If the

“reaction” layer for a monomer to interact with the surface is 0.5nm (which is approximately the Debye layer for 5x TBE buffer), then the surface area basepair density is 0.05bp per μm^2 . Finally, this suggests that there are about 80bp that could interact with the surface for a 10kb pancake with a diameter of about 80 μm . This number is at least in the same order of magnitude as the previously derived value of 25 surface contacts, when I started by assuming that the surface friction is about ten times stronger than the buffer friction.

One might reasonably ask at this point, “How do I make the system perform better?”, “Can the nanoslit separate longer DNA?” I will take each question in turn. The system probably can be made to perform better by increasing the relative strength of the surface friction coefficient. Nominally, PVP acts to decrease surface friction and prevent sticking. Thus, the very coating that allows me to do the experiments (by preventing electroosmotic flow) actually serves to make the experiment less efficient. Lucky for me, then, that the experiment worked at all. Fortunately, there are other surface coatings that can be used. Though I have not used any of them (such as silane treatments with various functionalized end-groups, or other polymer coatings such as POP6), it is conceivable that one of them would increase the surface friction. One might take a linear polymer (such as acrylamide) and bind it to the surface using an attachment chemistry. Additionally, one might consider adding linear polymers to the buffer to act as a sieving matrix in conjunction with the surface friction separation observed in my experiments. Though the separation mechanism would be a complicated combination of sieving, entanglement (in the buffer due to the linear polymer), and surface effects (due to the nanoslit), the separation may be very efficient.

As written, the nanoslit separation theory does not suggest that altering

the channel dimensions will increase the separation effectiveness. However, from both my own work (see chapter 6), and from that of Fu *et al.*, it is known that the nanoslit height is important for determining the overall size of molecules that can be separated in a nanoslit. It is possible that the surface friction term actually depends upon the slit height. Even if the surface friction is independent of the slit height (as Brouchard's theory of DNA confined in two-dimensional slits would suggest), I would advise future experimenters to make thinner devices for separating shorter DNA molecules. For longer DNA molecules, slits in the range of 20-50nm should be tested (smaller slits will always run the risk of being clogged more readily, especially as the size of the DNA molecules increases). Furthermore, it is possible that Θ depends upon the relationship between radius of gyration and slit height. If Θ does depend upon the slit height and radius of gyration of the molecule, then the effect is probably most prominent for molecules with a radius of gyration approximately equal to the slit height. For particular lengths of DNA, one could conceivably optimize the separation process by tailoring Θ by using an appropriate slit height (based upon the results of the study hinted at in the previous sentence).

One of the most interesting applications that I envision for nanoslit separation devices is separating intact chromosomes. Owing to the simplicity of the device geometry and my own past experience with very long DNA molecules, the nanoslit devices seem to have a high likelihood of not succumbing to catastrophic clogging. Figure 7.5 shows the mobility of three size ranges of DNA, using Equation 7.5 and fit parameter values from the fit in Figure 7.4. Note that while the mobility begins to plateau for very long molecules, one is increasingly able to accept lower resolution as the

molecules get longer. That is, resolution of 0.1-1Mbps is sufficient for chromosomal DNA.

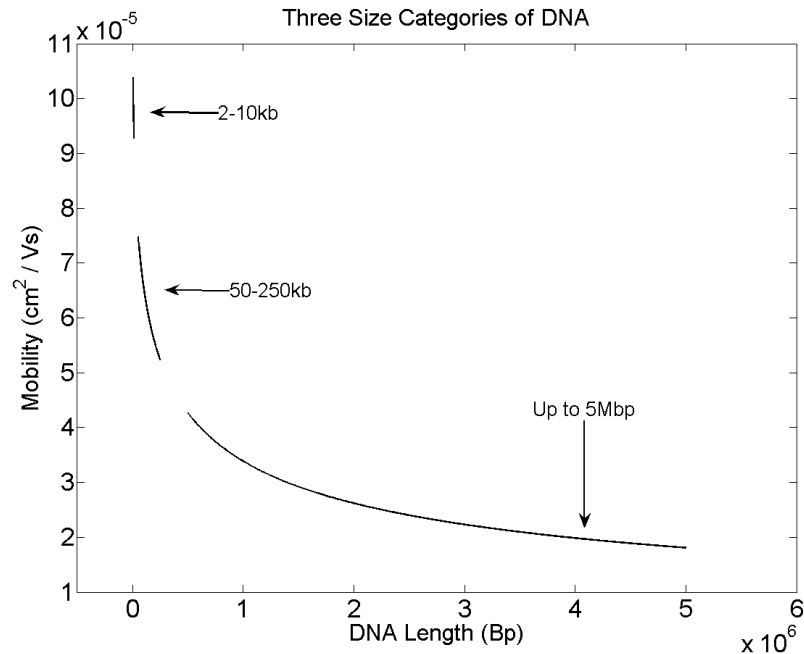


Figure 7.5: Mobility calculated using Equation 7.5 for DNA sizes up to 5Mbps. Note that the mobility begins to level off for very long DNA, though one does not typically require the same resolution for long DNA as for short DNA.

Elution times (Figure 7.6) are calculated from the DNA mobilities shown in Figure 7.5. Experimental conditions are assumed to be: 100V/cm, 3cm long separation length, and free solution mobility of $1.15 \times 10^{-4} \text{ cm}^2/\text{Vs}$. Even for DNA molecules longer than 1Mbps, the separation is expected to take only about 30 minutes. This is in contrast to traditional techniques (pulsed field electrophoresis) which require 12-48 hours.

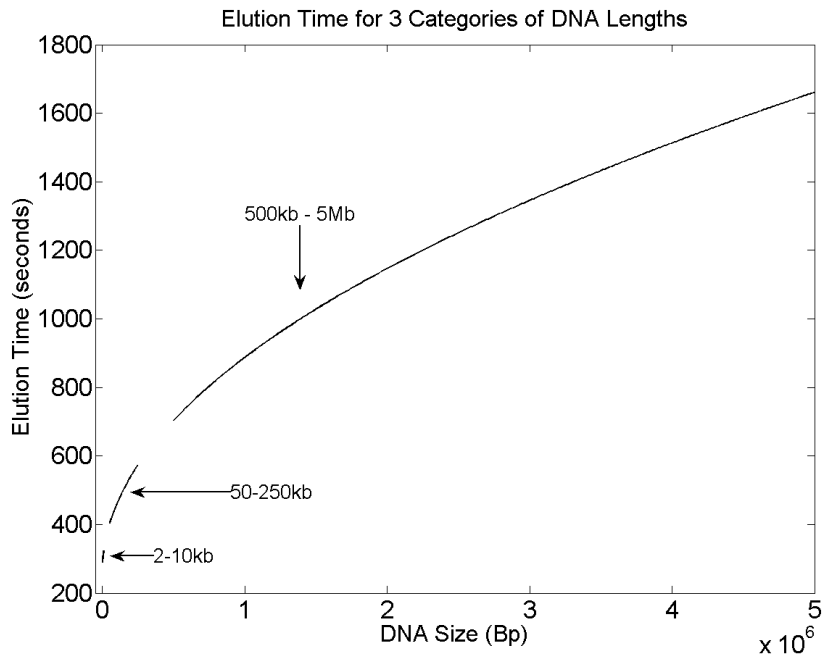


Figure 7.6: Elution times for DNA molecules in nanoslit devices calculated using the mobility values from Figure 7.5 and an electric field of 100V/cm, a separation distance of 3cm, and a free solution mobility of $1.15 \times 10^{-4} \text{ cm}^2/\text{Vs}$. Note that even for 5Mbps DNA (a typical chromosome length), the separation only takes 26 minutes.

While Figure 7.6 suggests that separating chromosomal DNA molecules is possible, one important question is, “Is the resolution sufficient?” To answer this question, I calculated the diffusion coefficient for DNA in the nanoslit devices based upon the full width at half of the maximum intensity value for a typical separation experiment (taken from the set of 2kb through 10kb data described above). Based upon the Gaussian fits of the elution peaks, and an assumption that all of the dispersion in the peaks results from diffusional band broadening (an assumption that necessarily yields a diffusion coefficient that is too large), one arrives at a diffusion coefficient for DNA in the nanoslits of $3.9 \times 10^{-7} \text{ cm}^2/\text{s}$. Note that this value is much larger than that reported by others [128]. The difference is likely due to the fact that I have

assumed all of the dispersion is diffusional, whereas a significant amount of it is due to the injected plug width. I am not too concerned with this discrepancy, as the large diffusion constant should ensure that we have an estimate of the worst resolution of our devices (that is, actual experiments should yield even better results than those estimated herein). A final note about my estimate of the diffusion coefficient is that normally the diffusion coefficient is size dependent. In the calculation that follows, I use the same diffusion coefficient for each DNA size. Typically, the diffusion coefficient gets smaller as molecule size gets larger. Thus, the already overestimated diffusion coefficient becomes an even greater overestimate as the molecule size being considered increases. Again, this error is fine because it adds conservatism to the prediction from the calculation.

From the diffusion coefficient of DNA in the nanoslits and the mobility theory (Equation 7.5), I estimated the elution time and resolution of the three chromosomes of *S. pombe* yeast DNA. These molecules are considered because they happen to be the molecules that I originally used when I began my nanofluidic research. Results for a hypothetical experiment with *S. pombe* chromosomes in a nanoslit are shown in Figure 7.7. The three chromosomes have sizes of 3.5Mbps, 4.6Mbps, and 5.7Mbps. Expected elution times are plotted and the error bars represent the band width based upon the elution time and the diffusion constant (as estimated above). Note that the hypothetical data in the figure suggest that these chromosomes could easily be separated in about 30 minutes with suitable resolution. Again, the estimates leading to the elution times and band widths should be conservative in nature – one might be able to perform the separation faster or with better resolution.

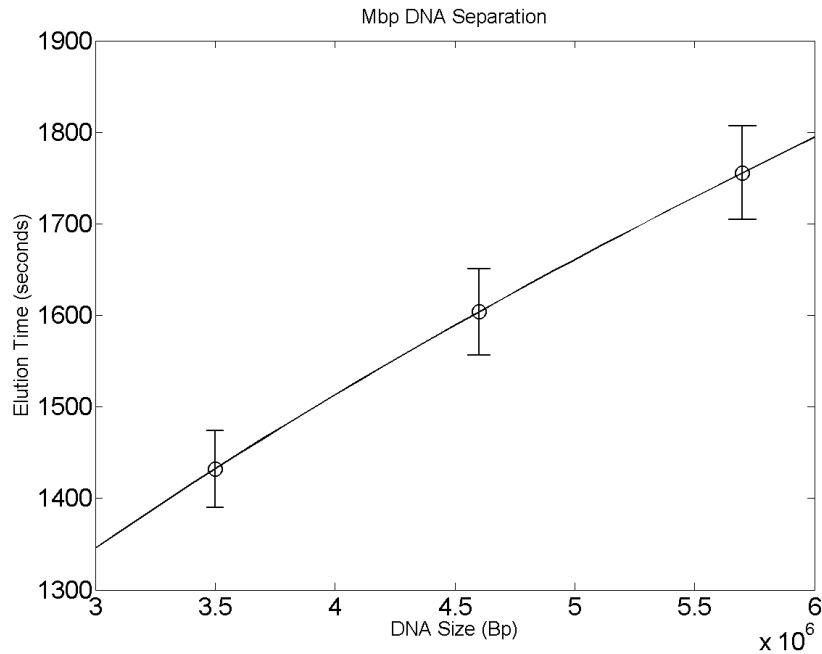


Figure 7.7: Results for a hypothetical separation experiment involving *S. pombe* chromosomal DNA in nanoslits. Experimental parameters are taken from Figure 7.4 and the elution times are based upon the mobilities of these molecules as determined using Equation 7.5. Error bars represent diffusional (only) band broadening and suggest that these three chromosomes could be separated and resolved in less than 30 minutes.

A few more comments on the nanoslit experiments are in order before moving on. I should note that while others [126] have used PVP as a sieving matrix, it seems unlikely that the inclusion of PVP in the buffer used herein is responsible for the observed length-dependent mobility. This conclusion is based upon the observed DNA separation in the 19nm channels but not the 70nm channels. Furthermore, in those experiments in which PVP was used as a sieving matrix, the molecular weight of the PVP was over 100 times greater than the form of PVP used in these experiments [126]. Additionally, others have used PVP in DNA separation experiments and reported no sieving

effects attributable to the PVP [8]. Because PVP is polar, it is also likely that the PVP molecules lie down flat upon the channel walls.

I have presented a theoretical model that accurately describes DNA size-dependent mobility from 2kb to 10kb when driven through nanochannels with dimensions of approximately 20nm. I have performed experiments in devices with 70nm deep nanochannels and observed no resolvable mobility differences for 2kb and 10kb molecules. The data highlight that free-solution electrophoresis is not possible for molecules with globular dimensions much larger than the small dimension of a nanochannel. These results are notable given the ever-increasing number of experiments being performed using biomolecules in nanofluidic devices with dimensions comparable to or smaller than the sizes of the molecules. Finally, I note a number of ways in which the nanoslits might be modified to enhance their performance or extend their utility. A hypothetical separation experiment is presented that suggests that *S. pombe* chromosomes could be separated in a nanoslit device in about 30 minutes.

CHAPTER 8

ENTROPIC TRAPS

8.1 Introduction

As mentioned in chapter 2.7.3, entropic traps were described in [47-55] and have been used to separate long DNA molecules by size [25, 57, 58, 105]. Entropic traps are essentially nanometer-scale constrictions in an otherwise larger fluidic channel. If you imagine taking a microchannel and placing an approximately 50nm constriction in the middle of it that is about 10-20 μ m long, then you have an entropic barrier. If you now put a few thousand of these barriers in a row, you have what is referred to as an entropic trap array. This is essentially the nanoslit device of chapter 7 with the nanoslit portion of the device periodically punctuated by deep regions (alternatively, one thinks of the entropic trap array as a microchannel periodically punctuated by constrictions).

As will be described below in some detail, the geometry of a narrow restriction in an otherwise “large” channel is called an entropic barrier or trap because the restriction delimits a region of high entropy (the deep region) from a region of low entropy (the restriction or shallow region). Like the nanoslit geometry, one of the very elegant aspects of the entropic trap (array) is that the essential function of the device can be described with relatively simple equations. The experiments required to test the theoretical model are straightforward to perform. Not only is there a practical application (polymer separation), but one also learns something about polymers in confined environments in the process.

8.2 Entropic Trapping

Before going into the fabrication and describing the experiments conducted using entropic trap devices, I will begin by describing what the devices are and then present the theory of polymer movement through these structures. To take advantage of the conformational entropy of polymers in solution, small volumes are juxtaposed with large volumes. In microfluidic environments, the small volumes are typically nanometer-scale, quasi-two-dimensional slits or square-cross-sectional channels with dimensions of less than 100nm^2 . These small volumes are usually short in the direction along which the polymers are forced to move.

Figure 8.1 shows schematics of two devices that could be used to take advantage of the small-large volume juxtaposition for entropy-based experiments. The upper panel of Figure 8.1 shows an entropic trap array and molecules therein. The entropic trap array is discussed more below. The lower schematic shown in Figure 8.1 is alternatively referred to as a nanochannel, nanopore, or very small channel, and has been described extensively in [44-46, 93, 103, 104, 124]. Applications of devices with this geometry include: separating DNA by length using “entropic recoil”, elongating DNA for gene mapping, and studying the physical properties of polymers confined within highly restrictive geometries as well as the frictional interactions between the polymers and device walls.

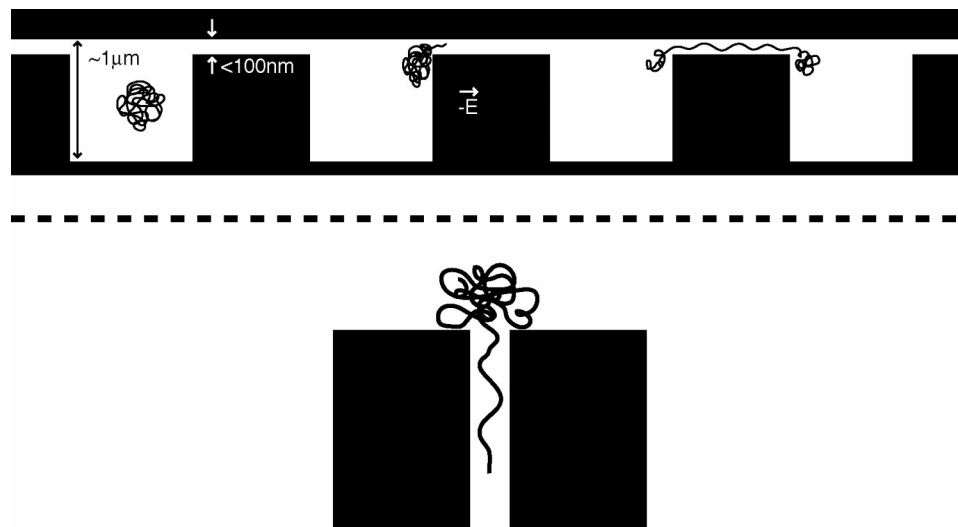


Figure 8.1: Two schematic diagrams showing devices used to manipulate or separate polymers based upon entropic differences in adjacent volumes. The top panel shows a side-view of multiple entropic traps, an entropic trap array. The deep regions are typically $\sim 1\text{mm}$ deep, while the shallow regions are $<100\text{nm}$. Typically, an electric field is used to drive molecules through the restriction, and since DNA or SDS-clad proteins are negatively charged, they move in the opposite direction as the electric field direction. Polymers must overcome a significant energy barrier to move into and then through the shallow region. The molecules spend more time in the deep regions, where their (conformational) free energy is maximized. Thus, the oscillating pattern of deep and shallow regions constitutes a series of traps (energy wells) for polymers. The lower panel shows a polymer at the interface between an open region and a narrow channel. The polymer can be driven into the channel, which may be on the order of $30\text{nm} \times 30\text{nm}$, where its relaxed state is a near-linear strand. If the molecule is left to straddle the boundary, it will recoil from the constricting region.

The upper schematic in Figure 8.1 shows an oscillating pattern of deep and shallow volumes. This geometry has been dubbed the entropic trap array; a single set of shallow-deep-shallow volumes constitutes a single entropic trap. In the simplest elaboration of the theory for how polymers move through entropic traps, frictional interactions between the polymers and the device walls are ignored. Only the change in entropy (accessible microstates) from the deep region to the shallow region, and the associated change in the free

energy of the polymer, is considered. I shall briefly restate the theory of entropic trapping below.

The entropy of the polymer scales directly with the length of the polymer [93]

$$S \propto N, \quad (8.1)$$

where N is the total number of monomers in the polymer. The decrease in entropy from the deep to the shallow region is directly proportional to the distance into the shallow region the polymer is extended [93, 129]

$$S \propto x, \quad (8.2)$$

where x is the coordinate axis along which the molecule extends into the shallow region (the left-right direction in the upper panel of Figure 8.1; the top-bottom direction in the lower panel).

The polymer is driven electrophoretically, so along the direction of the field there is an associated electric energy equal to

$$E_{Electric} = \int_{x=edge}^x dx \cdot qEx = qEx^2, \quad (8.3)$$

where I have written the total polymer charge as q , and have (in the final step) set the edge of the trap at $x = 0$.

Assuming that we only care about what happens at the trap edge (the interesting place), the free energy change associated with moving along the x -direction is then

$$\Delta F \propto Tx - qEx^2, \quad (8.4)$$

where I have explicitly included the temperature, T , so as to make it clear that the entropy term (the one with the T) acts in the opposite direction as the electric field term. The probability of passage is then given by the Boltzmann factor

$$p = \exp\left(\frac{\Delta F}{kT}\right) = \exp\left(\frac{Tx - qEx^2}{kT}\right). \quad (8.5)$$

Note that Equation 8.5 is the probability that a single “attempt” to pass through the restriction succeeds. An attempt to pass through the restriction consists of a tendril of polymer probing a distance x into the restriction. For small x , the electrical energy is not sufficient to overcome the entropic penalty and the probing attempt fails. If the molecule is “trying” to get through the restriction some number of times per second, then the probability of passage per second is written as

$$P = w \exp\left(\frac{Tx - qEx^2}{kT}\right), \quad (8.6)$$

where w represents attempt frequency. Perhaps the most remarkable aspect of the theory is that the probability of a single escape attempt is not dependent upon any aspect of the molecule size (Equation 8.5).

Even though all polymers have the same chance of success of moving through the restriction once they begin to probe it, length-dependent discrimination is possible using entropic traps because polymers of different sizes (or stiffness) make different numbers of attempts per unit time. The interfacial contact area between the polymer and the opening of the restriction determines the frequency of attempts that a polymer makes when pressed against the restriction. Larger polymers have larger spherical dimensions and this translates into higher frequencies of attempts. Note that the attempts themselves are essentially random in nature, being the result of thermal agitation of the polymer. Figure 8.2 shows a schematic of the different contact areas between two polymers and a restriction. Note that this is a top-down view of the same structure shown in the top panel of Figure 8.1.

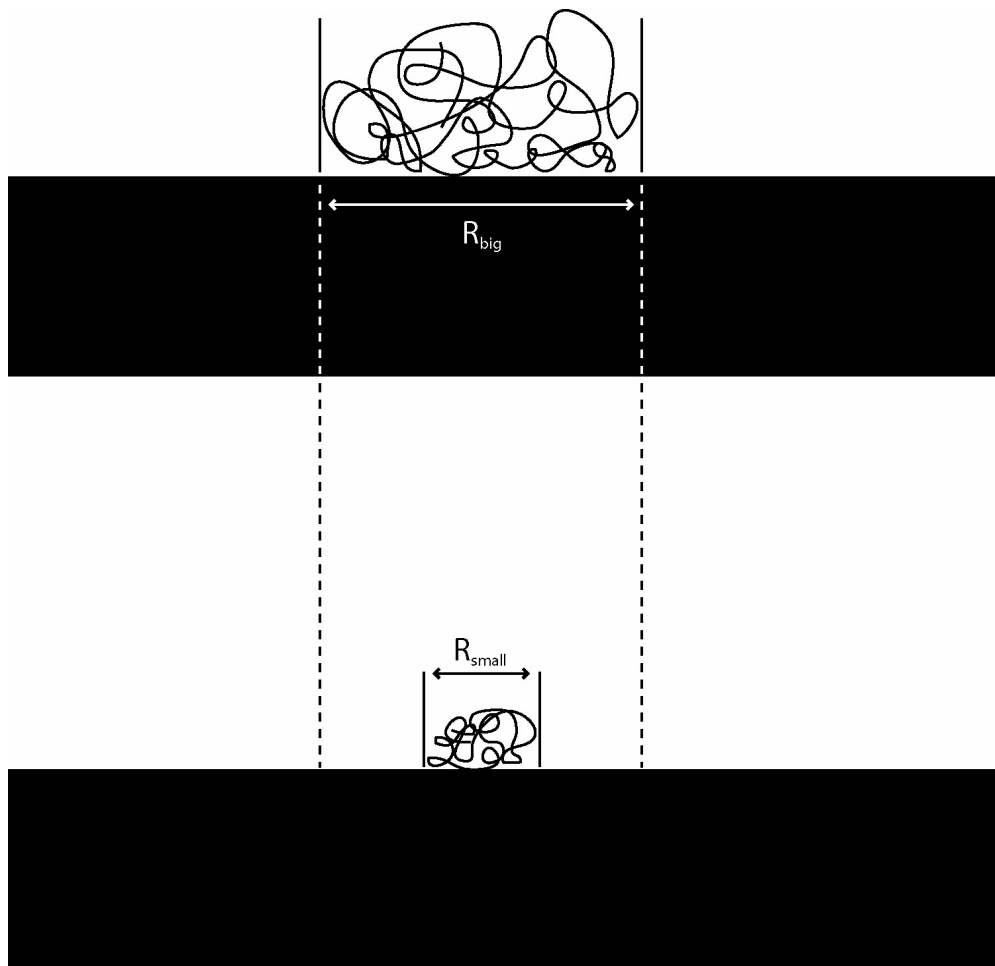


Figure 8.2: A top-down schematic showing a big and small polymer pressed against restrictions (shown as black rectangles). The bigger molecule, with its associated bigger radius, makes more interfacial contact with the barrier and is therefore able to make more randomly-initiated probing attempts.

The frequency of escape attempts, w , is given in one of Han's original papers on entropic trapping [57]

$$w \propto R d_s, \quad (8.7)$$

where R is the radius (or diameter) of the molecule and d_s is the depth of the shallow region (the restriction). The right-side of Equation 8.7 is the contact area. Equation 8.7 can be substituted into Equation 8.6 to give the probability

of passage per second, or inverted to give the average time a molecule spends pressed against the trap before it escapes, the trapping time,

$$\tau = \tau_0 \exp\left(-\frac{\Delta F}{kT}\right), \quad (8.8)$$

where $\tau_0 = 1/w$. Equation 8.8 contains the essence of entropic trapping as a means of manipulating or separating molecules: τ_0 contains all of the “information” related to the polymer, while ΔF describes the energy barrier.

If polymers are driven through a series of entropic traps with an electric field, then one can write the mobilities of the polymers as

$$\frac{\mu}{\mu_0} = \frac{1}{1 + \tau/t_{period}}, \quad (8.9)$$

where t_{period} is the time that it would take a polymer to move the distance of one deep and shallow region (one period of the array) if no delay at the trap occurs. The form of Equation 8.9 highlights that in an entropic trap array: polymers always move slower (or possibly at the same speed) than they would if they were in an open channel; that if $t_{period} \gg \tau$ then the polymers move at their “normal” mobility (the electrical energy overwhelms the entropic penalty); and that if $\tau \gg t_{period}$ then the polymers take a very long time to move through the array (the slowness of overall motion overwhelms the delay caused by a trap, or the delay caused by the trap is such that the molecule never escapes).

Because polymer properties like the length or persistence length are “contained” in the factor τ_0 (Equation 8.8), and because one has a relatively straightforward means of measuring τ (it is a time after all, something that can be measured with a stopwatch or by tapping one’s foot), one can use entropic barriers to learn about what is being forced to move across them. The most readily accessible information (given most of the experimental setups available within the Craighead group) is fluorescence intensity information. We can look

at the traps and measure the arrival and departure of individual molecules or the buildup of many molecules over time (see, for example, [130]).

To quantify the buildup of many molecules at an entropic barrier, I assume that the measured fluorescence intensity is linearly proportional to the number of molecules, $I \propto N$. This assumption is valid for linearly-responsive photodetectors. One must avoid saturating the detector. For this discussion, saturation means that the fluorescence intensity from the molecules has reached the maximum dynamic range of the detector and that even if more molecules appear within the viewing area of the detector, no extra intensity gain will be measured. Experiments conducted by driving molecules at various electric fields against barriers of various thicknesses are described quantitatively as follows.

There is an arrival rate of molecules probing at the trap, \dot{N}_t , which is given by

$$\dot{N}_t = \dot{N}_i - \dot{N}_o, \quad (8.9)$$

where \dot{N}_i is the rate of incoming molecules and \dot{N}_o is the rate of outgoing molecules. $\dot{N}_i = \Phi = \lambda v$, where Φ is the rate of incoming molecules (#/s) as described by the quantity λv , where λ is the linear number density of molecules (#/cm) and v is the velocity of the molecules (cm/s). $\dot{N}_o = N_t P$, where N_t is the number of molecules probing the trap, and P is the probability of passage through the trap (Equation 8.6). Substituting the known incoming and outgoing rates yields

$$\dot{N}_t = \Phi - N_t P \rightarrow \dot{N}_t + N_t P - \Phi = 0, \quad (8.10)$$

which is an inhomogeneous, first-order differential equation giving the number of molecules at the trap as a function of time. Equation 8.10 is solved by finding both a particular and homogeneous solution and the result is

$$N_i(t) = \frac{\Phi}{P} + \left(N_o - \frac{\Phi}{P} \right) \exp(-Pt), \quad (8.11)$$

for the initial condition $N_i(t=0) = N_o$. Note that this initial condition is often the case experimentally; initially, there are molecules on the downstream side of the entropic barrier. In the special case where $N_o(t=0) = 0$, the N_o term is equal to 0 in Equation 8.11 and the result is the same as if the initial condition had originally been $N_i(0) = 0$.

Equation 8.11 is used extensively throughout the remainder of this chapter. The preceding discussion of the theory of entropic trapping was a reformulation of ideas presented by Jongyoon Han and others (such as Gary Slater and his various teams of researchers) in earlier experimental and theoretical works on entropic trapping (see, for example, [57, 59]. Over the years, Kevan Samiee and I have had many discussions on the subject, and most of the above presentation was tailored around the common framework that he and I built to understand the theory and the utility of the theory in designing experiments. I'll now describe one of those experiments, which has led to other, ongoing experiments.

8.3 Applications

In the most recent experiments that I have performed using entropic trap devices, the primary goal is to determine if ssDNA can be trapped at barriers. Assuming ssDNA can be trapped, the goal becomes to develop a protocol capable of discriminating between double- and single-stranded DNA at a barrier or in an array. These two goals motivate the experiments. The application of trapping ssDNA and separating ssDNA molecules from dsDNA molecules is a chip-based version of temperature gradient gel electrophoresis (TGGE).

In TGGE, DNA is driven across a gel (as in standard gel electrophoresis) while the temperature of the gel environment is increased. DNA molecules denature at different temperatures based upon their base composition (sequence). During denaturation, two single-stranded segments attached by a segment of still double-stranded DNA migrate through the gel (somewhat, but not exactly, similar to the ssDNA hairpin shown in Figure 3.2). The 'Y' shape of the partially denatured fragment migrates more slowly than does DNA that has not yet begun to denature. Thus, sequence-dependent mobility is possible. That is, two molecules of the same length but with different sequences can be separated based upon their denaturation temperatures.

I expect to be able to perform similar experiments using entropic barriers or entropic trap arrays. The factor w appearing in Equation 8.6 (or τ_0 appearing in Equation 8.8) depends upon not only the overall probing area, but also the stiffness of the polymer. Thus, it should be possible to discriminate between polymers of sufficiently different rigidity even if they are the same length. This is indeed the scenario one finds when comparing single- and double-stranded DNA. Single-stranded DNA has a persistence length of approximately 3nm, while double-stranded DNA has a persistence length of approximately 50nm. The two molecules have very dissimilar stiffness. The interfacial contact area of single- and double-stranded DNA will be very different and the molecules will remain stuck at each barrier with different trapping times. In the most straightforward interpretation of the theory, the smaller persistence length of ssDNA leads to a smaller radius of gyration for ssDNA of similar length to dsDNA, so the ssDNA should make less probing attempts. This should lead to longer trapping times for ssDNA.

The straightforward (or perhaps, naïve) interpretation of the interfacial contact area differences between ssDNA and dsDNA depends upon both molecules being trapped and interacting with the gap in essentially the same way. It is conceivable that most ssDNA molecules will have so small a radius of gyration that no trapping at all will occur. Experiments described below confirm the ability to trap ssDNA with very thin barriers. It is also possible that the nature of the probing is different for ssDNA and dsDNA. Namely, it is possible that due to its increased flexibility, ssDNA is actually capable of making more probing attempts even though it has a smaller radius. That is, the increased flexibility of ssDNA might lead to a greater “probing density per surface area” which would appear in Equation 8.7 as a different proportionality constant than the constant appearing for dsDNA. This last possibility is currently being investigated theoretically by Elizabeth Strychalski and will come to bear on future experiments. The as yet incomplete analysis is not included or considered herein.

8.4 Experiments

Experiments are performed using the same experimental setup described in previous chapters (see for instance, chapters 6 and 7). Loading channels are 650nm deep, while the restrictions (entropic barriers) are 25nm deep. Images of the devices are shown in Figure 8.3. DNA is driven through the fluidic channels using electric fields as described in previous chapters. Experiments are generally performed by driving DNA molecules directly from the loading reservoir to the channel containing the entropic barrier(s). Directly driving DNA from the reservoir across the barrier is a convenient method for determining if short DNA molecules (described below) can effectively be

trapped. Also, as single-stranded DNA molecules have never been tested with entropic barriers, driving these molecules directly across the trap is necessary in order to evaluate the possibility of being able to trap these molecules at all. As the protocol is further refined (in future work), experiments will shift from this direct and continuous drive method, to the more conventional method of gathering a plug of DNA at the entrance to the separation channel, driving off excess DNA, and then launching the plug into the separation region.

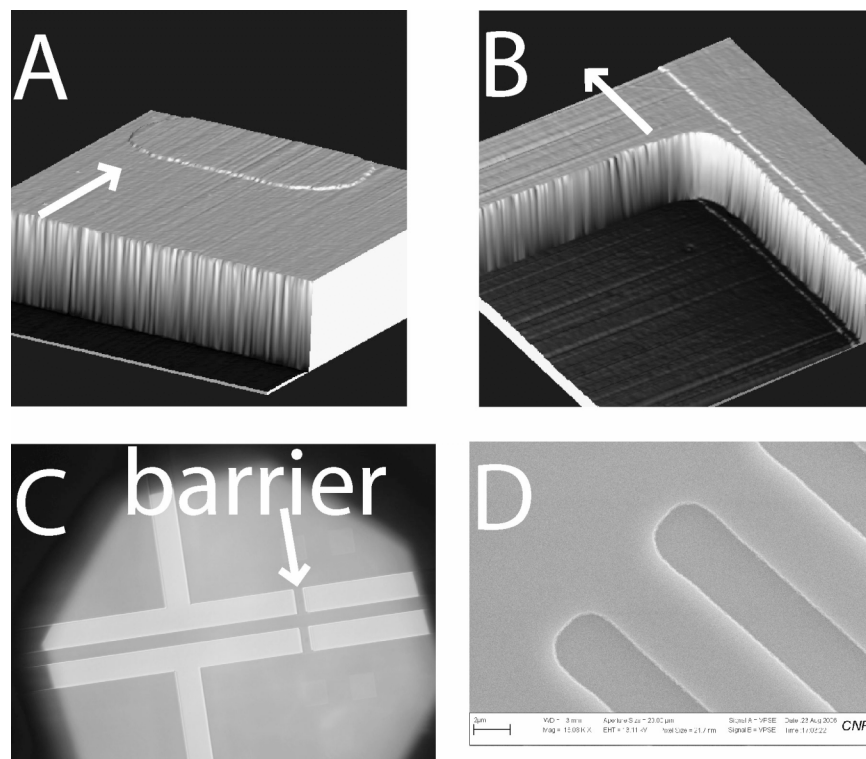


Figure 8.3: Images of entropic barriers. A) and B) Atomic force microscope images, rendered in three-dimensions with texturing. The arrows indicate the direction DNA molecules are driven against and across the barrier. In A, the oval-shaped structure at the upper-right edge is a support pillar in the middle of the barrier. In B, the edge that runs from the lower-right edge to the upper-left edge in the direction of the arrow is the edge of the fluidic channel. In both A and B, the large cliff-like structure at the base of the arrows is the edge of the entropic barrier. C) An optical image of two isolated microchannels that each contain an entropic barrier. D) A scanning electron micrograph showing three consecutive deep regions in an entropic trap array.

The DNA samples used in these experiments were provided by Dr. Stephane Corgie of the Walker research group. The molecules are 325 or 450bases or base pairs in length (both single- and double-stranded DNA were provided). The DNA molecules are species-specific segments of DNA that can be PCR amplified and provide unique genetic signatures of the microbes from which the molecules originated. Thus, the molecules are useful as biomarkers for microbial species. The molecules are end-labeled with AlexaFluor 488.

An example of an experiment is shown in Figure 8.4. There are a number of ways to quantify the data presented in Figure 8.4. Those that I have employed all involve computing a sum of the pixel intensity over a given region of the image. A thin rectangle just at the edge of the barrier is typically chosen as a measure of the number of molecules at the trap (recall the assumption that the intensity is proportional to the number of molecules at the barrier). An example of the resulting data is shown in Figure 8.5.

Once intensity versus time data are collected as in Figure 8.5, Equation 8.11 is used to fit the maxima. A three-parameter fit is employed, with Φ , P , and N_o allowed to vary. As mentioned previously, N_o is almost never zero to start, and this is evident in Figure 8.4 by the non-zero intensity when the experiment begins at $t=0$. The parameter N_o does little more than establish the $t=0$ point. $\Phi = \lambda v$ governs the maximum (the plateau), assuming that saturation does not occur, and sets the rapidity of attaining that plateau. P also dictates the speed at which saturation occurs. More importantly, P contains explicit information about the molecules caught at the barrier. Sample graphs showing the variability of N_t with respect to Φ and P are presented (Figures 8.6 and 8.7). Obtaining P by fitting data like those of Figure 8.5 is a means of

measuring the stiffness or length of the molecules at the barrier. This is the information obtained in the following experiments.

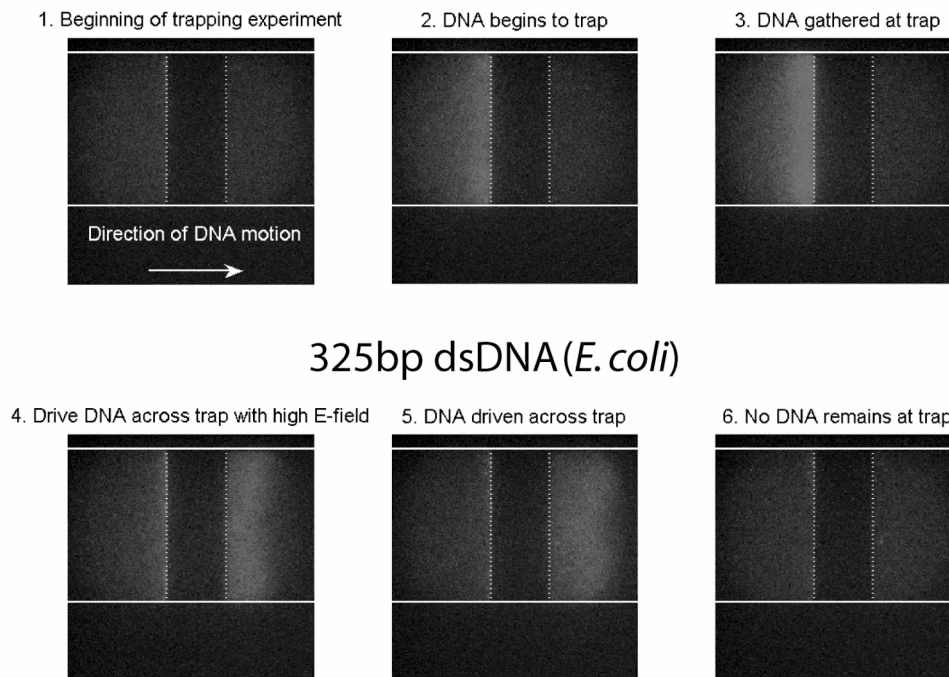


Figure 8.4: A collage of images showing the gathering of dsDNA at an entropic barrier. The barrier is outlined by the vertical, dotted lines; the horizontal, solid lines outline the fluidic channel. The DNA is a 325bp fragment from *E. coli*, end-labeled with AlexaFluor 488. DNA is driven directly across the barrier at 5V. In panel 1, the experiment is just beginning and the intensities on either side of the barrier are equal. In panel 2, the DNA is beginning to gather appreciably at the barrier. In panel 3, a significant amount of DNA has gathered at the barrier. Note that DNA continues to move across the barrier during the build-up process as evidenced by the fluorescence persistent on the right side of the barrier. In panels 4 and 5, DNA is driven across the barrier (“flushed”) by applying 100V across the barrier. Finally, panel 6 shows complete flushing of the barrier (compare panel 6 to panel 1).

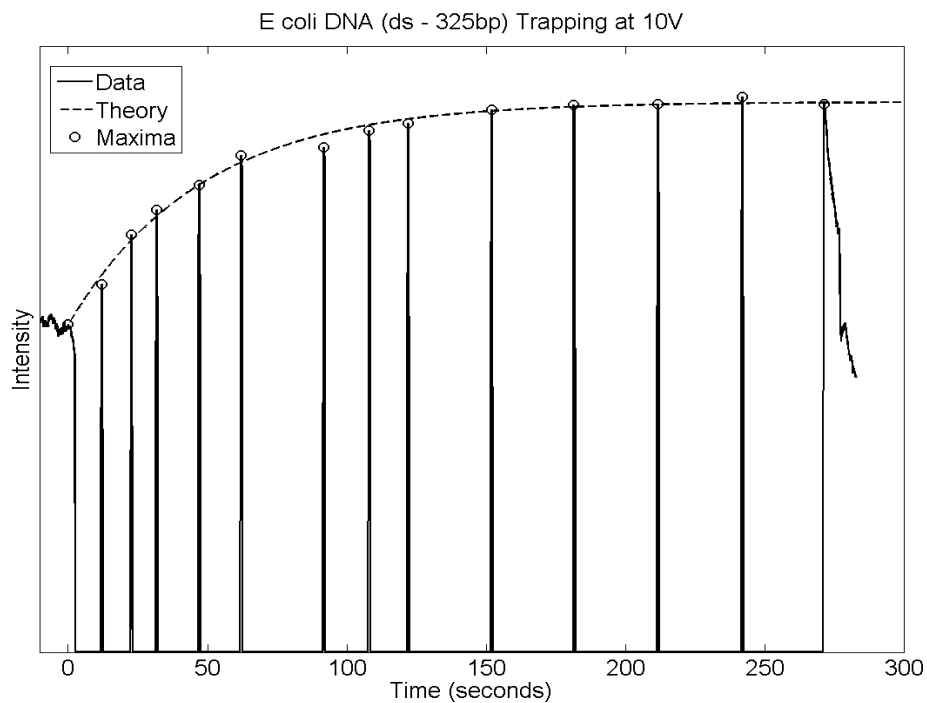


Figure 8.5: Intensity versus time data for 325bp *E. coli* DNA gathering at a 25nm entropic barrier. The DNA molecules are driven at 10V across the trap. The plateau represents the amount of DNA necessary to essentially guarantee that one molecule is always escaping. A shutter is used to prevent photobleaching, which is why the data appear as sharp spikes (as opposed to continuous intensity data). Maxima are found using a MATLAB search algorithm.

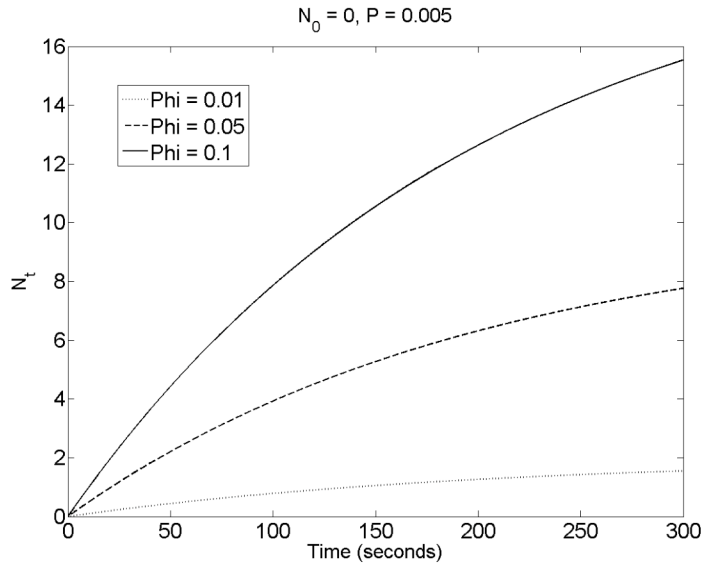


Figure 8.6: N_t as a function of time for multiple Φ (Equation 8.11). Note that I chose the proportionality constant between N_t and I such that y-axis values can be roughly interpreted to be real numbers of DNA molecules. Φ values are chosen across the range of experimentally measured values. The initial condition is $N_0 = 0$, and the parameter P is 0.005.

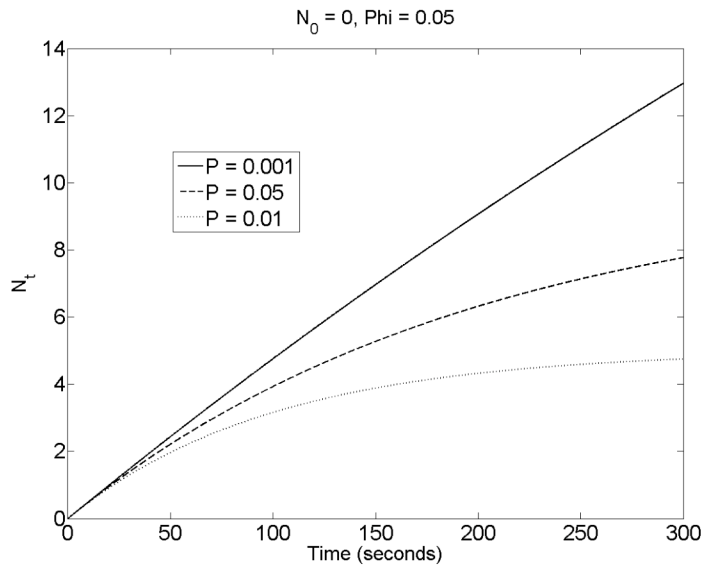


Figure 8.7: N_t as a function of time for multiple P . Again, it should be pointed out that an arbitrary scaling parameter between N_t and I is chosen such that the y-axis can be roughly interpreted as the number of real DNA molecules at the barrier. P values are chosen across the range of experimentally measured values. The initial condition is $N_0 = 0$, and the parameter Φ is 0.05.

The important fit parameter is P . If all experimental parameters are held constant except for the length of the DNA used (or the flexibility of the DNA used), then it is possible to compare DNA lengths in different experiments by comparing different P values. Going back to Equations 8.6 and 8.7, we see that

$$\frac{P_1}{P_2} = \frac{w_1 \exp(\Delta F / kT)}{w_2 \exp(\Delta F / kT)} = \frac{w_1}{w_2} = \frac{CR_1 d_s}{CR_2 d_s} = \frac{R_1}{R_2}, \quad (8.12)$$

where the subscripts refer to two different types of molecules, and where the proportionality constant in Equation 8.6 has been called C . Note that the proportionality constant C is interpreted as the surface area probing density. The ratio of R -values on the right of Equation 8.12 should be interpreted more broadly than the ratio of the radii of the two molecules. The R -value ratio is the ratio of the number of probing tendrils of each molecule. One could imagine comparing a single-stranded DNA molecule to a double-stranded DNA molecule using Equation 8.12, and while the form of the ratio would be different (you would have to consider the persistence length), the equation accommodates such a comparison through different C s.

I performed experiments to test the ability of 25nm barriers to trap ssDNA and to compare the trapping characteristics for ssDNA and dsDNA. For single- and double-stranded DNA comparisons, the following set of molecules was used: 325bp, 325b, and 450b DNA molecules from *E. coli*. This set offers a nice means of comparing both single and double stranded DNA of the same length as well as comparing slight differences in the length. Figure 8.8 shows the measured intensity as a function of time for the 325b and 325bp molecules at the entropic barrier. Note that the 325bp molecule appears to reach its plateau much slower than does the 325b molecule. This suggests

that the 325b molecule is more strongly trapped than the 325bp molecule. That is, 325bp DNA escape more rapidly and thus “saturate” the trap (plateau) more slowly than do the 325b DNA molecules.

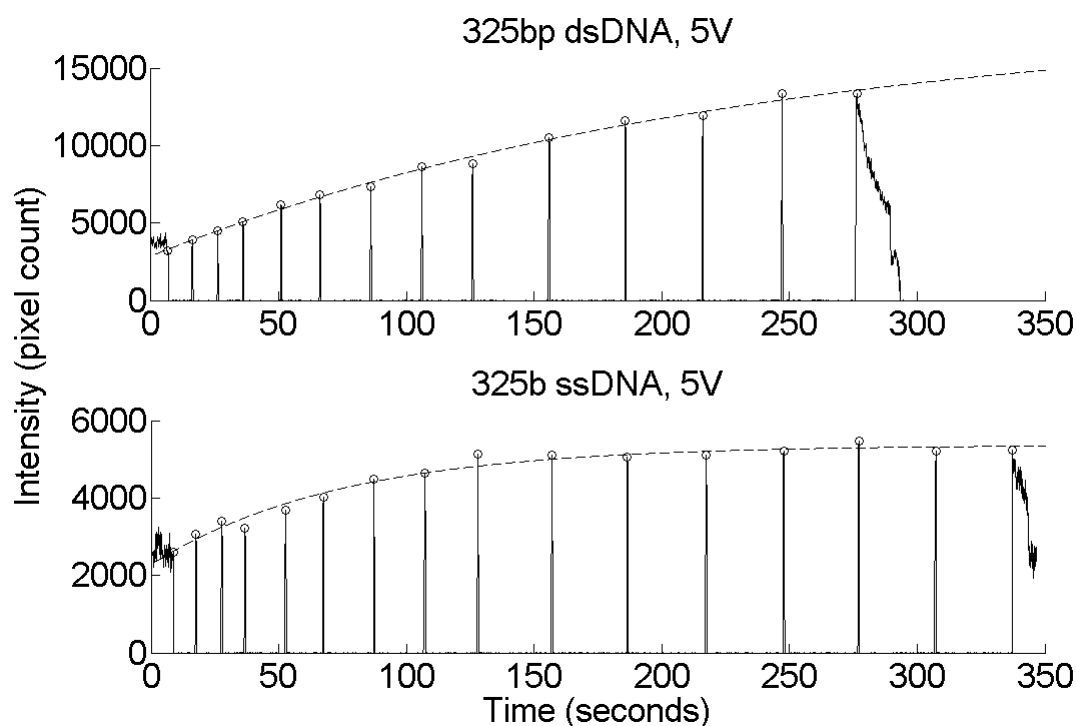


Figure 8.8: A comparison of the intensity of DNA accumulated over time at an entropic barrier. DNA are driven towards and across the barrier with a 5V potential. The upper graph shows the results for 325bp dsDNA and the bottom graph shows the results for the same length of ssDNA. The ‘o’ symbols mark the points to which Equation 8.11 is fit. The dashed line is the fit. Note the qualitatively different shapes in the curves. The dsDNA curve does not appear to plateau after approximately 5 minutes, while the ssDNA curve has neared its plateau after about 3 minutes. This indicates that dsDNA escape more readily than do ssDNA, as confirmed quantitatively by considering the probing frequencies presented in Figure 8.9.

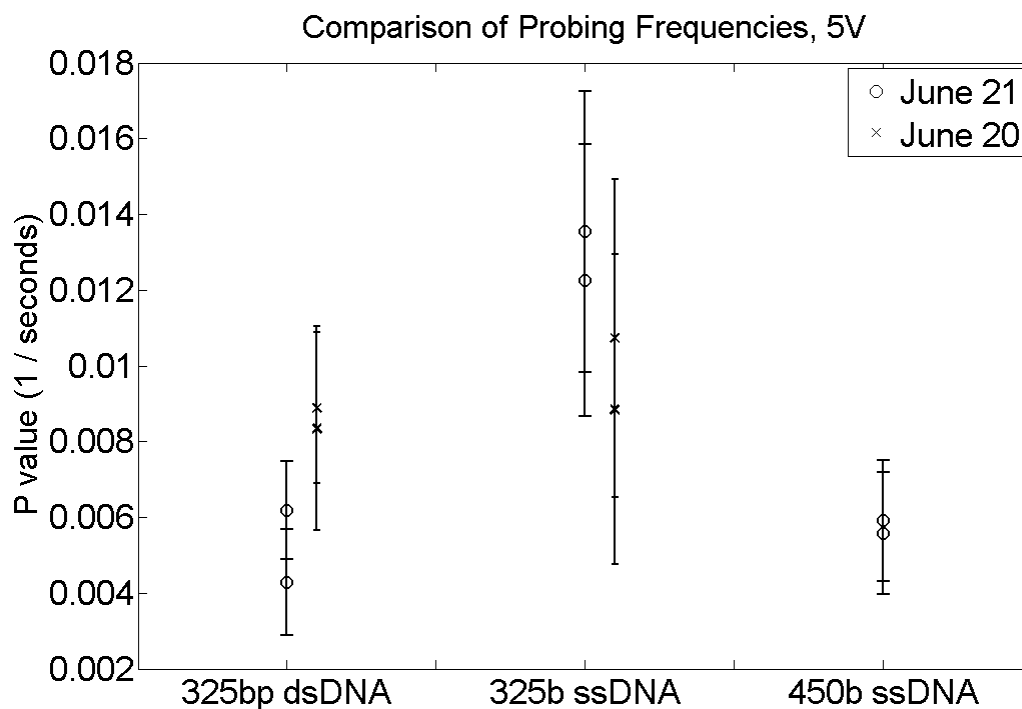


Figure 8.9: Probing frequencies for three different DNA molecules at an entropic barrier under similar driving conditions. Probing frequencies are determined by fitting Equation 8.11 to intensity data such those presented in Figure 8.8. Note that the 325bp dsDNA makes about three times more probing attempts per second that does 325b ssDNA. Note that the larger, 450b ssDNA, make more probing attempts than do the shorter 325b ssDNA, as expected. Error bars are from the fit envelope (MATLAB fit) and are given at 95% confidence.

The data are fit to Equation 8.11, and the resulting P values from the fit are shown in Figure 8.9. While the error bars are large (95% confidence intervals of the fit envelope), one can draw a few qualitative conclusions. The 325b and 325bp P values are different for the June21 data set and have the same qualitative trend for the June20 data set. This reflects what is apparent in Figure 8.8: that the ssDNA molecules trap more strongly than do the dsDNA molecules. Note also that the 450b ssDNA molecules have comparable P values as the 325bp dsDNA, suggesting that the longer ssDNA molecules

have a comparable probing interface with the gap as do the shorter dsDNA molecules. This is consistent with the naïve interpretation of the original entropic trapping model, that the interfacial contact area is the dominant factor in probing the gap.

Now, I'll step back and adopt the not-so-optimistic evaluation of the data. The data are difficult to quantify for a number of reasons. This difficulty is manifest in the large uncertainty bars in Figure 8.9, and suggests that attempting to quantify the intensity at individual entropic barriers is not a good method for analytically determining properties of molecules at the barriers. One must make a subjective determination as to the size of the integration area when quantifying the original videos. One should choose as small a region around the trap as possible so as to quantify only the fluorescence that originates from molecules at the probing interface. But what exactly the probing interface is is somewhat difficult to ascertain as the camera pixels "bleed" when they approach saturation and the individual molecules themselves are difficult to discern (for DNA longer than about 2000bp, it is relatively easy to point to a blob of intensity and say, "That is one DNA molecule."). One does not want the camera pixels to saturate as this automatically ruins the proportionality between the intensity and the number of molecules. Using too low a camera gain, or large a dynamic range, however, often makes it impossible to "see" anything in the channels, which is also a problem.

The above difficulties in quantifying the data and choosing the correct data to quantify can be categorized as "experimenter" problems to be solved by somebody more skilled or more intelligent than me. However, there is one very significant equipment quirk that makes the overall experiment design less

than ideal. The Cascade 512B CCD camera used in these experiments has a “warm up” time that resets every time the camera is put into “acquire” mode. The “acquire” mode is the mode the camera is in when it is actively acquiring images. The camera can be turned on and not be in acquire mode. Examples of the “warming up” are shown in Figure 8.10. These data were collected by observing a clean piece of fused silica directly adjacent to a microfluidic channel through which DNA would be driven in an experiment. The conditions are thus nearly identical to those that would be experienced during a quantitative experiment similar to those described above. When video is recorded immediately after the camera is put into acquire mode, a dramatic increase in intensity over time is observed. Again, the video is of blank glass and there is no reason external to the camera that should cause an increase in the observed intensity over time. Even if the camera has been in the acquire mode for a few minutes, the intensity gain over time is still significant, as shown in the middle curve of Figure 8.10. Experiments are often conducted using a shutter, so in the lower curve of Figure 8.10 a shutter is used to determine if periodically blocking all of the light to the camera has any influence on the intensity increase over time. The lower curve in Figure 8.10 shows that after 5 minutes in the acquire mode, the intensity gain over time is still measurable and that the increase is not dependent upon past measurements (that is, it is not affected by using the shutter). While it is possible to account for the increase in intensity over time by normalizing the measured intensity with the background intensity, it would be advantageous to be able to quantify intensity values with reference to an absolute standard (such as by measuring photons directly) as opposed to a relative scale that must be normalized to the background. An example of “corrected” data is

shown in Figure 8.11 for an AlexaFluor 488-dUTP conjugate molecule driven across an entropic barrier.

Finally, I should point out that the use of the shutter is necessary in order to control photobleaching of the fluorescently labeled DNA molecules. Photobleaching represents another significant non-ideal aspect of trying to quantify intensity information from fluorescently labeled DNA molecules. Photobleaching is evident in the top panel of Figure 8.8 at the end of the experiment. The exponential decay in intensity shows the photobleaching of the AlexaFluor 488 molecules bound to the DNA molecules that were present at the trap when the shutter was left open at the end of the experiment. The bleaching is very rapid and very strong. Each time the shutter is opened to measure the intensity of DNA at the traps, some of the molecules bleach and do not appear in subsequent measurements. Thus, the act of making the measurement affects future measurements. In some cases, the bleached molecules will escape from the trap and the bleaching will have no effect on future measurements. This cannot be guaranteed and generally future measurements are degraded by the measurements that came before. This photobleaching is probably the reason why some of the data points in Figures 8.5 and 8.8 show large fluctuations.

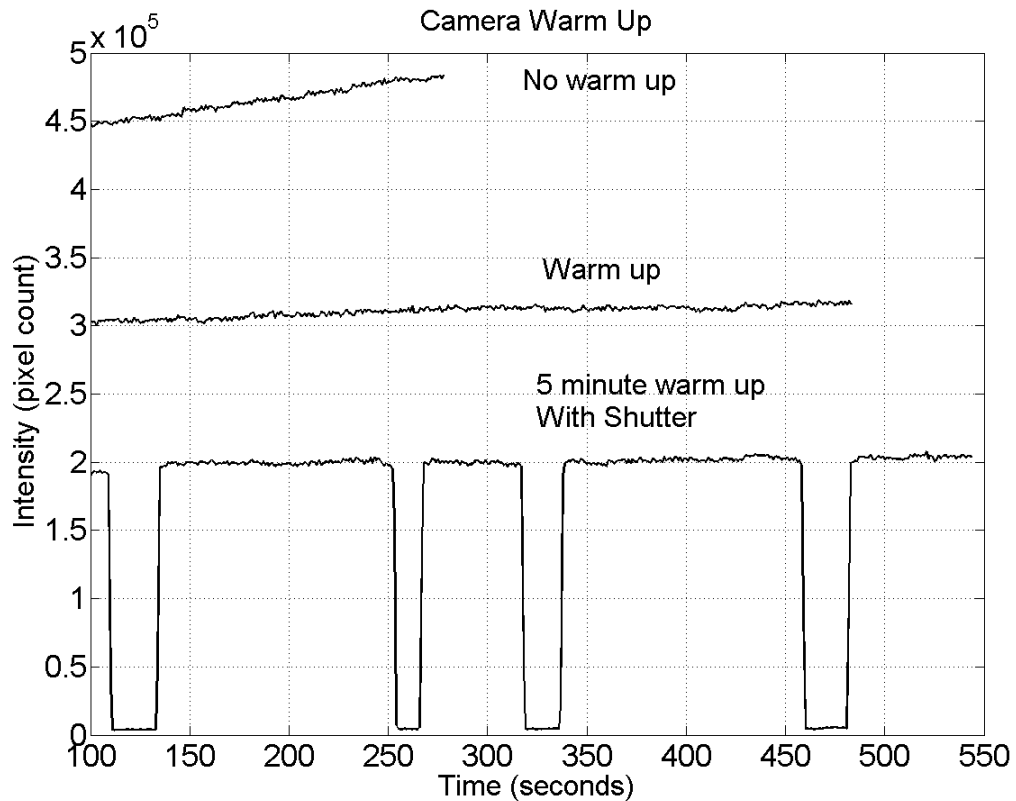


Figure 8.10: Three intensity versus time data showing the “warming up” period of the Cascade 512b CCD camera. Intensities are artificially offset from each other for clarity, and the actual magnitudes of the intensities are all about equal ($\sim 2 \times 10^5$). In each case, data are collected with the camera shutter wide open, a 100x, oil immersion objective, and the image is a clean piece of fused silica glass (a portion of the wafer that contains no fluidic devices and is relatively clean of debris). The upper curve shows the image intensity when the camera is immediately turned on and data acquired. The middle curve is taken after the camera is previously left in the “acquire” mode for about four minutes. And the lowest curve is taken using periodic shuttering after the camera has been left in the “acquire” mode for five minutes.

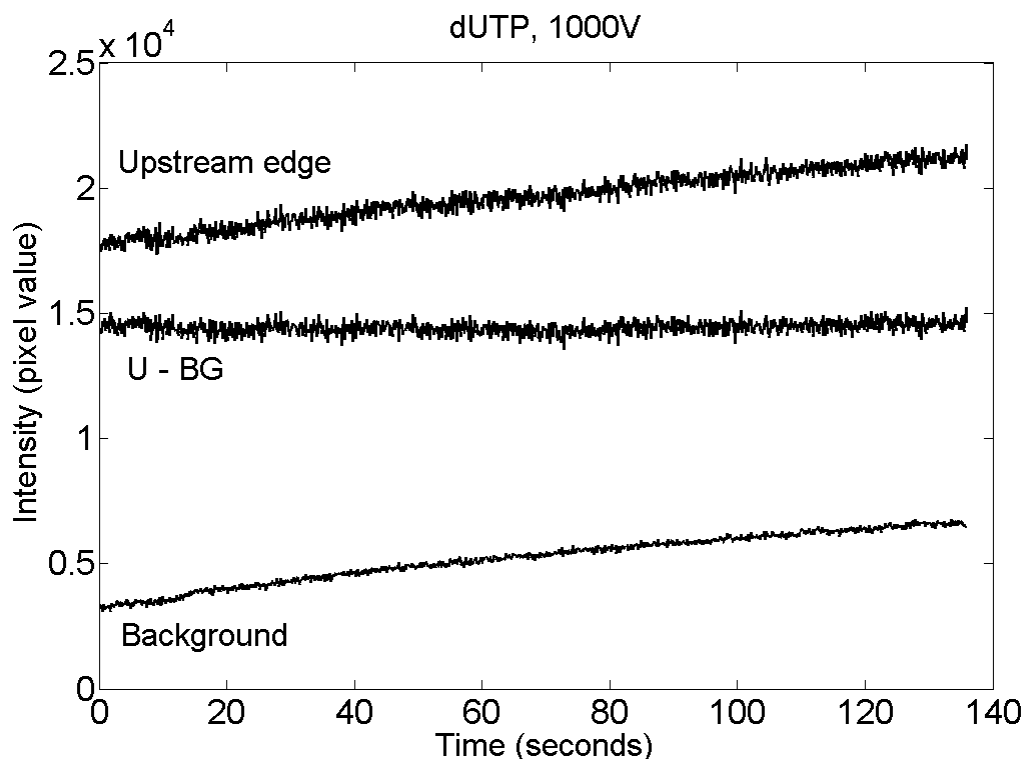


Figure 8.11: Three sets of data showing the increase in intensity caused by the camera “warming up” over time. Data are collected by observing AlexaFluor 488 conjugated to dUTP molecules driven across an entropic barrier at 1000V (so no photobleaching should occur). The lowest curve is taken from an integration area just outside of the area of the microfluidic channel (essentially clean glass and similar to the data shown in Figure 8.10). The uppermost curve is data taken from an integration area at the upstream edge of the entropic barrier. The middle curve is the difference between the upper curve and the lower curve. I refer to this as the background corrected curve because intensity fluctuations caused by the light source or the camera are effectively removed from the upstream data by subtracting from it the background (blank glass) data. Note that the background data increases over time (as in Figure 8.10) and that the middle curve is nearly constant in time. The constancy of the middle curve is expected for properly corrected data for which no analyte concentration at the barrier occurs.

8.4 Conclusions

Single entropic barriers have been used to gather single- and double-stranded DNA molecules by length. Single-stranded DNA has never been

trapped at such a barrier, so this is a significant step towards using entropic barriers or entropic trap arrays to manipulate or separate ssDNA by length. I have attempted to quantify the intensity data in such a way as to determine the probing frequency of molecules at barriers. The probing frequency is a proxy measurement for physical properties of the molecules such as their size or stiffness. Han's original entropic trapping theory was used to fit the quantified intensity data and one of the fit parameters is the probing frequency.

Unfortunately, experimental variability was such that only a qualitative assessment of probing frequencies for different DNA molecules was possible.

Because of the success in showing that ssDNA could be trapped, new entropic trap arrays have been fabricated and experiments are currently underway to separate DNA molecules by length and sequence. The method of data collection and the type of data obtained in these new experiments will not suffer from the same faults as described above for the single barrier experiments. I have also shown that proteins (myosin heavy chain protein and tetanus toxin subunit B, for example) can be trapped at barriers 15nm in thickness (data not shown). Experiments are being conducted to ascertain whether or not entropic trap arrays can be used to separate proteins by length. The results presented, while not entirely what I had hoped for, have shown that entropic traps of about 25nm in thickness can be used to trap these very small, flexible biomolecules. This new result opens the door for further experiments to separate biomolecules that have not previously been separated using entropic traps. As entropic traps have been shown to be useful for separating long DNA molecules, and they are relatively easy to manufacture, the ability to separate ssDNA and proteins would greatly enhance the utility of such structures in lab-on-a-chip devices.

CHAPTER 9

CONCLUDING REMARKS

With this dissertation, I have presented an overview of micro- and nanofluidic technologies available and currently under development for separating biological molecules based upon physical properties such as length. The ability to separate biomolecules is of practical importance because of the myriad medical diagnostics separation techniques permit. Additionally, the ability to manipulate biomolecules within structures of comparable size as the molecules provides on the opportunity to learn about fundamental interactions and processes, not possible with conventional molecular biology techniques. Whether from a practical perspective or from the standpoint of developing next-generation medical and analytical tools, nanofluidics is a powerful tool.

An overview of the field of micro- and nanofluidics was presented, and for those readers who initially skipped that chapter, I would encourage you to return to it now and skim it for historical experiments of particular interest to you. Detailed descriptions of electrophoresis, DNA, and polymer theory were presented to orient the reader and to quickly guide future students of nanofluidics in the right direction for intellectual resources. Finally, a trio of experiments was presented in which high surface area structures and restrictions were used to separate DNA molecules by length. These devices are easily manufactured using standard nanofabrication techniques and can easily be used in conjunction with other fabrication methods or devices not explicitly described herein. The ultimate goal of many in the field of nanofluidics is to create a lab-on-a-chip device capable of high quality samples

analysis with minimal human intervention starting with a biological sample that looks something like a cell. To this end, individual tools (such as those described in chapters 6-8) will be required and will need to be superposed in a relatively complicated device. It is my hope that such a lab-on-a-chip device will incorporate “sub-devices” similar to those that I have spent my graduate school career working on.

I have tried to highlight throughout this dissertation those experiments that I feel could be profitably done by future researchers. To summarize: the gold island fabrication method could be returned to for the manufacture of either pillar-like structures for separating DNA by length, or for creating very high surface area devices for applications like microarrays; fabrication modifications of the nanoslit device should be used to evaluate at what channel depth surface interactions become significant, especially in light of the increased interest in making nanoscale devices for electrophoresis; ideas for tailoring the surface friction in the nanoslit device were presented and these might be profitably employed to increase the efficiency of the device, especially for separating shorter molecules; a hypothetical experiment was performed using the nanoslit device that suggested that one might be able to separate chromosomes using currently existing devices, and these experiments should be performed as they would highlight a very useful application for the nanoslit device; and as mentioned, the entropic trap array devices with barrier thicknesses of less than about 20nm can probably be used to separate proteins by length and to separate single from double stranded DNA. While the technical challenges of performing many of these experiments are very real, the foundation has at least been laid both within the scope of this dissertation and in other work cited herein.

REFERENCES

- [1] J. O. Tegenfeldt *et al.*, *Analytical and Bioanalytical Chemistry* **378**, 1678 (2004).
- [2] P. S. Dittrich, and A. Manz, *Analytical and Bioanalytical Chemistry* **382**, 1771 (2005).
- [3] A. Manz, N. Graber, and H. M. Widmer, *Sensors and Actuators B-Chemical* **1**, 244 (1990).
- [4] http://www.ornl.gov/sci/techresources/Human_Genome/home.shtml.
- [5] D. L. Nelson, and M. M. Cox, *Leninger Principles of Biochemistry*, Worth, New York, 2000, pp. 325.
- [6] D. L. Nelson, and M. M. Cox, *Leninger Principles of Biochemistry*, Worth, New York, 2000, pp. 115.
- [7] C. F. Chou *et al.*, *Electrophoresis* **21**, 81 (2000).
- [8] N. Kaji *et al.*, *Anal Chem* **76**, 15 (2004).
- [9] D. L. Nelson, and M. M. Cox, *Leninger Principles of Biochemistry*, Worth, New York, 2000, pp. 3.
- [10] D. L. Nelson, and M. M. Cox, *Leninger Principles of Biochemistry*, Worth, New York, 2000, pp. 1020.
- [11] D. L. Nelson, and M. M. Cox, *Leninger Principles of Biochemistry*, Worth, New York, 2000, p. 196.
- [12] D. L. Nelson, and M. M. Cox, *Leninger Principles of Biochemistry*, Worth, New York, 2000, pp. 1132.
- [13] J. D. Watson, and F. H. C. Crick, *Nature* **171**, 737 (1953).

- [14] M. Doi, *Introduction to Polymer Physics*, Oxford University Press, Oxford, 2001.
- [15] C. R. Calladine, and H. R. Drew, *Understanding DNA: The Molecule and How it Works*, Academic Press, Inc., San Diego, 1997, pp. 1.
- [16] C. G. Baumann *et al.*, Proc Natl Acad Sci U S A **94**, 6185 (1997).
- [17] N. C. Stellwagen, C. Gelfi, and P. G. Righetti, Biopolymers **42**, 687 (1997).
- [18] C. Heller *et al.*, Journal of Chromatography A **806**, 113 (1998).
- [19] J. Noolandi, Electrophoresis **13**, 394 (1992).
- [20] G. W. Slater *et al.*, Electrophoresis **21**, 3873 (2000).
- [21] J. R. Webster *et al.*, Analytical Chemistry **73**, 1622 (2001).
- [22] R. Riehn, and R. H. Austin, Analytical Chemistry **78**, 5933 (2006).
- [23] S. Pennathur, and J. G. Santiago, Anal Chem **77**, 6782 (2005).
- [24] S. Pennathur, and J. G. Santiago, Anal Chem **77**, 6772 (2005).
- [25] J. Han, and H. G. Craighead, Journal of Vacuum Science & Technology a-Vacuum Surfaces and Films **17**, 2142 (1999).
- [26] H. A. Stone, A. D. Stroock, and A. Ajdari, Annual Review of Fluid Mechanics **36**, 381 (2004).
- [27] R. F. Probstein, *Physicochemical Hydrodynamics: An Introduction*, Academic Press, Inc., San Diego, pp. 185, 1989.
- [28] M. Cabodi *et al.*, Electrophoresis **23**, 3496 (2002).
- [29] D. J. Harrison *et al.*, Analytical Chemistry **64**, 1926 (1992).
- [30] S. C. Jacobson *et al.*, Analytical Chemistry **66**, 1107 (1994).
- [31] D. J. Harrison *et al.*, Science **261**, 895 (1993).
- [32] Y. F. Cheng, and N. J. Dovichi, Science **242**, 562 (1988).
- [33] S. C. Jacobson, A. W. Moore, and J. M. Ramsey, Analytical Chemistry **67**, 2059 (1995).

- [34] D. F. Swaile, and M. J. Sepaniak, *Analytical Chemistry* **63**, 179 (1991).
- [35] M. N. Albargheuthi, and A. E. Barron, *Electrophoresis* **21**, 4096 (2000).
- [36] C. S. Effenhauser *et al.*, *Analytical Chemistry* **66**, 2949 (1994).
- [37] A. T. Woolley, and R. A. Mathies, *Proc Natl Acad Sci U S A* **91**, 11348 (1994).
- [38] A. T. Woolley, and R. A. Mathies, *Analytical Chemistry* **67**, 3676 (1995).
- [39] Caliper Lifesciences, *The Application Notebook*, p. 22.
- [40] Agilent Technologies, *Agilent Bioanalyzer 2100 Guide*.
- [41] W. D. Volkmuth, and R. H. Austin, *Nature* **358**, 600 (1992).
- [42] T. A. Duke *et al.*, *Electrophoresis* **17**, 1075 (1996).
- [43] S. W. Turner *et al.*, *Journal of Vacuum Science & Technology B* **16**, 3835 (1998).
- [44] M. Cabodi, S. W. Turner, and H. G. Craighead, *Anal Chem* **74**, 5169 (2002).
- [45] J. T. Mannion *et al.*, *Biophys J* **90**, 4538 (2006).
- [46] C. H. Reccius *et al.*, *Phys Rev Lett* **95**, 268101 (2005).
- [47] A. Baumgartner, and M. Muthukumar, *Journal of Chemical Physics* **87**, 3082 (1987).
- [48] M. Muthukumar, and A. Baumgartner, *Macromolecules* **22**, 1937 (1989).
- [49] M. Muthukumar, and A. Baumgartner, *Macromolecules* **22**, 1941 (1989).
- [50] G. I. Nixon, and G. W. Slater, *Physical Review E* **53**, 4969 (1996).
- [51] G. W. Slater, and S. Y. Wu, *Physical Review Letters* **75**, 164 (1995).
- [52] L. Liu, P. S. Li, and A. S. Asher, *Journal of the American Chemical Society* **121**, 4040 (1999).
- [53] L. Liu, P. S. Li, and S. A. Asher, *Nature* **397**, 141 (1999).
- [54] J. Rousseau, G. Drouin, and G. W. Slater, *Physical Review Letters* **79**, 1945 (1997).

- [55] D. L. Smisek, and D. A. Hoagland, *Science* **248**, 1221 (1990).
- [56] J. Han, and H. G. Craighead, *Science* **288**, 1026 (2000).
- [57] J. Y. Han, and H. G. Craighead, *Analytical Chemistry* **74**, 394 (2002).
- [58] J. Han, S. W. Turner, and H. G. Craighead, *Physical Review Letters* **83**, 1688 (1999).
- [59] F. Tessier, J. Labrie, and G. W. Slater, *Macromolecules* **35**, 4791 (2002).
- [60] Z. Chen, and F. A. Escobedo, *Molecular Simulation* **29**, 417 (2003).
- [61] M. Streek *et al.*, *Journal of Biotechnology* **112**, 79 (2004).
- [62] J. P. Fu, J. Yoo, and J. Y. Han, *Physical Review Letters* **97** (2006).
- [63] J. P. Fu, P. Mao, and J. Y. Han, *Applied Physics Letters* **87** (2005).
- [64] R. P. Feynman, R. B. Leighton, and M. Sands, in *The Feynman Lectures on Physics* (Addison-Wesley, Reading, 1963), pp. 46.
- [65] J. Rousselet *et al.*, *Nature* **370**, 446 (1994).
- [66] D. R. Chialvo, and M. M. Millonas, *Physics Letters A* **209**, 26 (1995).
- [67] G. W. Slater, H. L. Guo, and G. I. Nixon, *Physical Review Letters* **78**, 1170 (1997).
- [68] T. A. J. Duke, and R. H. Austin, *Physical Review Letters* **80**, 1552 (1998).
- [69] D. Ertas, *Physical Review Letters* **80**, 1548 (1998).
- [70] S. Leibler, *Nature* **370**, 412 (1994).
- [71] C. F. Chou *et al.*, *Proceedings of the National Academy of Sciences of the United States of America* **96**, 13762 (1999).
- [72] D. E. Smith, H. P. Babcock, and S. Chu, *Science* **283**, 1724 (1999).
- [73] A. van Oudenaarden, and S. G. Boxer, *Science* **285**, 1046 (1999).
- [74] B. J. Kane *et al.*, *Analytical Chemistry* **78**, 4291 (2006).
- [75] J. H. Wittig, A. F. Ryan, and P. M. Asbeck, *Journal of Neuroscience Methods* **144**, 79 (2005).

- [76] J. El-Ali, P. K. Sorger, and K. F. Jensen, *Nature* **442**, 403 (2006).
- [77] J. R. Burns, and C. Ramshaw, *Lab on a Chip* **1**, 10 (2001).
- [78] S. L. Anna, N. Bontoux, and H. A. Stone, *Applied Physics Letters* **82**, 364 (2003).
- [79] I. Shestopalov, J. D. Tice, and R. F. Ismagilov, *Lab on a Chip* **4**, 316 (2004).
- [80] E. M. Chan, A. P. Alivisatos, and R. A. Mathies, *Journal of the American Chemical Society* **127**, 13854 (2005).
- [81] A. J. deMello, *Nature* **442**, 394 (2006).
- [82] G. J. M. Bruin, *Electrophoresis* **21**, 3931 (2000).
- [83] V. Dolnik, S. R. Liu, and S. Jovanovich, *Electrophoresis* **21**, 41 (2000).
- [84] C. T. Culbertson *et al.*, *Analytical Chemistry* **77**, 7933 (2005).
- [85] J. C. Roulet *et al.*, *Optical Engineering* **40**, 814 (2001).
- [86] J. C. Roulet *et al.*, *Analytical Chemistry* **74**, 3400 (2002).
- [87] J. Hubner *et al.*, *Review of Scientific Instruments* **72**, 229 (2001).
- [88] J. Seo, and L. P. Lee, *Sensors and Actuators B-Chemical* **99**, 615 (2004).
- [89] D. L. Nelson, and M. M. Cox, *Leninger Principles of Biochemistry*, Worth, New York, 2000.
- [90] M. Doi, *Introduction to Polymer Physics*, Oxford University Press, Oxford, 2001.
- [91] P. J. Flory, *Statistical Mechanics of Chain Molecules*. Oxford University Press, New York, 1989.
- [92] J. L. Viovy, *Reviews of Modern Physics* **72**, 813 (2000).
- [93] S. W. Turner, PhD Thesis, Cornell University, Ithaca, 2000.
- [94] L. Onsager, *Annals of the New York Academy of Sciences* **51**, 627 (1949).
- [95] D. W. Schaefer, J. F. Joanny, and P. Pincus, *Macromolecules* **13**, 1280 (1980).
- [96] R. T. Hunter, *Zeta Potential in Colloid Science* (1984).

- [97] J. Lyklema, *Fundamentals of Interface and Colloid Science*, Academic Press Inc., San Diego, 1991.
- [98] R. F. Probstein, *Physicochemical Hydrodynamics: An Introduction*. Butterworth Publishers, Boston, 1989.
- [99] N. Kaji *et al.*, *Analytical Chemistry* **76**, 15 (2004).
- [100] A. J. Storm *et al.*, *Phys Rev E Stat Nonlin Soft Matter Phys* **71**, 051903 (2005).
- [101] A. J. Storm *et al.*, *Nano Lett* **5**, 1193 (2005).
- [102] O. B. Bakajin *et al.*, *Physical Review Letters* **80**, 2737 LP (1998).
- [103] W. Reisner *et al.*, *Phys Rev Lett* **94**, 196101 (2005).
- [104] J. O. Tegenfeldt *et al.*, *Proc Natl Acad Sci U S A* **101**, 10979 (2004).
- [105] J. Han, and H. G. Craighead, *Science* **288**, 1026 (2000).
- [106] F. Brochard, *Journal De Physique* **38**, 1285 (1977).
- [107] H. Ren *et al.*, *Electrophoresis* **20**, 2501 (1999).
- [108] V. Barger, and M. Olsson, *Classical Mechanics: A Modern Perspective*. McGraw-Hill, Inc., New York, 1995.
- [109] S. J. Hubert, and G. W. Slater, *Electrophoresis* **16**, 2137 (1995).
- [110] J. Noolandi, *Electrophoresis* **14**, 680 (1993).
- [111] R. J. Meagher *et al.*, *Electrophoresis* **27**, 1702 (2006).
- [112] R. J. Meagher *et al.*, *Electrophoresis* **26**, 331 (2005).
- [113] K. A. Ferguson, *Metabolism-Clinical and Experimental* **13**, 985 (1964).
- [114] Chrambac.A, and D. Rodbard, *Science* **172**, 440 (1971).
- [115] J. C. Giddings *et al.*, *Journal of Physical Chemistry* **72**, 4397 (1968).
- [116] J. Lunney, Chrambac.A, and D. Rodbard, *Analytical Biochemistry* **40**, 158 (1971).
- [117] A. G. Ogston, *Transactions of the Faraday Society* **54**, 1754 (1958).

- [118] D. Rodbard, and Chrambac.A, Proceedings of the National Academy of Sciences of the United States of America **65**, 970 (1970).
- [119] D. Rodbard, and Chrambac.A, Analytical Biochemistry **40**, 95 (1971).
- [120] D. L. Holmes, and N. C. Stellwagen, Electrophoresis **12**, 612 (1991).
- [121] N. C. Stellwagen, Electrophoresis **19**, 1542 (1998).
- [122] B. Q. Li *et al.*, Analytical Chemistry **78**, 4743 (2006).
- [123] B. Q. Li *et al.*, Electrophoresis **27**, 1312 (2006).
- [124] S. W. Turner, M. Cabodi, and H. G. Craighead, Phys Rev Lett **88**, 128103 (2002).
- [125] Q. Gao, H. M. Pang, and E. S. Yeung, Electrophoresis **20**, 1518 (1999).
- [126] Q. Gao, and E. S. Yeung, Anal Chem **70**, 1382 (1998).
- [127] P. D. Grossman, and J. C. Colburn, *Capillary Electrophoresis: Theory and Practice* San Diego, 1992, pp. 111.
- [128] A. E. Nkodo *et al.*, Electrophoresis **22**, 2424 (2001).
- [129] J. Han, PhD Thesis, Cornell University, Ithaca.
- [130] J. D. Cross, K. T. Samiee, and H. Craighead, in *Micro-Total Analytical Systems* Boston, MA, 2005.